STATE OF THE CLIMATE IN 2022

THE TROPICS

H. J. Diamond and C. J. Schreck, Eds.

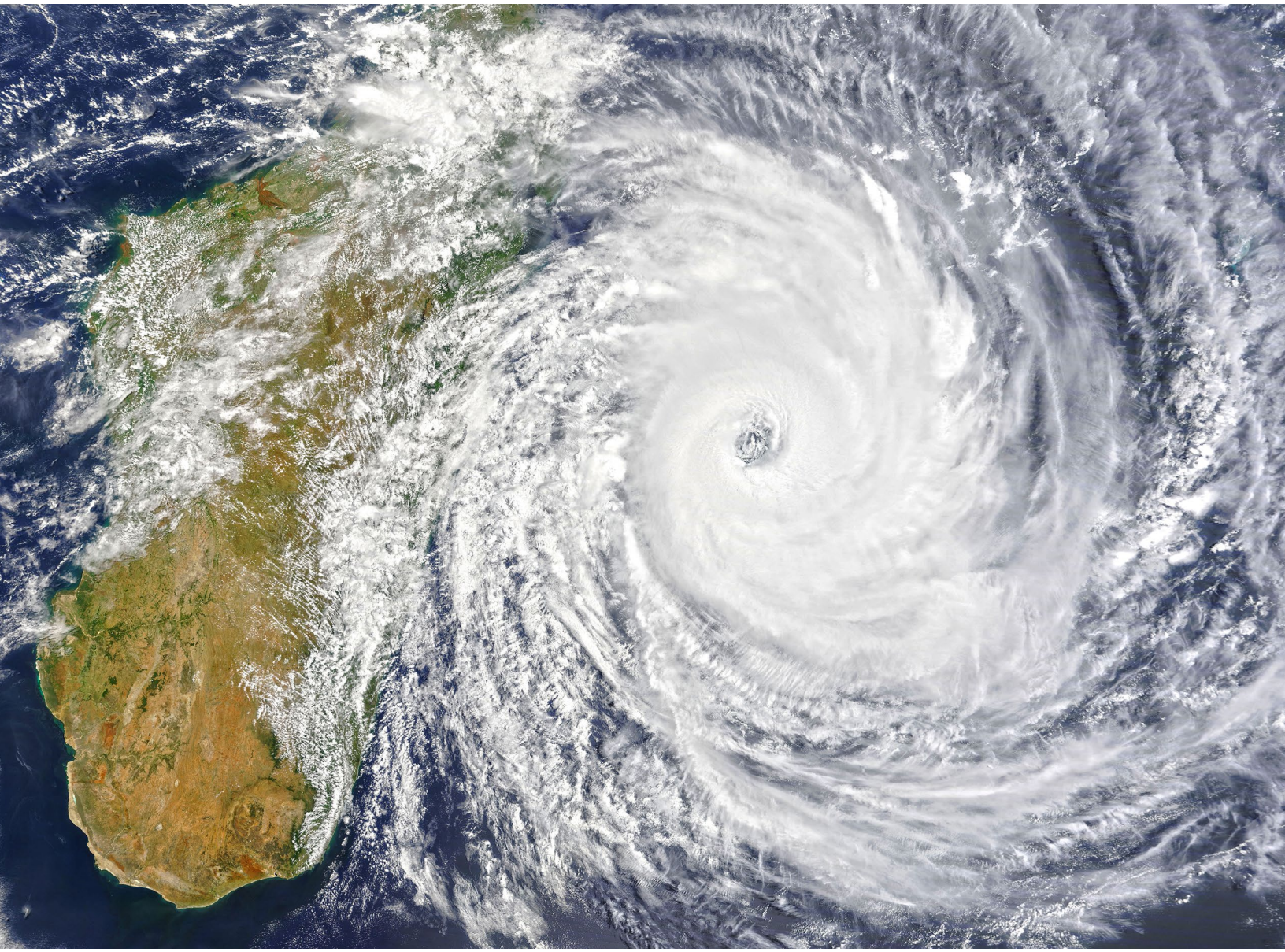

Special Online Supplement to the *Bulletin of the American Meteorological Society* Vol. 104, No. 8, August, 2023

https://doi.org/10.1175/BAMS-D-23-0078.1

Corresponding author: Howard J. Diamond / howard.diamond@noaa.gov

STATE OF THE CLIMATE IN 2022
The Tropics

Editors

Ellen Bartow-Gillies
Jessica Blunden
Tim Boyer

Chapter Editors

Peter Bissolli
Kyle R. Clem
Howard J. Diamond
Matthew L. Druckenmiller
Robert J. H. Dunn
Catherine Ganter
Nadine Gobron
Gregory C. Johnson
Rick Lumpkin
Ademe Mekonnen
John B. Miller
Twila A. Moon
Marilyn N. Raphael
Ahira Sánchez-Lugo
Carl J. Schreck III
Richard L. Thoman
Kate M. Willett
Zhiwei Zhu

Technical Editor

Lukas Noguchi

BAMS Special Editor for Climate

Michael A. Alexander

American Meteorological Society

Cover Credit:
Hurricane Ian as seen from NOAA's GOES-East satellite on 27 September 2022 at 0826 UTC in the Gulf of Mexico.

(Image credit: NOAA/NESDIS)

How to cite this document:
The Tropics is one chapter from the *State of the Climate in 2022* annual report and is available from https://doi.org/10.1175/BAMS-D-23-0078.1. Compiled by NOAA's National Centers for Environmental Information, *State of the Climate in 2022* is based on contributions from scientists from around the world. It provides a detailed update on global climate indicators, notable weather events, and other data collected by environmental monitoring stations and instruments located on land, water, ice, and in space. The full report is available from https://doi.org/10.1175/2023BAMSStateoftheClimate.1.

Citing the complete report:
Blunden, J., T. Boyer, and E. Bartow-Gillies, Eds., 2023: "State of the Climate in 2022". Bull. Amer. Meteor. Soc., 104 (8), Si–S501 https://doi.org/10.1175/2023BAMSStateoftheClimate.1.

Citing this chapter:
Diamond, H.J. and C. J. Schreck, Eds., 2023: The Tropics [in "State of the Climate in 2022"]. Bull. Amer. Meteor. Soc., 104 (8), S207–S270, https://doi.org/10.1175/BAMS-D-23-0078.1.

Citing a section (example):
Allgood, A. and C. J. Schreck, 2023: Tropical intraseasonal activity [in "State of the Climate in 2022"]. Bull. Amer. Meteor. Soc., 104 (8), S218–S220, https://doi.org/10.1175/BAMS-D-23-0078.1.

Editor and Author Affiliations (alphabetical by name)

Allgood, Adam, NOAA/NWS National Centers for Environmental Prediction Climate Prediction Center, College Park, Maryland

Becker, Emily J., University of Miami Rosenstiel School of Marine and Atmospheric Science, Miami, Florida

Blake, Eric S., NOAA/NWS National Hurricane Center, Miami, Florida

Bringas, Francis G., NOAA/OAR Atlantic Oceanographic and Meteorological Laboratory, Miami, Florida

Camargo, Suzana J., Lamont-Doherty Earth Observatory, Columbia University, Palisades, New York

Chen, Lin, Institute for Climate and Application Research (ICAR)/KLME/ILCEC/CIC-FEMD, Nanjing University of Information Science and Technology, Nanjing, China

Coelho, Caio A.S., Centro de Previsão do Tempo e Estudos Climáticos/National Institute for Space Research, Center for Weather Forecasts and Climate Studies, Cachoeira Paulista, Brazil

Diamond, Howard J., NOAA/OAR Air Resources Laboratory, College Park, Maryland

Fauchereau, Nicolas, National Institute of Water and Atmospheric Research, Ltd., Auckland, New Zealand

Fogarty, Chris, Canadian Hurricane Centre, Dartmouth, Canada

Goldenberg, Stanley B., NOAA/OAR Atlantic Oceanographic and Meteorological Laboratory, Miami, Florida

Goni, Gustavo, NOAA/OAR Atlantic Oceanographic and Meteorological Laboratory, Miami, Florida

Harnos, Daniel S., NOAA/NWS National Centers for Environmental Prediction Climate Prediction Center, College Park, Maryland

He, Qiong, Earth System Modeling Center, Nanjing University of Information Science and Technology, Nanjing, China

Hu, Zeng-Zhen, NOAA/NWS Climate Prediction Center, College Park, Maryland

Klotzbach, Philip J., Department of Atmospheric Science, Colorado State University, Fort Collins, Colorado

Knaff, John A., NOAA/NESDIS Center for Satellite Applications and Research, Fort Collins, Colorado

Kumar, Arun, NOAA/NWS National Centers for Environmental Prediction Climate Prediction Center, College Park, Maryland

L'Heureux, Michelle, NOAA/NWS National Centers for Environmental Prediction Climate Prediction Center, College Park, Maryland

Landsea, Chris W., NOAA/NWS National Hurricane Center, Miami, Florida

Lin, I-I., National Taiwan University, Taipei, Taiwan

Lorrey, Andrew M., National Institute of Water and Atmospheric Research, Ltd., Auckland, New Zealand

Luo, Jing-Jia, Institute for Climate and Application Research, Nanjing University of Information Science and Technology, Nanjing, China

Magee, Andrew D., Centre for Water, Climate and Land, School of Environmental and Life Sciences, University of Newcastle, Callaghan, Australia

Pasch, Richard J., NOAA/NWS National Hurricane Center, Miami, Florida

Pezza, Alexandre B., Greater Wellington Regional Council, Wellington, New Zealand

Rosencrans, Matthew, NOAA/NWS National Centers for Environmental Prediction Climate Prediction Center, College Park, Maryland

Rozkošný, Jozef, Slovak Hydrometeorological Institute, Bratislava, Slovakia

Schreck, Carl J., North Carolina State University, North Carolina Institute for Climate Studies, Cooperative Institute Satellite Earth System Studies, Asheville, North Carolina

Trewin, Blair C., Australian Bureau of Meteorology, Melbourne, Australia

Truchelut, Ryan E., WeatherTiger, Tallahassee, Florida

Wang, Bin, School of Ocean and Earth Science and Technology, Department of Meteorology, University of Hawaii; International Pacific Research Center, Honolulu, Hawaii

Wang, Hui, NOAA/NWS National Centers for Environmental Prediction Climate Prediction Center, College Park, Maryland

Wood, Kimberly M., Department of Geosciences, Mississippi State University, Mississippi State, Mississippi

Editorial and Production Team

Allen, Jessicca, Graphics Support, Cooperative Institute for Satellite Earth System Studies, North Carolina State University, Asheville, North Carolina

Camper, Amy V., Graphics Support, Innovative Consulting and Management Services, LLC, NOAA/NESDIS National Centers for Environmental Information, Asheville, North Carolina

Haley, Bridgette O., Graphics Support, NOAA/NESDIS National Centers for Environmental Information, Asheville, North Carolina

Hammer, Gregory, Content Team Lead, Communications and Outreach, NOAA/NESDIS National Centers for Environmental Information, Asheville, North Carolina

Love-Brotak, S. Elizabeth, Lead Graphics Production, NOAA/NESDIS National Centers for Environmental Information, Asheville, North Carolina

Ohlmann, Laura, Technical Editor, Innovative Consulting and Management Services, LLC, NOAA/NESDIS National Centers for Environmental Information, Asheville, North Carolina

Noguchi, Lukas, Technical Editor, Innovative Consulting and Management Services, LLC, NOAA/NESDIS National Centers for Environmental Information, Asheville, North Carolina

Riddle, Deborah B., Graphics Support, NOAA/NESDIS National Centers for Environmental Information, Asheville, North Carolina

Veasey, Sara W., Visual Communications Team Lead, Communications and Outreach, NOAA/NESDIS National Centers for Environmental Information, Asheville, North Carolina

4. Table of Contents

Please refer to Chapter 8 (Relevant Datasets and Sources) for a list of all climate variables and datasets used in this chapter for analyses, along with their websites for more information and access to the data.

4. THE TROPICS

H. J. Diamond and C. J. Schreck, Eds.

a. Overview

—H. J. Diamond and C. J. Schreck

In 2022, the El Niño–Southern Oscillation (ENSO) continued a multi-year La Niña event spanning the period from 2020 to 2022. La Niña conditions started in July–September 2020 and have lasted nearly continuously for over two years, with a brief period of ENSO-neutral conditions between May–July and June–August 2021. In 2022, La Niña fluctuated between weak and moderate strength, with an Oceanic Niño Index (ONI) value of –1.1°C in March–May (peak ONI values between –1.0° and –1.4°C are defined to be moderate strength) and weakening to –0.8°C in June–August. Following the Northern Hemisphere summer, La Niña strengthened again with a peak intensity of –1.0°C in August–October and September–November 2022.

For the global tropics, the NOAA Merged Land Ocean Global Surface Temperature analysis (NOAA GlobalTemp; Vose et al. 2021) indicates that the combined average land and ocean surface temperature (measured 20°S–20°N) was 0.01°C above the 1991–2020 average, tying with 2004 and 2006 as the 17th-warmest year for the tropics in the 173-year data record. The five warmest years in the tropics since 1850 have all occurred since 2015. Data from the Global Precipitation Climatology Project indicate a mean annual total precipitation value of 1413 mm across the 20°S–20°N latitude band over land. This is 9 mm above the 1991–2020 average and ranks 20th wettest for the 1979–2022 period of record.

Globally, 85 named tropical cyclones (TCs; ≥34 kt; or ≥17 m s^{-1}) were observed during the 2022 Northern Hemisphere season (January–December 2022) and the 2021/22 Southern Hemisphere season (July–June 2021/22; see Table 4.2), as documented in the International Best Track Archive for Climate Stewardship version 4 (Knapp et al. 2010). Overall, this number was near the 1991–2020 global average of 87 TCs but below the 96 TCs reported during the 2021 season (Diamond and Schreck 2022) and the all-time record 104 named storms in 1992.

Of the 85 named storms, 40 reached tropical-cyclone strength and 16 reached major tropical-cyclone strength. Both of these counts were below their 1991–2020 averages. The accumulated cyclone energy (ACE; an integrated metric of the strength, frequency, and duration of tropical storms and hurricanes) was the lowest on record since reliable data began in 1981. No basin was more active than normal in terms of ACE. The North Atlantic, eastern North Pacific, and South Indian Ocean basins had near-normal activity. The other basins were all less active than normal, including the western North Pacific, which had its third consecutive season with below-normal activity. Three storms reached Category 5 on the Saffir-Simpson Hurricane Wind Scale during 2022. Two were from the western North Pacific: Super Typhoons Hinnamnor and Noru. The third was Hurricane Ian in the North Atlantic, which was upgraded to Category 5 during post-season analysis (Bucci et al. 2023). This was the fewest Category 5 storms globally since 2017.

The 14 named storms in the North Atlantic during 2022 were the fewest observed since 2015 when 11 named storms developed and well below the 21 named storms in 2021. Eight hurricanes developed in 2022, one more than occurred in 2021 and near the 1991–2020 average of seven. Two major hurricanes occurred, which was slightly below the 1991–2020 average of three and half as many as occurred in 2021. The 2022 North Atlantic hurricane season was classified by NOAA's National Hurricane Center as a near-normal season based on ACE, ending the streak

of six consecutive above-normal seasons (2016–21). Even during near-normal seasons, a single hurricane can bring devastation to an area. Hurricane Ian caused over 100 deaths and more than $100 billion (U.S. dollars) in damage, making it the third-costliest hurricane in U.S. history. Hurricane Fiona caused extreme flooding in Puerto Rico before making landfall in Canada as the country's strongest storm on record in terms of pressure. Both storms are featured in Sidebar 4.1 as well as in section 4g2.

While we do not normally report on volcanic eruptions, given the climatic impact that a large volcanic eruption can have, we would be remiss in not mentioning the eruption of the Hunga Tonga-Hunga Ha'apai (HTHH) in the southwest island nation of Tonga on 15 January 2022. HTHH ranked a 5.7 on the Volcanic Explosivity Index, alongside other history makers like Vesuvius in 79 CE and Mount St. Helens in 1980 (Besl 2023). The injection of water into the atmosphere was unprecedented in both magnitude (far exceeding any previous values in the 17-year *Aura* Microwave Limb Sounder record) and altitude (penetrating into the mesosphere). Millán et al (2022) estimates that the mass of water injected into the stratosphere to be 146±5 Tg, or~10% of the stratospheric burden.

It may take several years for the water plume to dissipate, and it is thought that this eruption could impact climate, not through surface cooling due to sulfate aerosols, but rather through possible surface warming due to the radiative forcing from the excess stratospheric water vapor. Similar to the climate effects (albeit cooling) of Mount Pinatubo in the Philippines in 1991, but unlike other eruptions its size, HTHH had a relatively low sulfur dioxide content. While it has been theorized that it may have added only 0.004°C of global cooling in 2022 (Zuo et al. 2022), it may take a few more years to fully determine if this eruption had any possible long-term climate effects.

b. ENSO and the tropical Pacific

—Z.-Z. Hu, M. L'Heureux, A. Kumar, and E. Becker

The El Niño–Southern Oscillation (ENSO) is an ocean and atmosphere-coupled climate phenomenon that occurs across the tropical Pacific Ocean. Its warm and cold phases are called El Niño and La Niña, respectively. For historical purposes, NOAA's Climate Prediction Center classifies and assesses the strength and duration of El Niño and La Niña events using the Oceanic Niño Index (ONI; shown for mid-2020 through 2022 in Fig. 4.1). The ONI is the three-month (seasonal) running average of sea-surface temperature (SST) anomalies in the Niño-3.4 region (5°S–5°N, 170°W–120°W), currently calculated as the departure from the 1991–2020 base period mean[1]. El Niño is classified when the ONI is at or greater than +0.5°C for at least five consecutive, overlapping seasons, while La Niña is classified when the ONI is at or less than –0.5°C for at least five consecutive, overlapping seasons.

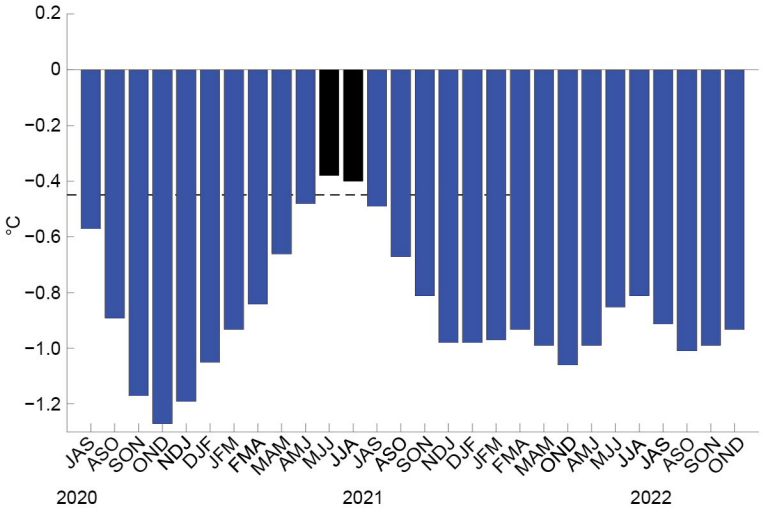

Fig. 4.1. Time series of the Oceanic Niño Index (ONI, °C) from mid-2020 through 2022. Overlapping three-month seasons are labeled on the x-axis, with initials indicating the first letter of each month in the season. Blue bars indicate negative values that are less than –0.5°C. ONI values are derived from the ERSSTv5 dataset and are based on departures from the 1991–2020 period monthly means (Huang et al. 2017).

The time series of the ONI (Fig. 4.1) shows a multi-year La Niña event spanning 2020–22 (Fang et al. 2023). La Niña conditions started in July–September

[1] The ONI is an index measuring ENSO, and to highlight its seasonal-to-interannual component, the base period is updated every five years with a rolling 30-year climatology. SSTs in the Niño-3.4 region have multi-decadal and longer trends going back to 1950 or earlier, and the rolling climatology reduces the influence of trend on the state of ENSO.

2020 and have lasted nearly continuously for over two years, with a brief period of ENSO-neutral conditions between May–July and June–August (JJA) 2021 (Fig. 4.1). In 2022, La Niña fluctuated between moderate and weak strength with an ONI value of –1.1°C in March–May (MAM; peak ONI value between –1.0° and –1.4°C is defined to be moderate strength) and weakening to –0.8°C in June–August. Following the Northern Hemisphere summer, La Niña strengthened again with a peak intensity of –1.0°C in August–October and September–November (SON). Sidebar 3.1 in Chapter 3 describes the triple La Niña event.

(i) Oceanic conditions

Figure 4.2 displays the three-monthly mean SST (left column) and SST anomalies (right column) during December–February (DJF) 2021/22 through September–November (SON) 2022. Consistent with La Niña, below-average SSTs persisted across most of the equatorial Pacific Ocean during the year. During DJF (Fig. 4.2b), the strongest SST anomalies on the equator exceeded –2.0°C in a small portion of the eastern equatorial Pacific (between 120°E and 80°W), implying a strengthening of the cold tongue (Fig. 4.2a). During MAM, the negative SST anomalies strengthened in the central equatorial Pacific and expanded westward (Fig. 4.2d). Below-average SSTs were weakest across the equatorial Pacific in JJA, but remained in excess of –1.0°C in small regions of the central and far eastern Pacific (Fig. 4.2f). The western Pacific warm pool remained contracted to the west during most of the year, with the 30°C isotherm nearly vanishing during JJA (Fig. 4.2e). During SON, below-average SSTs re-strengthened in the central and eastern equatorial Pacific (Fig. 4.2h). A horseshoe-like pattern of above-average SSTs stretched from the western tropical Pacific to the extratropical North and South Pacific Oceans during all seasons.

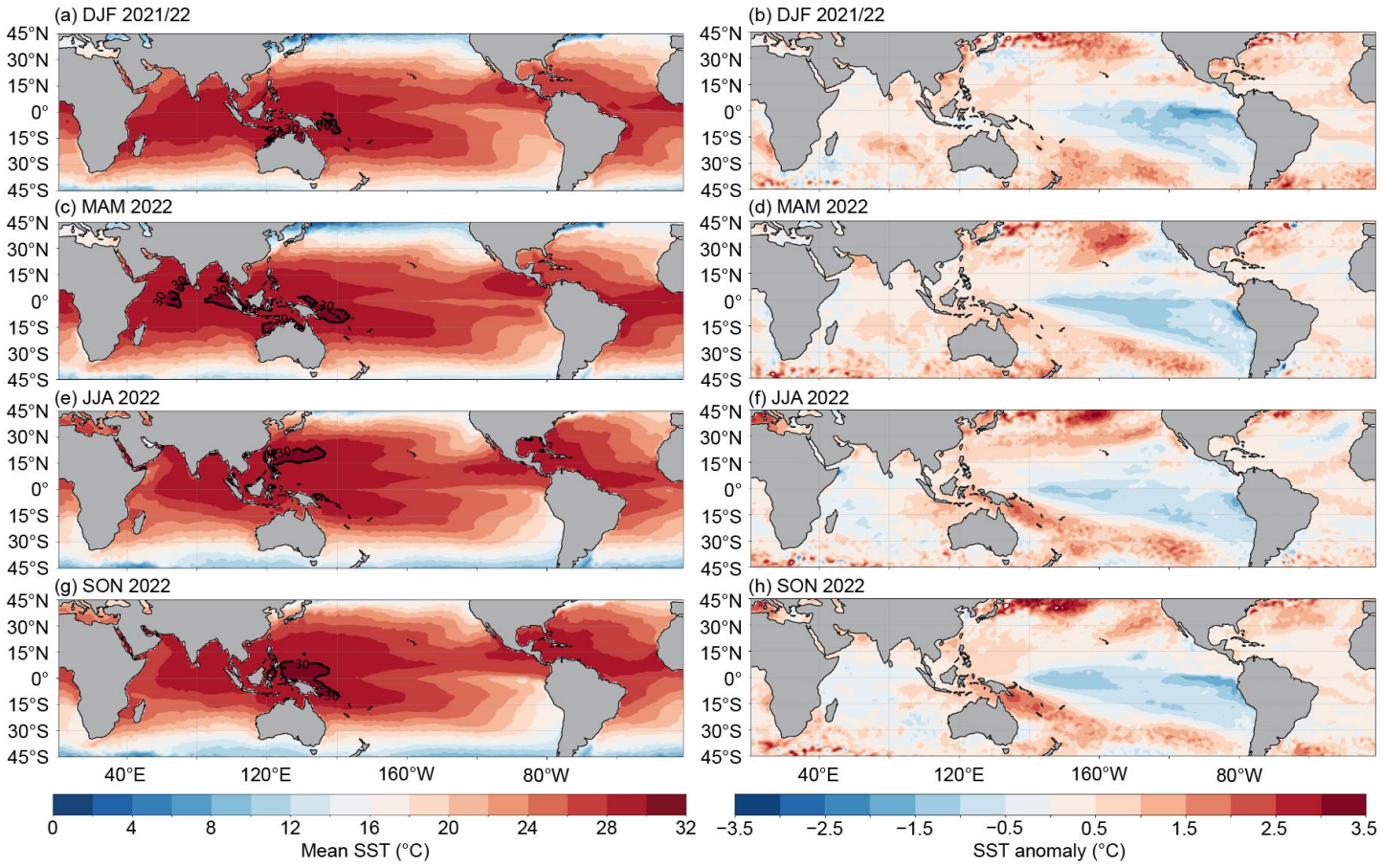

Fig 4.2. Mean sea-surface temperature (SST; left) and SST anomaly (right) for (a),(b) DJF 2021/22, (c),(d) MAM 2022, (e),(f) JJA 2022, and (g),(h) SON 2022. Units are in °C. The bold contour for SST is located at 30°C. Anomalies are departures from the 1991–2020 seasonal adjusted OIv2.1 climatology (Huang et al. 2020).

Consistent with the evolution of SST anomalies and La Niña, the subsurface temperature anomalies were a dipole-like pattern centered along the thermocline in the western and eastern Pacific Ocean (Kumar and Hu 2014). The positive temperature anomalies were centered in the western and central equatorial Pacific, while negative temperature anomalies were strongest in the eastern Pacific throughout the year. These anomalies reflect a steeper-than-average thermocline slope (solid line) with shallow anomalies in the eastern Pacific and deep anomalies in the western Pacific (Fig. 4.3). Negative subsurface temperature anomalies also persisted within the mixed layer near the date line. The slope of the thermocline was steepest in SON, which was also when the anomalous subsurface temperature gradient was strongest (Fig. 4.3d). These subsurface features were relatively weaker in MAM and JJA (Figs. 4.3b,c).

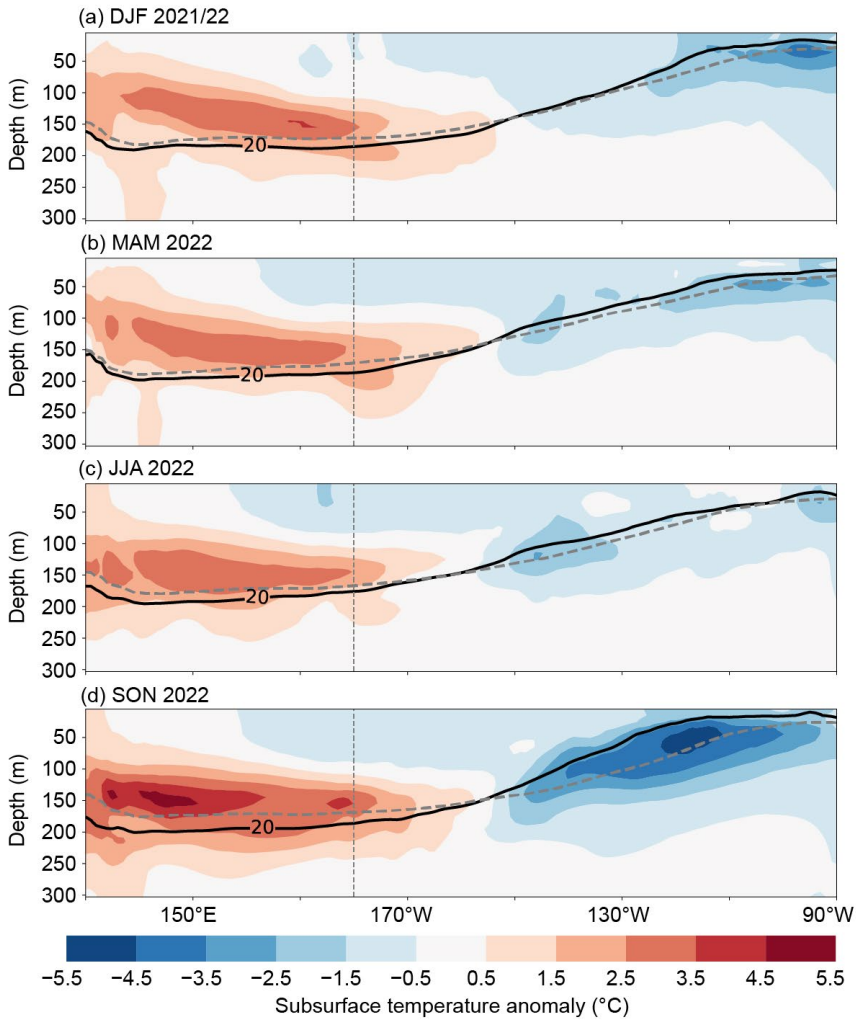

Fig 4.3. Equatorial depth–longitude section of Pacific Ocean temperature anomalies (°C) averaged between 5°S and 5°N during (a) DJF 2021/22, (b) MAM 2022, (c) JJA 2022, and (d) SON 2022. The 20°C isotherm (thick solid line) approximates the center of the oceanic thermocline. The gray dashed line shows the climatology of the 20°C isotherm based on 1991–2020. Anomalies are departures from the 1991–2020 period monthly means. Data are from GODAS; Behringer 2007.

(ii) Atmospheric circulation

In 2022, the large-scale tropical atmospheric circulation anomalies were also consistent with La Niña and persisted through the year. Figure 4.4 shows outgoing longwave radiation (OLR) anomalies, which is a proxy for tropical convection and rainfall. Typically, during La Niña, convection is suppressed (positive OLR, brown shading) over the western and central tropical Pacific and enhanced (negative OLR, green shading) over the Maritime Continent. Relative to the other seasons in the year, the dipole-like pattern in precipitation anomalies was shifted eastward

during DJF 2021/22, with suppressed convection located just to the east of the date line and enhanced convection over the western tropical Pacific (Fig. 4.4a). The anomalies then shifted westward after DJF with suppressed convection expanding into the western tropical Pacific and enhanced convection shifting over western Indonesia (Fig. 4.4b). During MAM 2022, convection over the date line was further suppressed, which occurred at the same time the ONI value reached its peak. Corresponding to the seasonal cycle, the region of enhanced precipitation over the Maritime Continent extended farther northwards toward the Philippines during DJF 2021/22 and MAM 2022. Following boreal spring, enhanced rainfall anomalies became mainly confined to the equator and south of the equator during JJA and SON, with anomalies also increasing in intensity (Figs. 4.4c,d).

Similar to convection, the lower- and upper-level wind anomalies were reflective of La Niña throughout the year. Stretching across most of the equatorial Pacific Ocean (Fig. 4.5), the tropical low-level 850-hPa easterly trade winds were enhanced. The low-level easterly wind anomalies were strongest over the eastern Pacific during DJF 2021/22 (Fig. 4.5a). During the other seasons (MAM through SON), the low-level easterly wind anomalies strengthened and expanded over the western tropical Pacific Ocean (Figs. 4.5b–d). The upper-level 200-hPa westerly wind anomalies prevailed throughout the year over most of the equatorial Pacific Ocean (Fig. 4.6). Like the low-level winds, upper-level westerly wind anomalies also expanded farther to the west after DJF (Figs. 4.6b–d). During all seasons, an anomalous cyclonic circulation couplet straddled the equator in both hemispheres (Fig. 4.6). At times, two pairs of cyclonic anomalies were evident, such as in MAM 2022, with centers around 160°E and 120°W, respectively. Overall, the lower- and

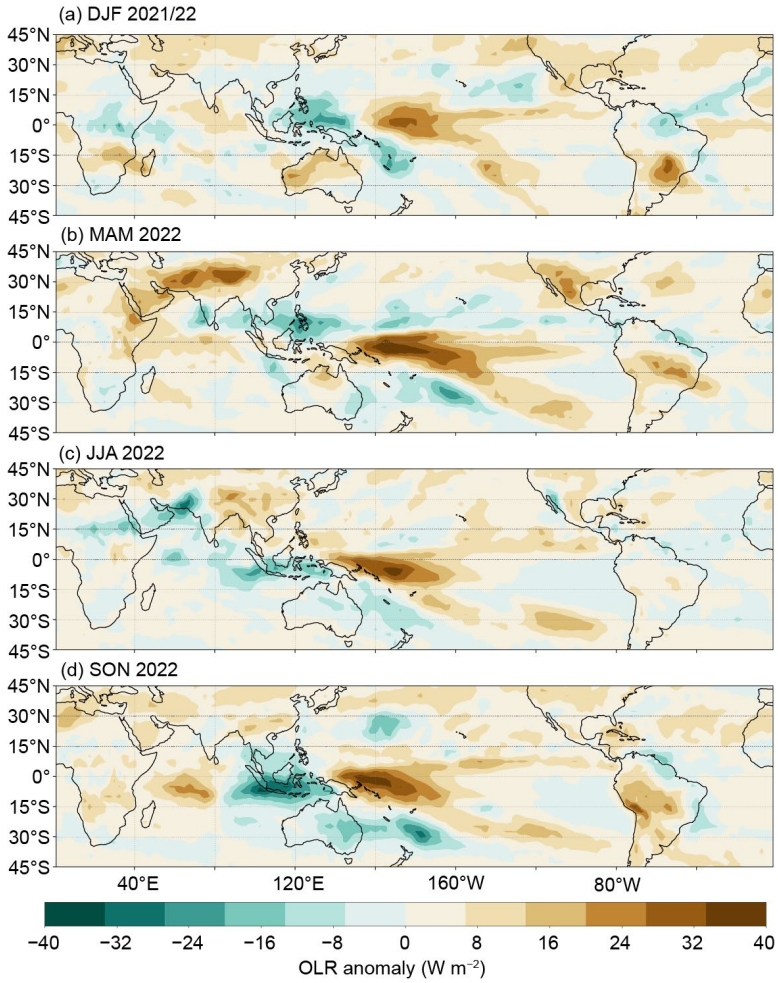

Fig. 4.4. Outgoing longwave radiation (OLR) anomalies (W m^{-2}) during (a) DJF 2021/22, (b) MAM 2022, (c) JJA 2022, and (d) SON 2022. Anomalies are departures from the 1991–2020 period monthly means. Data are from Liebmann and Smith (1996).

upper-level wind anomalies (Figs. 4.5, 4.6) and rainfall anomalies across the tropical Pacific (Fig. 4.4) were indicative of an enhanced equatorial Walker circulation over the tropical Pacific. Collectively, these oceanic and atmospheric anomalies reflected the well-known, basin-wide atmospheric and oceanic coupling of the La Niña phenomenon (Bjerknes 1969).

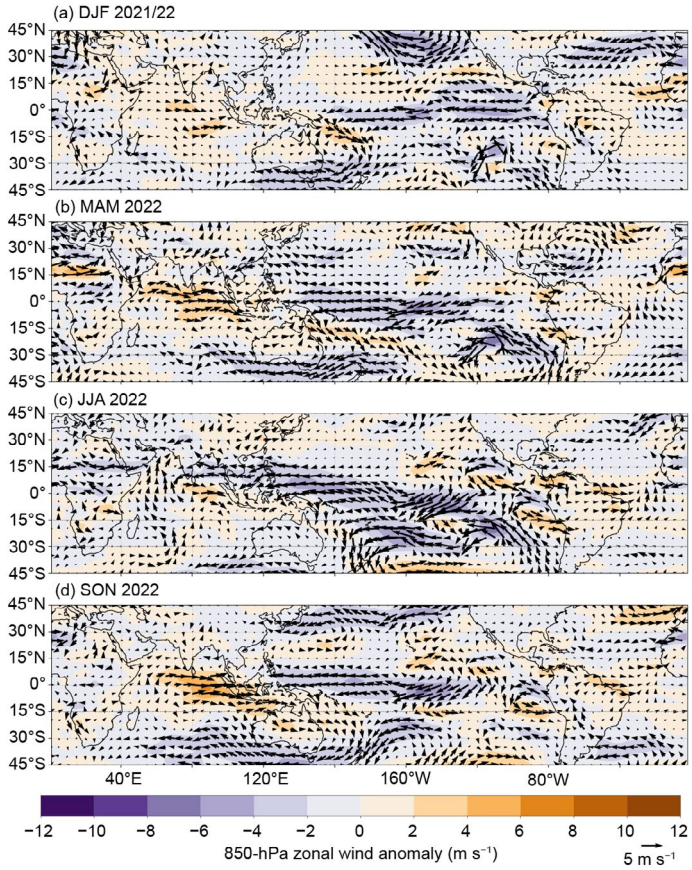

Fig. 4.5. Anomalous 850-hPa wind vectors and zonal wind speed (shading) during (a) DJF 2021/22, (b) MAM 2022, (c) JJA 2022, and (d) SON 2022. The reference wind vector is located at the bottom right. Anomalies are departures from the 1991–2020 period monthly means. Data are from the NCEP/NCAR reanalysis (Kalnay et al. 1996).

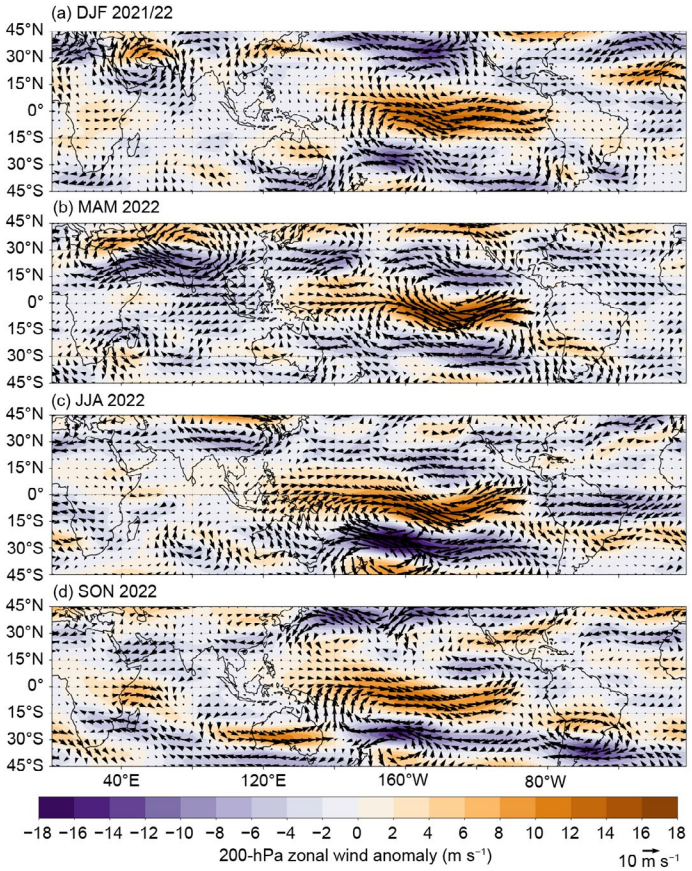

Fig. 4.6. Anomalous 200-hPa wind vectors and zonal wind speed (shading) during (a) DJF 2021/22, (b) MAM 2022, (c) JJA 2022, and (d) SON 2022. The reference wind vector is located at the bottom right. Anomalies are departures from the 1991–2020 period monthly means. Data are from the NCEP/NCAR reanalysis (Kalnay et al. 1996).

(iii) Global precipitation

ENSO-driven teleconnections can affect extratropical precipitation anomalies globally (Bjerknes 1969; Ropelewski and Halpert 1989). During JJA 2022, impacts were weaker and more confined to the immediate tropics and to the Southern Hemisphere, as is typical for this season (Appendix Fig. A4.1a). Enhanced precipitation was evident across some stations in Indonesia and eastern Australia. Drier-than-normal conditions were found over the southernmost parts of South America, while wetter conditions were observed over much of northern South America. During SON 2022, wetter-than-normal conditions remained over Indonesia and spread to northern Australia (Appendix Fig. A4.1b). Over southeastern China, drier-than-normal conditions were evident. Drier-than-normal conditions also remained over southern Brazil and Uruguay, while increased precipitation expanded to eastern Brazil and continued to influence parts of northern South America. Enhanced rainfall was present over central India, along with below-average rainfall over southern India and Sri Lanka, as is typical for La Niña.

c. Tropical intraseasonal activity

—A. Allgood and C. J. Schreck

Organized tropical intraseasonal activity is modulated by several different modes of coherent atmospheric variability, most notably the Madden-Julian Oscillation (MJO; Madden and Julian 1971, 1972, 1994; Zhang 2005). The MJO is characterized by eastward-propagating envelopes of large-scale anomalous enhanced and suppressed convection that typically circumnavigate the globe in a 30–60-day period. MJO-related convective anomalies are similar in spatial extent to those generated by the atmospheric response to the El Niño–Southern Oscillation (ENSO), but the latter signal remains largely stationary and lasts for at least several months. Other impactful modes of variability include convectively coupled atmospheric waves, such as Kelvin waves, which exhibit a faster phase speed than the MJO, and westward-propagating equatorial Rossby waves (Wheeler and Kiladis 1999; Kiladis et al. 2009). These waves are typically narrower zonally than the MJO and may not couple as well to the broader convective regime. Therefore, the MJO typically generates the strongest extratropical responses (Kiladis and Weickmann 1992; Riddle et al. 2012; Baxter et al. 2014) and plays a role in modulating both monsoonal activity (Krishnamurti and Subrahmanyam 1982; Lau and Waliser 2012) and tropical cyclone activity (Mo 2000; Frank and Roundy 2006; Camargo et al. 2009; Schreck et al. 2012; Diamond and Renwick 2015).

The MJO can exhibit sustained periods of robust activity as well as periods of weak or indiscernible activity (Matthews 2008). Active periods can be diagnosed through time–longitude analyses of various atmospheric fields, including anomalous outgoing longwave radiation (OLR; Fig. 4.7a), anomalous 200-hPa velocity potential (Fig. 4.7b), and anomalous zonal winds at 200-hPa and 850-hPa (Fig. 4.8a). OLR can be used as a proxy for convective anomalies due to the

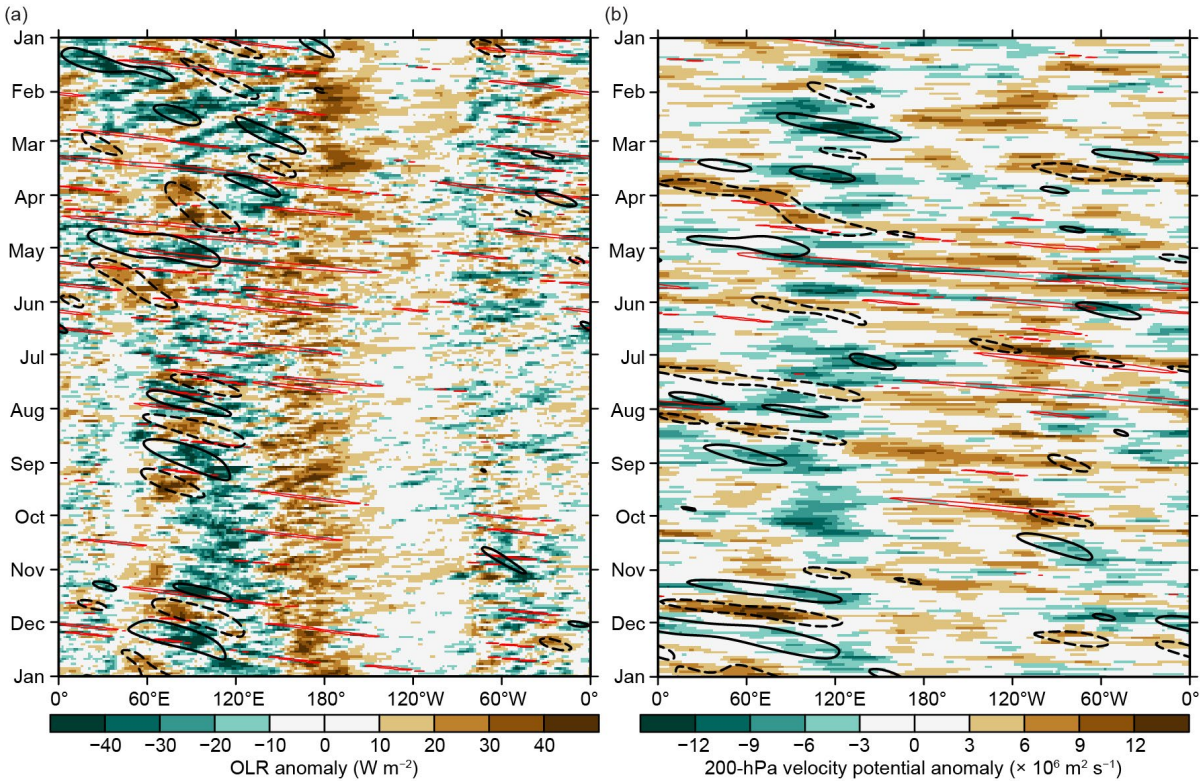

Fig. 4.7. (a) Time–longitude section with (a) outgoing longwave radiation (OLR) anomalies (W m^{-2}; Schreck et al. 2018) and (b) 200-hPa velocity potential anomalies (× 10^6 m^2 s^{-1}) from the CFSR (Saha et al. 2014). Both variables are averaged over 10°S–10°N. Time increases downward on this graph, beginning with Jan 2022 at the top and ending with Jan 2023 at the bottom. Negative anomalies indicate enhanced convection, and positive anomalies indicate suppressed convection. Contours identify anomalies filtered for the Madden-Julian Oscillation (MJO; black) and atmospheric Kelvin waves (red). Contours are drawn at ±12 W m^{-2} and ±4 × 10^6 m^2 s^{-1} with the enhanced (suppressed) convective phase of these phenomena indicated by solid (dashed, MJO only) contours. Anomalies are departures from the 1991–2020 base period daily means.

strong connection between OLR and high cloud cover typically generated by thunderstorm activity in the tropics. MJO activity appears on Figs. 4.7 and 4.8a as coherent opposite-signed anomaly couplets that propagate eastward with time. Filtering these analyses for the wavelengths and periods associated with the MJO diagnoses its activity. Another diagnostic tool frequently used to identify MJO activity is the Wheeler-Hendon (2004) Real-time Multivariate MJO (RMM) index, which identifies the MJO from a combined signal in OLR and zonal winds at 850 hPa and 200 hPa. In RMM plots, robust atmospheric anomalies on a spatial scale resembling the MJO appear as a signal outside of the unit circle, and eastward propagation is represented by counterclockwise looping of the index about the origin (Fig. 4.9).

La Niña conditions persisted throughout 2022, which had a weakening effect on MJO activity due to destructive interference between the MJO-enhanced convective envelope and negative sea-surface temperature anomalies and enhanced trade winds across the equatorial Pacific, which in turn served to suppress widespread organized convection (Hendon et al. 1999; Zhang and Gottschalck 2002; Zhang 2005). Therefore, it is typical when La Niña conditions are present for MJO events that initiate over the Indian Ocean to strengthen as the enhanced convection reaches the Maritime Continent but weaken as they propagate to the Pacific. MJO activity was incoherent at the start of the year, although an active MJO signal that crossed the Pacific in late 2022 helped initiate a downwelling oceanic Kelvin wave that brought warm water from the West Pacific Warm Pool eastward across much of the basin (Fig. 4.8b).

The first period of somewhat sustained MJO activity during 2022 began in February and lasted through April, with most of the events initiating over the Indian Ocean and weakening as the enhanced convective envelopes reached the West Pacific. During May and June, eastward propagating signals continued to circumnavigate the globe, but the phase speeds of these signals were more consistent with unusually strong and convectively-coupled atmospheric Kelvin waves (Fig. 4.7, red contours). Despite the poor depiction on the MJO filtering of the time–longitude

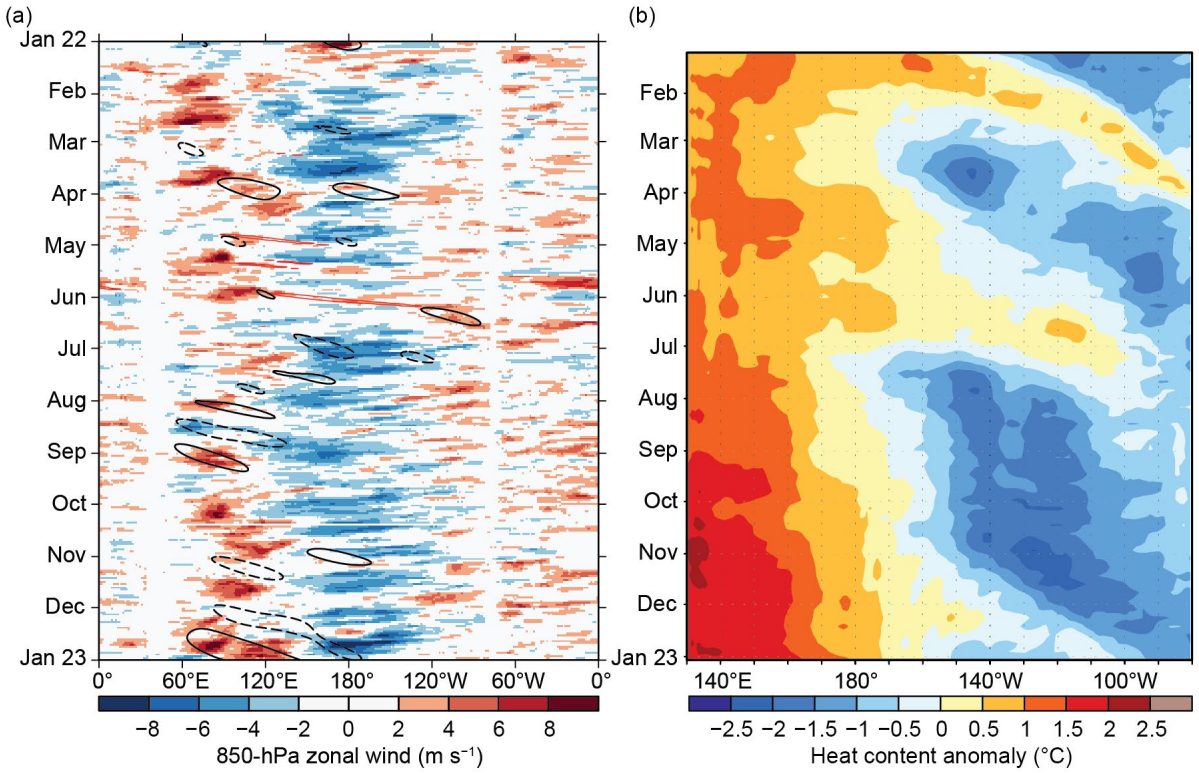

Fig. 4.8. (a) Time–longitude section for 2022 of anomalous 850-hPa zonal wind (m s^{-1}) averaged between 10°S and 10°N. Contours identify anomalies filtered for the Madden-Julian Oscillation (MJO; black) and atmospheric Kelvin waves (red). (b) Time–longitude section for 2022 of the anomalous equatorial Pacific Ocean heat content, calculated as the mean temperature anomaly (°C) between 0-m and 300-m depth. Yellow/red (blue) shading indicates above- (below-) average heat content. Relative warming (dashed lines) and cooling (dotted lines) due to downwelling and upwelling equatorial oceanic Kelvin waves are indicated. Anomalies are departures from the 1991–2020 base period pentad means. Data in (b) are derived from GODAS (Behringer et al. 1998).

diagrams due to the faster phase speeds, this strong Kelvin wave activity projected strongly on the RMM-index diagrams (Fig. 4.9). Additionally, two subsequent Kelvin wave passages over the Pacific succeeded in generating brief westerly wind bursts near the equator (Fig. 4.8a), which helped generate a second downwelling oceanic Kelvin wave that propagated across the Pacific basin during June and July (Fig. 4.8b). The MJO produced an even stronger trade-wind surge in late June and July, which brought back significant upwelling and cooler water across the central and eastern Pacific. The MJO's enhanced convective phases failed to overcome the strong boreal summer La Niña conditions during July and August.

The MJO became weaker during September and October as the atmospheric response to the ongoing La Niña dominated the global tropical convective pattern. Coherent eastward propagating intraseasonal activity resumed in November and lasted through the end of 2022. During November, this activity was again on the fast side of the 30–60-day MJO circumnavigational period, but the signal began to slow down during December. Towards the end of 2022, the MJO reached the Pacific, though convection associated with the intraseasonal signal was observed primarily off of the equator (not shown) due to destructive interference from the ENSO base state.

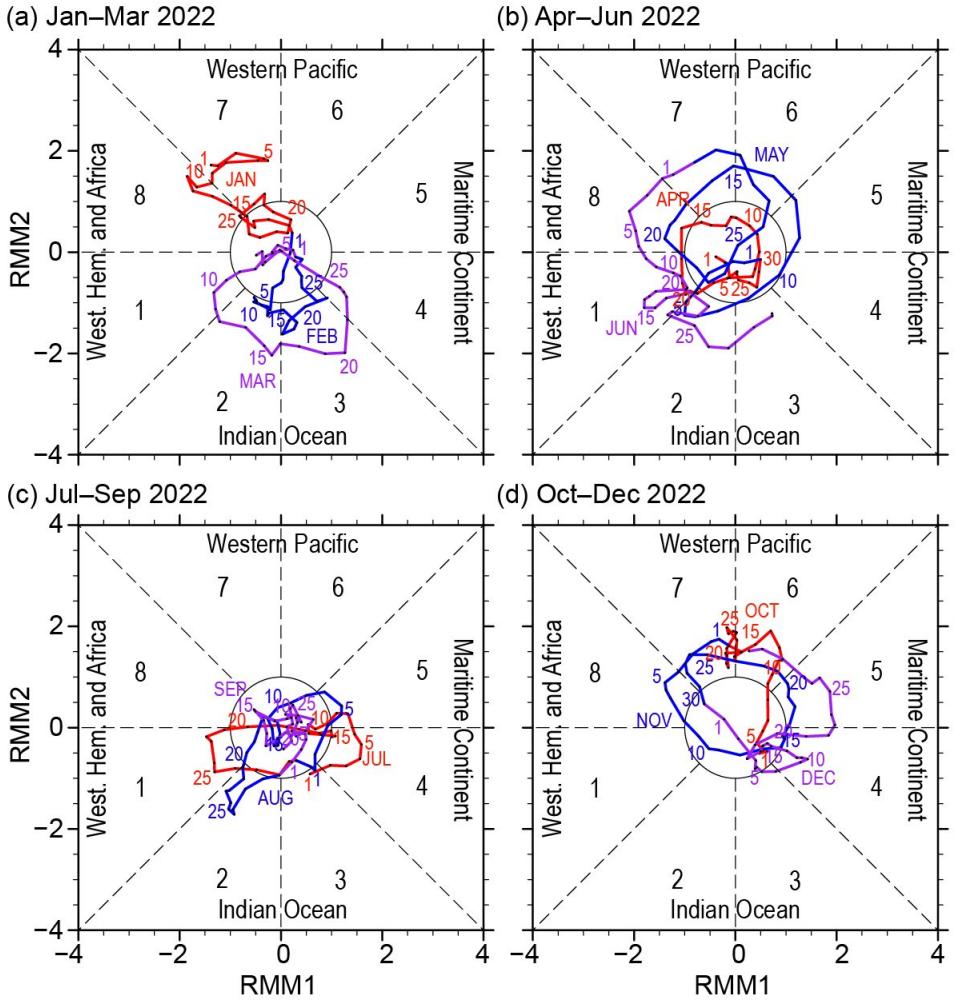

Fig. 4.9. Wheeler and Hendon (2004) Real-time Multivariate Madden-Julian Oscillation (RMM) index for (a) Jan–Mar, (b) Apr–Jun, (c) Jul–Sep, and (d) Oct–Dec 2022. Each point represents the Madden-Julian Oscillation (MJO) amplitude and location on a given day, and the connecting lines illustrate its propagation. Amplitude is indicated by distance from the origin, with points inside the circle representing weak or no MJO. The eight phases around the origin identify the region experiencing enhanced convection, and counter-clockwise movement is consistent with eastward propagation.

d. Intertropical convergence zones

1. PACIFIC

—N. Fauchereau

Tropical Pacific rainfall patterns are dominated by two convergence zones: the Intertropical Convergence Zone (ITCZ; Schneider et al. 2014) north of the equator and the South Pacific Convergence Zone (SPCZ; Vincent 1994) in the southwest Pacific. The position and intensity of these convergence zones throughout the year are highly sensitive to sea-surface temperature anomalies and, therefore, are also highly sensitive to the El Niño–Southern Oscillation (ENSO; Trenberth 1984).

As a whole, the tropical Pacific exhibited precipitation anomalies throughout 2022 that were consistent with the ongoing La Niña conditions. Figure 4.10 summarizes the behavior for both convergence zones during 2022 using rainfall from the Multi-Source Weighted-Ensemble Precipitation (MSWEP) 2.8.0 dataset (Beck et al. 2019). Rainfall transects over 30°S–20°N are presented for each quarter of the year, averaged across successive 30-degree longitude bands, starting in the western Pacific at 150°E–180°. The 2022 seasonal variation is compared against the longer-term 1991–2020 climatology. The transects for January–March (Fig. 4.10a) for the western and central Pacific (150°E–150°W, especially 150°E to the date line) show that the SPCZ was shifted south and west of its climatological position, while rainfall rates within the ITCZ were reduced compared to climatology. This is a signature consistent with typical anomalies recorded in the Southern Hemisphere summer during La Niña.

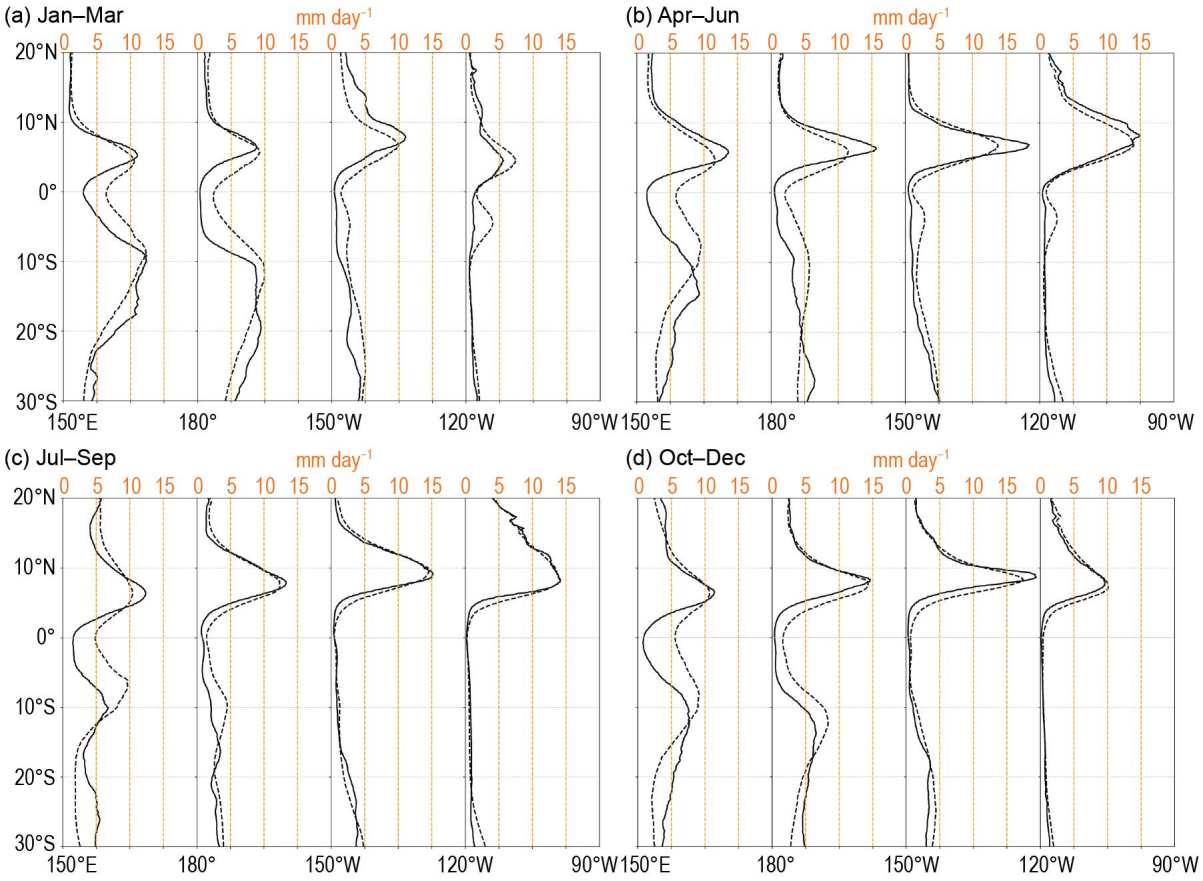

Fig. 4.10. Rainfall rate (mm day^{-1}) for (a) Jan–Mar, (b) Apr–Jun, (c) Jul–Sep, and (d) Oct–Dec 2022. The separate panels for each quarter show the rainfall cross-section between 30°S and 20°N (solid line) and the 1991–2020 climatology (dotted line), separately for four 30° sectors from 150°E–180° to 120°W–90°W. (Source: MSWEP v2.8.0.)

The precipitation anomaly patterns that persisted throughout 2022 in the tropical Pacific are shown in Fig. 4.11, which presents the precipitation anomalies for the period April–June with respect to the 1991–2020 climatological period. As was the case for most of the year, the tropical Pacific rainfall anomalies reflected a northward shift in the ITCZ and a southwestward shift in the SPCZ (Fig. 4.10b). Both of these are typical for La Niña and are reflected by anomalously dry conditions near the equatorial Pacific, with wetter-than-normal conditions to the north and the southwest.

Figure 4.12 shows a more detailed comparison of the western Pacific (150°E–180°) rainfall transect during January–March 2022, corresponding to well-established La Niña conditions, relative to all other years in this dataset. During this three-month period, the recorded rainfall, averaged over all longitudes (black line), closely corresponds to the rainfall rates recorded on average for all La Niña years (thick blue line).

In summary, precipitation anomaly patterns throughout 2022 as a whole indicated that the ITCZ was shifted north of its climatological position, while the SPCZ was shifted southwest of its climatological position. These variations in intensity and position of the Pacific convergence zones were consistent with typical anomalies recorded over the historical period during La Niña events.

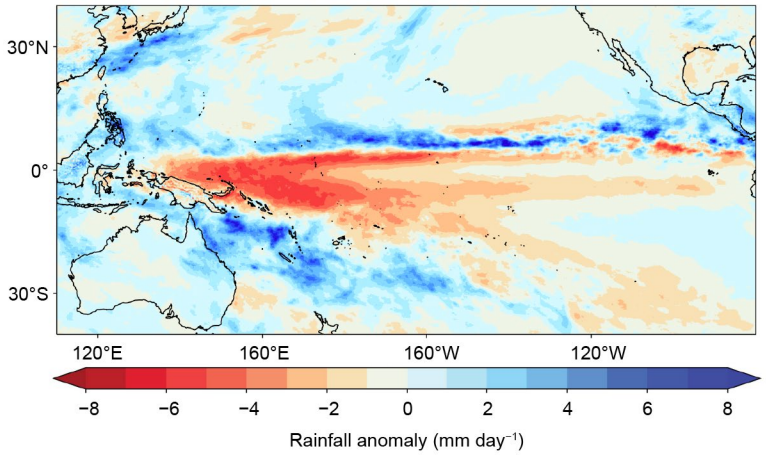

Fig. 4.11. Rainfall anomalies (mm day^{-1}) for Apr–Jun 2022. The anomalies are calculated with respect to the 1991–2020 climatology. (Source: MSWEP v2.8.0.)

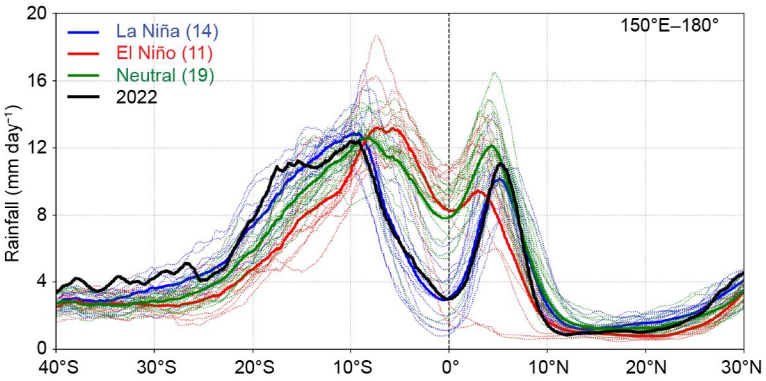

Fig. 4.12. Rainfall rate (mm day^{-1}) for the Jan–Mar 2022 quarter, for each year from 1979 to 2022, averaged over the longitude sector 150°W–180°E. The cross-sections are color-coded according to NOAA's Oceanic Niño Index (with a threshold of ±0.5°C), except 2022 which is shown in black. Dotted lines are individual years, and solid lines are the average overall years in each ENSO phase. The inset legend indicates how many years went into each composite. (Source: MSWEP v2.8.0.)

2. ATLANTIC

—A. B. Pezza and C. A. S. Coelho

The Atlantic ITCZ is a well-organized convective band that oscillates between approximately 5°N–12°N during July–November and 5°S–5°N during January–May (Waliser and Gautier 1993; Nobre and Shukla 1996). Equatorial atmospheric Kelvin waves can modulate ITCZ intraseasonal variability (Guo et al. 2014). ENSO and the Southern Annular Mode (SAM) can also influence the ITCZ on interannual time scales (Münnich and Neelin 2005). The SAM, also known as the Antarctic Oscillation, describes the north–south movement of the westerly wind belt that circles Antarctica. A positive SAM event reflects a contraction of the westerly wind belt away from the equator, with stronger subtropical ridges and less precipitation in the midlatitudes (Ding et al. 2012; Liu et al. 2021; Moreno et al. 2018).

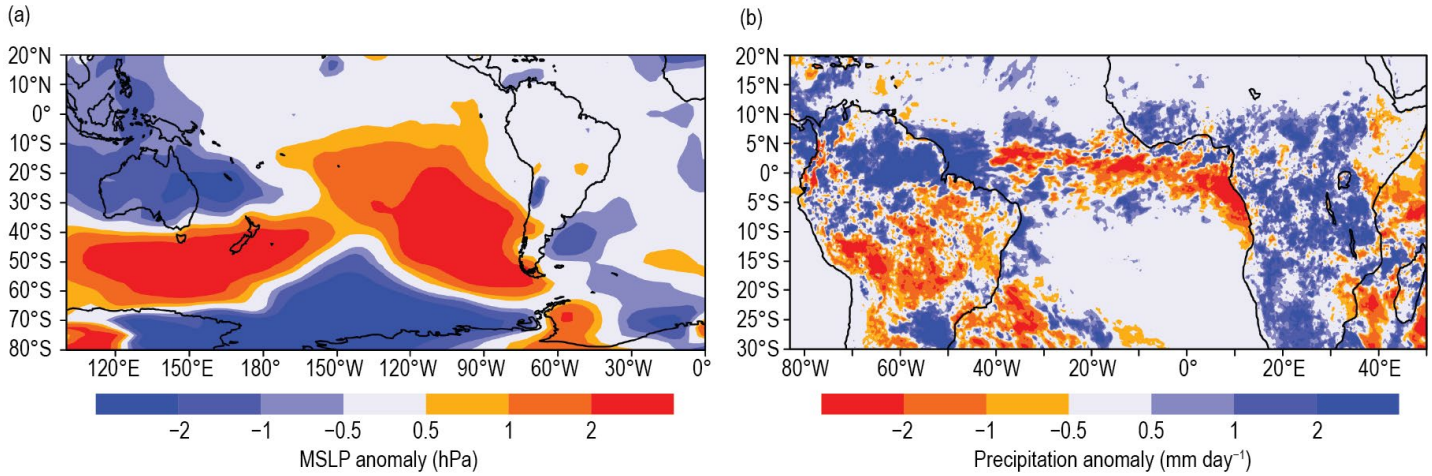

Fig. 4.13. Jan–May (a) South American and high-latitude mean sea-level pressure (MSLP) anomalies (hPa; Kalnay et al. 1996), and (b) precipitation anomalies (mm day^{-1}) over the Atlantic sector. MSLP anomalies are calculated with respect to the 1991–2020 climatology and are derived from NCEP/NCAR reanalysis (Kalnay et al. 1996). Precipitation anomalies are calculated with respect to the 2001–2021 climatology and are derived from IMERG (Huffman et al. 2014).

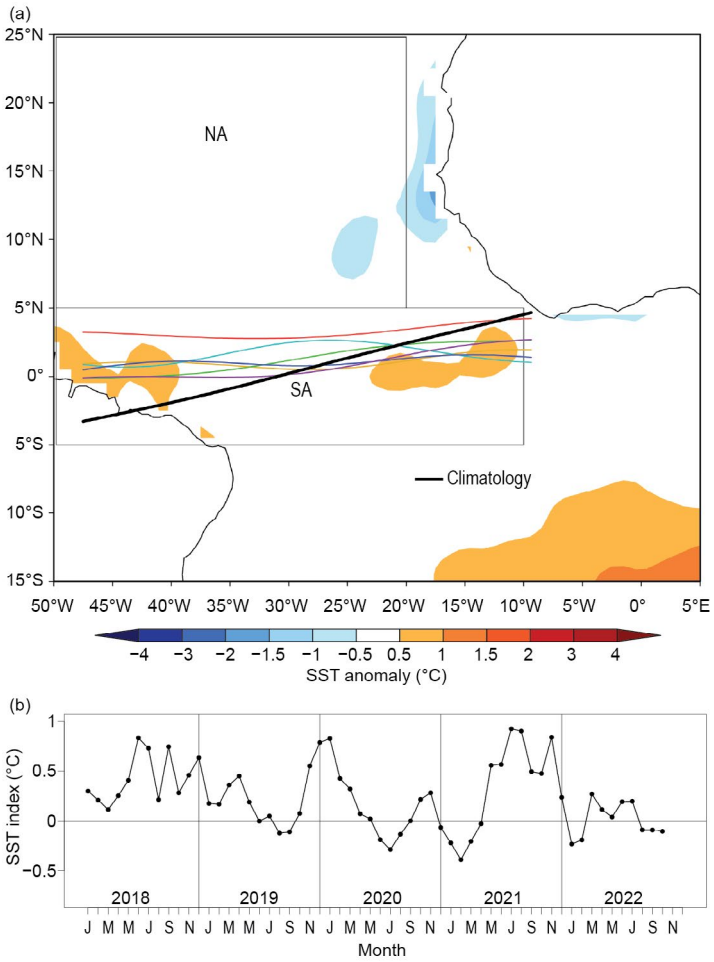

The Atlantic responded to the ongoing La Niña in a way that was similar to what was observed in 2021. Higher-than-normal pressure prevailed over the South Pacific and Patagonia during the key ITCZ period of influence (i.e., January–May; Fig. 4.13a). The Atlantic featured a weakened subtropical anticyclone with above-average precipitation over coastal northeastern and southern Brazil (Figs. 4.13a,b). Over other areas of inland Brazil, a precipitation deficit was observed during the ITCZ active period, highlighting a pronounced lack of balance in response to the irregularity of the dynamic flow. This pattern was accompanied by a largely positive SAM, as seen by the negative pressure anomalies at subpolar latitudes over the Pacific (Fig. 4.13a). The movement of the ITCZ and the Atlantic Index (see Fig. 4.14 for definition) were near normal (i.e., close to climatology) over the central Atlantic, while the ITCZ was north of its climatological position near the north coast of Brazil. This pattern was associated with low-level wind convergence slightly north of the equator at the start of the year (not shown).

Fig. 4.14. (a) Atlantic Intertropical Convergence Zone (ITCZ) position inferred from outgoing longwave radiation (Liebmann and Smith 1996) during Mar 2022. The colored thin lines indicate the approximate position for the six pentads of the month. The black thick line indicates the Atlantic ITCZ climatological position for Mar. The sea-surface temperature (SST) anomalies (°C) for Mar 2022 calculated with respect to the 1982–2020 climatology are shaded. The two boxes indicate the areas used for the calculation of the Atlantic index in panel (b), which shows the monthly OISST (Reynolds et al. 2002) anomaly time series averaged over the South Atlantic sector (SA region: 5°S–5°N, 10°W–50°W) minus the SST anomaly time series averaged over the North Atlantic sector (NA region: 5°N–25°N, 20°W–50°W) for the period 2017–22, forming the Atlantic index. The positive phase of the index indicates favorable conditions for enhanced Atlantic ITCZ activity south of the equator.

e. Global monsoon summary

—B. Wang and Q. He

Globally, monsoon activity is the dominant mode of annual precipitation and circulation variability and one of the defining features of Earth's climate system (Wang and Ding 2008). Here, we summarize the global and regional monsoon precipitation anomalies in the 2022 monsoon year, which includes the Southern Hemisphere (SH) summer (November 2021–April 2022) and Northern Hemisphere (NH) summer (May–October 2022) monsoons. Figure 4.15 presents the monsoon domain (red lines) defined by rainfall characteristics (rainy summer versus dry winter; Wang 1994) rather than the traditional definition by winds (Ramage 1971). The NH monsoon includes five regional monsoons: northern Africa, India, East Asia, the western North Pacific, and North America. The SH monsoon consists of three monsoons: southern Africa, Australia, and South America.

We use regional monsoon precipitation and circulation indices to measure the integrated regional monsoon intensity. The precipitation indices represent the anomalous precipitation rate averaged over the blue rectangular box regions shown in Fig. 4.15. The precipitation averaged in each blue box well represents the precipitation averaged over the entire corresponding regional monsoon domain (r >0.90; Yim et al. 2014). The definitions of the circulation indices for each monsoon region are provided in Table 4.1. Circulation indices are defined by the meridional shear of the zonal winds at 850 hPa, which measures the intensity (relative vorticity) of the monsoon troughs, except for the northern African and East Asian monsoons. The northern African monsoon circulation index is defined by the westerly monsoon strength, reflecting the

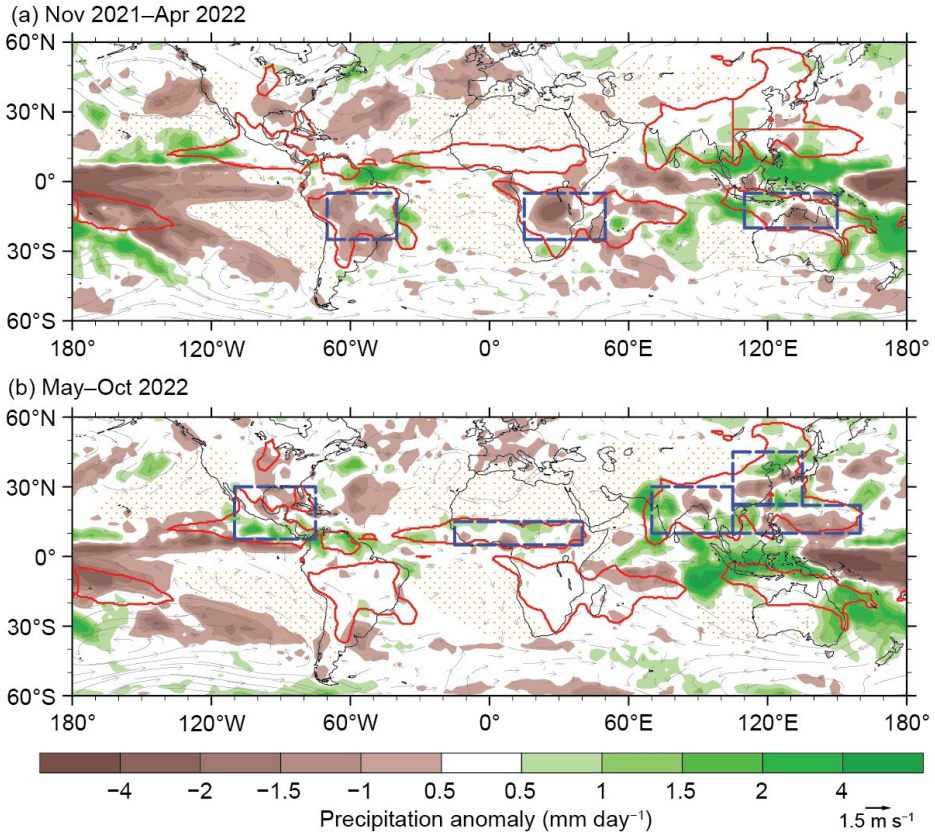

Fig. 4.15. Seasonal mean precipitation anomalies (mm day^{-1}) and 850-hPa wind anomalies (m s^{-1}) for (a) the Southern Hemisphere (SH) summer monsoon season: Nov 2021–Apr 2022 and (b) the Northern Hemisphere (NH) summer monsoon season: May–Oct 2022. The anomalies are departures from the 1991–2020 climatology. Red lines outline the global monsoon precipitation domain. Two criteria define the monsoon domains: 1) the annual precipitation range (summer-minus-winter mean) exceeds 300 mm, and 2) the summer precipitation is >55% of the total annual precipitation amount, where summer here means May–Sep for the NH and Nov–Mar for the SH (Wang and Ding 2008). The blue rectangular boxes denote the regions where the regional monsoon precipitation indices are measured. The dotted area represents the dry region where the local summer precipitation rate is below 1 mm day^{-1}. (Source: GPCP; Huffman et al. 2009.)

north–south thermal contrast between the South and North Atlantic. The East Asian summer monsoon (EASM) circulation index is determined by the meridional wind strength, reflecting the east–west thermal contrast between the Asian continent and the western North Pacific. The precipitation and circulation indices are well correlated for most regional monsoons, with correlation coefficients ranging from 0.70 to 0.88 (Table 4.1). Thus, the precipitation and circulation indices generally provide consistent measurements of the strength of each regional monsoon system except over the southern African monsoon region.

Table 4.1. Definition of the regional summer monsoon circulation indices and their correlation coefficients with the corresponding regional summer monsoon precipitation indices for 1979/80–2021/22. The precipitation indices are defined by the areal mean precipitation anomalies over the blue box regions shown in Fig. 4.15. R (r) represents the correlation coefficient between the total (land) monsoon precipitation and the corresponding circulation index. The correlation coefficients were computed using monthly time series (172 summer months; Jun–Sep in NH [1980–2022] and Dec–Mar in SH [1979/80–2021/22]). Bolded numbers represent significance at the 99% confidence level.

Regional monsoon	Definition of the circulation index	R (r)
Indian (ISM)	U850 (5°N–15°N, 40°E–80°E) minus U850 (25°N–35°N, 70°E–90°E)	**0.72 (0.60)**
Western North Pacific (WNPSM)	U850 (5°N–15°N, 100°E–130°E) minus U850 (20N°–35°N, 110°E–140°E)	**0.87 (0.72)**
East Asian (EASM)	V850 (20°N–35°N, 120°E–140°E) plus V850 (10°N–25°N, 105°E–115°E)	**0.73 (0.72)**
North American (NASM)	U850 (5°N–15°N, 130°W–100°W) minus U850 (20°N–30°N, 110°W–80°W)	**0.85 (0.78)**
Northern African (NAFSM)	U850 (0°–10°N, 40°W–10°E)	**0.70 (0.70)**
South American (SASM)	U850 (20°S–5°S, 70°W–40°W) minus U850 (35°S–20°S, 70°W–40°W)	**0.81 (0.81)**
Southern African (SAFSM)	U850 (12°S–2°S, 10°W–30°E) minus V850 (30S°–10°S, 40°E–60°E)	**0.58 (0.47)**
Australian (AUSSM)	U850 (15°S–0°, 90°E–130°E) minus U850 (30°S–20°S, 100°E–140°E)	**0.88 (0.80)**

During the 2021/22 SH summer, the La Niña-enhanced Walker circulation contributed to suppressed rainfall over the central-eastern Pacific and to increased rainfall over the northern Maritime Continent and southeast Asia and the adjacent seas (Fig. 4.15a). Precipitation was significantly reduced over the South American and southern African monsoon regions, as well as northern Australia (Fig. 4.15a). Figure 4.16 shows areal-averaged monsoon intensities. The Australian summer monsoon precipitation showed average precipitation intensity and slightly above-normal circulation intensity (Fig. 4.16g). The South American monsoon precipitation was 1 standard deviation (std. dev.) below normal, but the related circulation's strength was 0.5 std. dev. above normal (Fig. 4.16h). The southern African summer monsoon precipitation was 2 std. dev. below normal, with the circulation intensity 1 std. dev. below normal (Fig. 4.16f). Overall, the South American and southern African monsoons, as well as the northern Australian monsoon, responded uncharacteristically to the 2021/22 La Niña because La Niña conditions normally increase SH monsoon rainfall. The reasons for these uncharacteristic responses remain to be explored.

During the 2022 NH summer monsoon season (May–October), La Niña continued with the Niño-3.4 SST anomaly around –0.8°C to –1.0°C. Different from the SH monsoon, the NH summer monsoon responds to La Niña and follows a traditional pattern. Precipitation over the Maritime Continent was significantly above normal, but a noticeable reduction of precipitation occurred in the equatorial western Pacific and the Philippine Sea (Fig. 4.15b). Notably, the Indian summer monsoon was abundant and Pakistan experienced record flooding. The Indian summer monsoon precipitation and circulation indices were about 1 std. dev. above normal (Fig. 4.16b). Over East

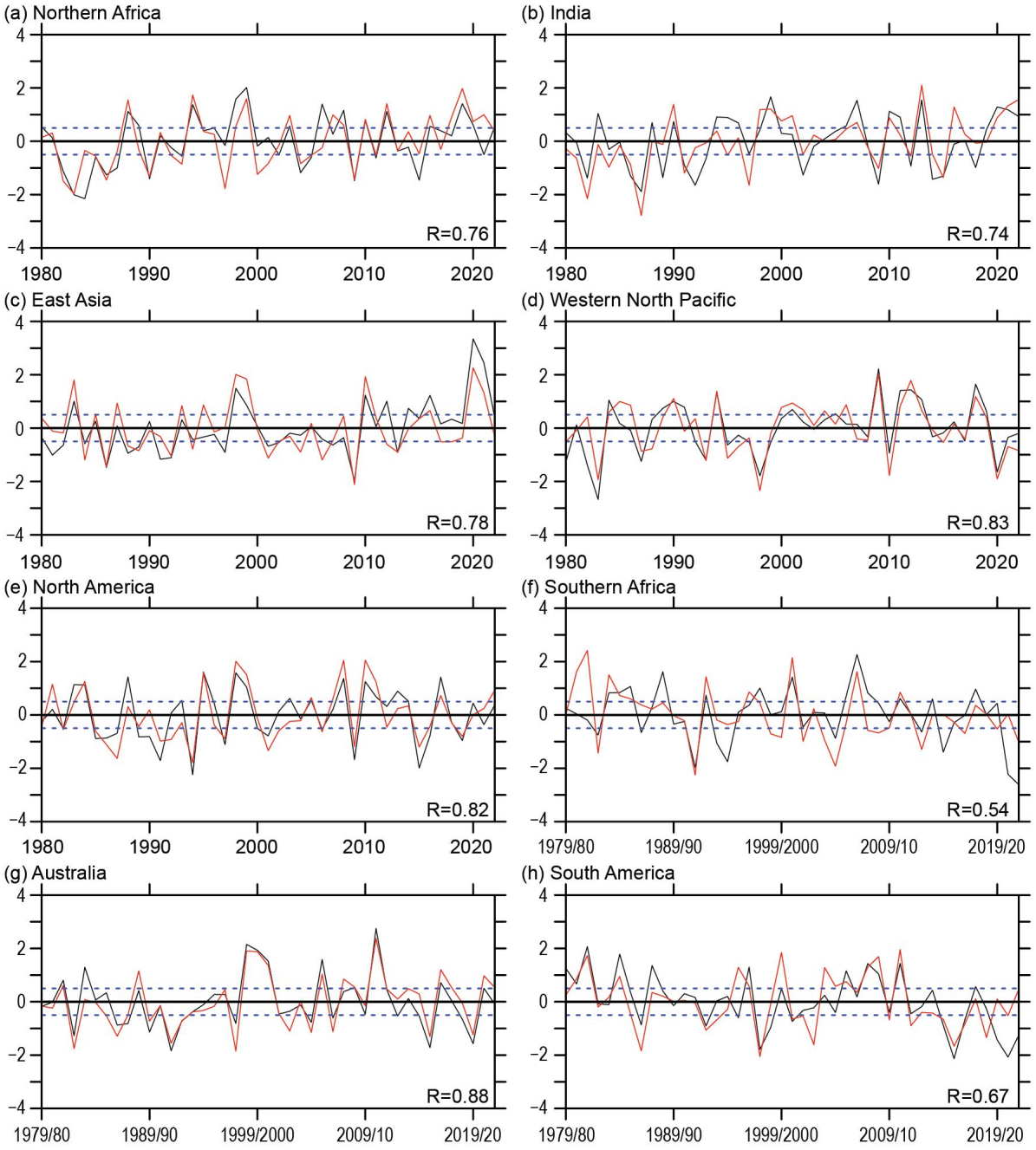

Fig. 4.16. (a)–(h). Temporal variations of summer monsoon precipitation (black lines) and low-level circulation (red lines) indices for eight regional monsoons. The precipitation indices represent the anomalous precipitation rate averaged over the blue rectangular box regions shown in Fig. 4.15. The corresponding circulation indices are defined in Table 4.1. All indices were normalized by their corresponding standard deviation (ordinate) derived for the period of 1979/80–2021/22. Numbers shown in the bottom right of each panel denote the correlation coefficient between the seasonal mean precipitation and circulation indices (sample size: 43). Dashed lines indicate ±0.5 std. dev. The summer monsoon seasons are May–Oct for the Northern Hemisphere and Nov–Apr for the Southern Hemisphere. (Data source: GPCP for precipitation; ERA5 [Hersbach et al. 2020] for circulation).

Asia, drought conditions dominated the East Asian subtropical front zone (Meiyu/Baiu/Changma), whereas northern China experienced abundant rainfall (Fig. 4.15b). Northern African and North American monsoons had near-normal conditions (Figs. 4.16a,e). The western North Pacific oceanic monsoon circulation index was below normal (Fig. 4.16d).

Monsoon rainfall over land has more important socioeconomic impacts than oceanic monsoon rainfall. Therefore, we specifically examine land monsoon rainfall (LMR). The NH and SH LMR indices were computed by averaging precipitation over the corresponding land areas within the monsoon domain. The LMR on a global scale is significantly influenced by the El Niño–Southern Oscillation (Wang et al. 2012). Figure 4.17 shows that the NH and SH land summer monsoon precipitation are anti-correlated with the simultaneous Niño-3.4 index. The NH land monsoon rainfall has a simultaneous correlation of −0.75 from 1980 to 2022 (Fig. 4.17a). The SH land monsoon rainfall and Niño-3.4 index also had a negative correlation of −0.75 during 1979/80–2019/20. However, in the past two years the SH land monsoon and Niño-3.4 indices have both been negative (Fig. 4.17b) such that the correlation coefficient for 1979/80–2021/22 is only −0.58. Further investigation is required to determine why the relationship has reversed in the past two years.

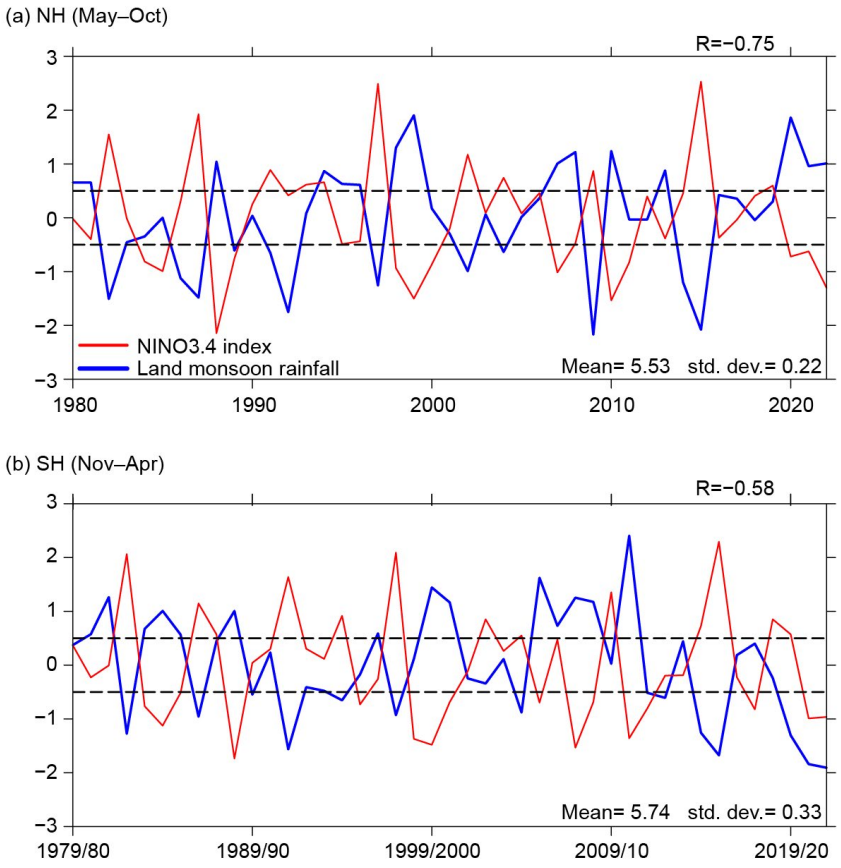

Fig. 4.17. (a) Northern Hemisphere (NH) summer (May–Oct) land monsoon precipitation anomaly (blue) normalized by its standard deviation (std. dev.). The climatological mean NH summer land monsoon precipitation (mean) and std. dev. are shown in the lower right panel (mm day^{-1}). Numbers shown in each panel's top right denote the correlation coefficient (R) between the seasonal mean precipitation anomaly and the simultaneous Niño-3.4 index (red). Dashed lines indicate ±0.5. (b) As in (a) except for the Southern Hemisphere (SH) summer (Nov–Apr). Note that the land monsoon precipitation excludes the monsoon rainfall over the oceanic monsoon domain. (Source: GPCP for precipitation; HadISST and ERSSTv5 for SST.)

f. Indian Ocean dipole

—L. Chen and J.-J. Luo

The Indian Ocean dipole (IOD) is the dominant interannual mode in the tropical Indian Ocean (IO), characterized by a zonal dipole of sea-surface temperature (SST) anomalies in the equatorial IO (Saji et al. 1999; Luo et al. 2010, 2012). The IOD originates from local air–sea interaction processes in the tropical IO and/or the tropical El Niño–Southern Oscillation (ENSO) forcing (Luo et al. 2007, 2010). The dipole usually develops in austral autumn and winter, matures in spring, and terminates rapidly in early austral summer. A negative IOD event is characterized by anomalously high SSTs in the eastern IO and below-average SSTs in the western IO and vice versa for a positive IOD. The IOD phenomenon shows a strong nonlinear feature; that is, a positive IOD is usually stronger than a negative IOD due to the asymmetric air–sea feedback strength between the two phases (Luo et al. 2007; Hong et al. 2008).

In 2022, the tropical IO exhibited a strong negative IOD event with significant positive SST anomalies in the eastern pole and negative SST anomalies in the western pole (Fig. 4.18a). The IOD index of this event reached a seasonal average of –0.9°C in September–November 2022 based on the Optimum Interpolation Sea Surface Temperature (OISST) dataset (Fig. 4.18b, green line). The negative IOD event in 2022 was one of the strongest such events of the past 41 years (since 1982; Fig. 4.19).

The strong negative IOD started to develop in boreal spring 2022 and peaked in boreal summer and autumn (Fig. 4.18b). Following a weak negative IOD event in 2021, the tropical IO exhibited a weak positive Indian Ocean basin (IOB) mode from December 2021 to April 2022 (Figs. 4.18a,b). Beginning in April–May 2022, the anomalous warmth across the basin transitioned into an anomalous dipole, with warm SST anomalies over the eastern IO and cold SST anomalies over the western IO that then began to grow (Fig. 4.18a). Meanwhile,

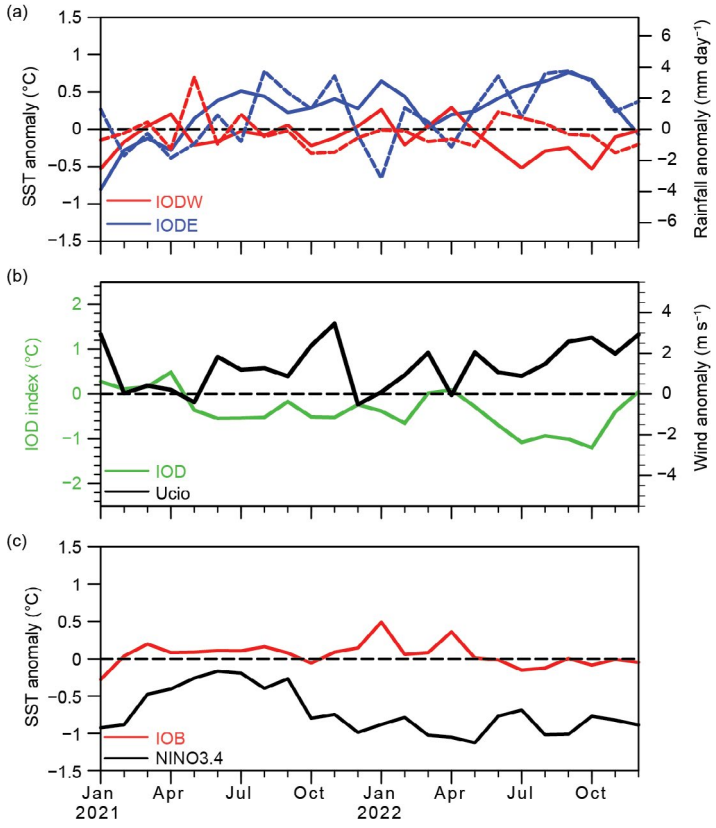

Fig. 4.18. (a) Monthly anomalies of sea-surface temperature (SST; °C; solid lines) and precipitation (mm day^{-1}; dashed lines) of the Indian Ocean dipole (IOD) in the eastern pole (IODE; 10°S–0°, 90°E–110°E; blue lines) and the western pole (IODW; 10°S–10°N, 50°E–70°E; red lines). (b) As in (a), but for the IOD index (measured by the SST difference between IODW and IODE, green line) and surface zonal wind anomaly (m s^{-1}) in the central equatorial IO (Ucio; 5°S–5°N, 70°E–90°E; black line). (c) As in (a), but for the SST anomalies in the Niño-3.4 region (5°S–5°N, 170°W–120°W; black line) and the tropical IO (IOB; 20°S–10°N, 40°E–120°E; red line). Anomalies are relative to the 1982–2022 base period. (Sources: NOAA OISST [Reynolds et al. 2002]; monthly CMAP precipitation analysis [http://ftpprd.ncep.noaa.gov/pub/precip/cmap/]; and JRA-55 atmospheric reanalysis [Ebita et al. 2011].)

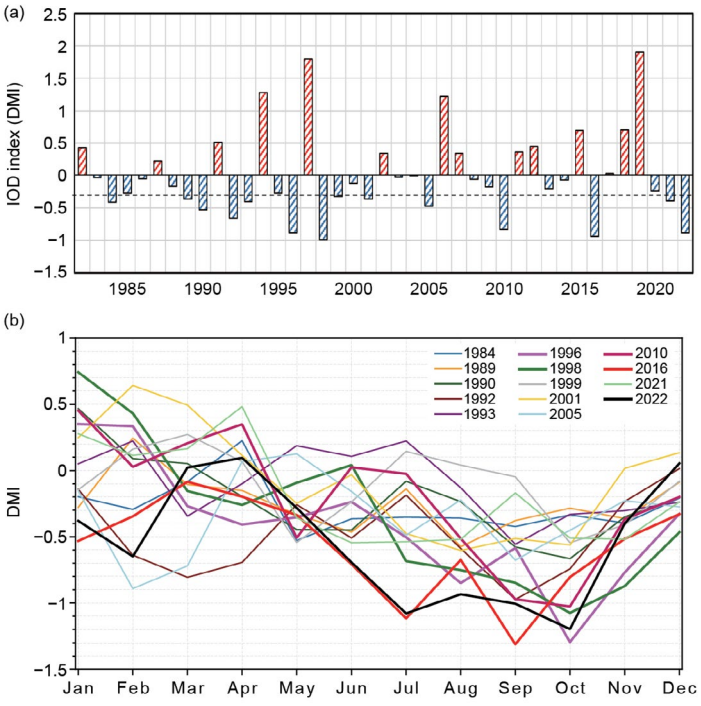

Fig. 4.19. (a) Sep–Nov IOD index (DMI) based on sea-surface temperature (SST) data from OISSTv2. (b) Annual DMI time series for all negative IOD events.

westerly surface wind anomalies occurred over the central IO region during that same period (Fig. 4.18b; see also Fig. 4.5). From the perspective of the tropical Indo-Pacific Ocean, these westerly wind anomalies over the central IO region can be associated with La Niña in the tropical Pacific (Fig. 4.18c). In response to La Niña, the Walker circulation across the equatorial sector of the Indo-Pacific Ocean increases in intensity. As indicated by the anomalous precipitation and surface winds (Figs. 4.4, 4.5) and the anomalous velocity potential field at 200 hPa (contours in Fig. 4.20), stronger descending motion and less rainfall occurred over the central equatorial Pacific, while stronger ascending motion and more rainfall occurred over the western equatorial Pacific and the Maritime Continent. Accordingly, an anomalous descending branch of the Walker circulation occurred for the majority of the year over eastern equatorial Africa and the western equatorial IO. After the dissipation of the positive IOB mode in early 2022, anomalous westerly winds over the equatorial IO began to increase in April–May 2022.

Owing to the positive feedback between the westerly wind anomalies and the dipole of SST anomalies over the equatorial sector of the IO, the negative IOD event quickly grew from its onset stage (i.e., April–May) to boreal summer 2022, as shown in Figs. 4.18b and 4.20b,c. Along with the increase of SST anomalies, some damping processes (e.g., negative cloud–radiation–SST feedback) may have played a role, leading to a relatively slow development of the negative IOD from boreal summer to boreal autumn. As would be expected given the negative IOD, the eastern part of the basin was characterized by anomalous warmth and increased precipitation, while the western part of the basin was characterized by anomalous coolness and decreased precipitation (Figs. 4.4, 4.5, 4.20).

The tropical Pacific was broadly characterized by La Niña for most of 2020–22 (Fig. 4.18c). During boreal summer/autumn, the IOD was generally neutral in 2020 (Chen and Luo 2021), weakly negative in 2021 (Chen and Luo 2022), and strongly negative in 2022. Although the two consecutives negative IOD events in 2021 and 2022 coincided with La Niña conditions in the Pacific, they appear to have had significantly different formation mechanisms. The weak negative IOD event in 2021 may have not only been triggered by La Niña, but may also have been influenced by other regions, such as wind and SST anomalies originating from the subtropical IO (Chen and Luo 2022). The strong negative IOD in 2022 seems to have been primarily driven by the La Niña, especially during its onset stage. This indicates the complexity of IOD formation mechanisms, which may be due to both local air–sea processes in the IO and/or remote impacts from the tropical Pacific.

In summary, a strong negative IOD event occurred in 2022, with the IOD index reaching a seasonal average of −0.9°C during boreal autumn. As noted in the previous paragraph, the development of this negative IOD event was largely driven by the La Niña. In response to La Niña, an anomalously strong

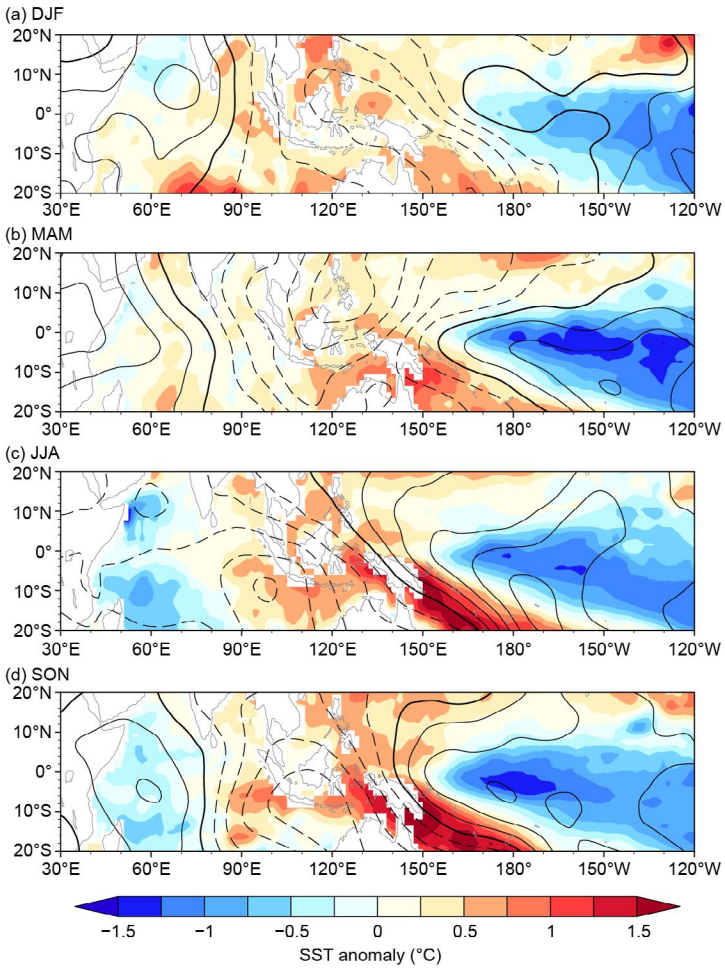

Fig. 4.20. Sea-surface temperature (SST) anomalies (°C, colored scale) and 200-hPa velocity potential (× 10^6 m^2 s^{-1}, contoured with an interval of 1; solid/dashed/bold curves denote positive/negative/zero values) during (a) Dec 2021–Feb 2022, (b) Mar–May 2022, (c) Jun–Aug 2022, and (d) Sep–Nov 2022. Anomalies were calculated relative to the climatology over the period 1982–2022. (Sources: NOAA OISST [Reynolds et al. 2002] and JRA-55 atmospheric reanalysis [Ebita et al. 2011].)

Walker circulation occurs over the tropical Indo-Pacific sector, with a stronger ascending of the Walker circulation branch over the western equatorial Pacific and the Maritime Continent and a stronger descending branching over the western equatorial IO. Consequently, anomalous westerly winds emerged in April–May 2022, and an anomalous SST dipole developed. A strong zonal dipole of SST and precipitation anomalies occurred in the equatorial IO during boreal summer and autumn, with anomalous warmth and increased precipitation in the eastern part of the basin and anomalous coolness and decreased precipitation in the western part of the basin. As is typical, the negative IOD began to decay in November–December. It is worth mentioning that such a strong negative IOD is conducive to the transition from a third-year ("triple") La Niña into El Niño in 2023, based on the potential impacts of IOD on the succeeding ENSO (Izumo et al. 2010).

g. Tropical cyclones

1. OVERVIEW

—H. J. Diamond and C. J. Schreck

The International Best Track Archive for Climate Stewardship (IBTrACS) dataset comprises historical tropical cyclone (TC) best-track data from numerous sources around the globe, including all of the World Meteorological Organization (WMO) Regional Specialized Meteorological Centers (RSMCs; Knapp et al. 2010). This dataset represents the most complete compilation of global TC data. From these data, 1991–2020 climatological values of TC activity for each basin using statistics from both the WMO RSMCs and the Joint Typhoon Warning Center (JTWC) are calculated following Schreck et al. (2014). These values are referenced in each subsection. Tallying the global TC numbers is challenging and involves more than simply adding up basin totals, as some storms cross TC basin boundaries, some TC basins overlap, and multiple agencies track and categorize TCs. The Northern Hemisphere (NH) basins are typically measured from January to December while Southern Hemisphere (SH) basins are typically measured from July to June. Global values here are the sum of NH for 2022 and SH for 2021/22.

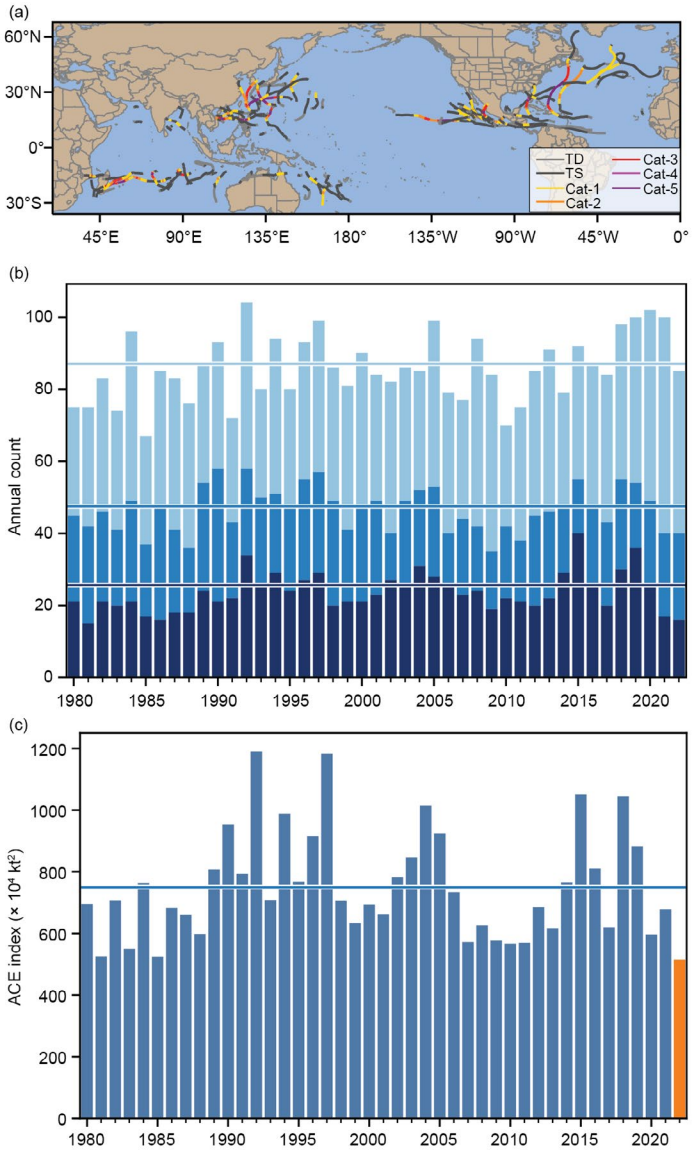

Fig. 4.21. (a) Global summary of tropical cyclone (TC) tracks; (b) global TC counts; and (c) global accumulated cyclone energy (ACE) values (× 10^4 kt^2). Horizontal lines on (b) and (c) are the 1991–2020 normals.

Based on preliminary data from NOAA's National Hurricane Center (NHC) and the JTWC as archived in IBTrACS (Fig. 4.21), the combined 2022 season had 85 named storms (sustained wind speeds ≥34 kt or 17 m s^{-1}), which is 12 fewer than the previous season (2021; Diamond and Schreck 2022) but on par with the 1991–2020 average of 87. There were 40 hurricanes/typhoons/cyclones (HTCs; sustained wind speeds ≥64 kt or 33 m s^{-1}), with only 16 of those reaching major HTC status (sustained wind speeds ≥96 kt or 49 m s^{-1}), which equals 1986 for the fewest since 1982. The accumulated cyclone energy (ACE) for the season was 517 × 10^4 kt^2, which is 22% lower than last year (Diamond and Schreck 2022) and the lowest on record since reliable global data began in 1981.

In sections 4g2–4g8, 2021/22 (SH) and 2022 (NH) seasonal TC activity are described and compared to the historical record for each of the seven WMO-defined TC basins. For simplicity, all counts are broken down by the U.S. Saffir-Simpson Hurricane Wind Scale (SSHWS)[2]. The overall picture of global TCs during 2022 is shown in Fig. 4.21, and counts by category and intensity are documented in Table 4.2.

The eastern North Pacific, North Indian Ocean, and Australian basins each had an above-normal number of named storms. The eastern North Pacific was the only basin that had more HTCs than normal. However, all five HTCs in the South Indian Ocean reached major HTC strength, which was also more than normal. In terms of ACE, the Atlantic, eastern North Pacific, and South Indian Ocean basins were all near-normal while all other basins were below normal.

The western North Pacific was quieter than normal by most metrics for the third year in a row. However, the western North Pacific produced two of the three SSHWS Category 5 storms globally in 2022. This is five fewer than last year's global count (Diamond and Schreck 2022) and below the 1991–2020 mean of 5.3. It was the fewest since 2008, when only one storm (Jangmi) reached SSHWS Category 5 status.

While not reaching Category 5 status, Major Hurricanes Fiona and Ian in the Atlantic caused tremendous damage and loss of life. Sidebar 4.1 and the following section, 4g2, describe their meteorological history and their impacts. Both parts of the chapter highlight the considerable damage that Fiona caused in the Atlantic Provinces of Canada and that Ian caused in Florida. Fiona also caused massive flooding damage in Puerto Rico, while Ian caused significant wind and storm surge damage in Cuba as well.

Table 4.2. Global counts of TC activity by basin for 2022. "+" denotes top tercile; "++" is top 10%; "–" is bottom tercile; "––" is bottom 10% (all relative to 1991–2020). "+++" denotes record values for the entire IBTrACS period of record. (Note that some inconsistencies between Table 4.2 and the text of the various basin write-ups in section g exist and are unavoidable, as tallying global TC numbers is challenging and involves more than simply adding up basin totals, because some storms cross TC basin boundaries, some TC basins overlap, and multiple agencies are involved in tracking and categorizing TCs.)

Region	TCs	HTCs	Major HTCs	SS Cat 5	ACE
North Atlantic	14	8	2	1	95
Eastern Pacific	19 +	10 +	4	0	117
Western Pacific	22 –	12 –	5 –	2	161 –
North Indian	7 +	1	0	0	11 –
South Indian	9 –	5	5 +	0	89
Australia	12 +	4	1 –	0	27 ––
Southwest Pacific	6	2	0	0	19 –
Global	85	40 –	16 ––	3 ––	517 ––

[2] SSHWS is based on 1-minute averaged winds, and the categories are defined at: https://www.weather.gov/mfl/saffirsimpson; the Australian category scale is based on 10-minute averaged winds, and those categories are defined at https://australiasevereweather.com/cyclones/tropical_cyclone_intensity_scale.htm

2. ATLANTIC BASIN

—M. Rosencrans, E. S. Blake, C. W. Landsea, H. Wang, S. B. Goldenberg, R. J. Pasch, and D. S. Harnos

(i) 2022 seasonal activity

The 2022 Atlantic hurricane season produced 14 named storms, of which 8 became hurricanes and 2 of those became major hurricanes (Fig. 4.22a). These are all near the 1991–2020 seasonal averages of 14.4 named storms, 7.2 hurricanes, and 3.2 major hurricanes based on the Hurricane Database (HURDAT2) historical archive (Landsea and Franklin 2013). HURDAT2 is also included in IBTrACS (Knapp et al. 2010). The 14 named storms were the least observed since 2015 when only 11 named storms developed. The 2022 hurricane season was classified by NOAA as a near-normal season, ending the consecutive streak of six above-normal seasons (2016–21).

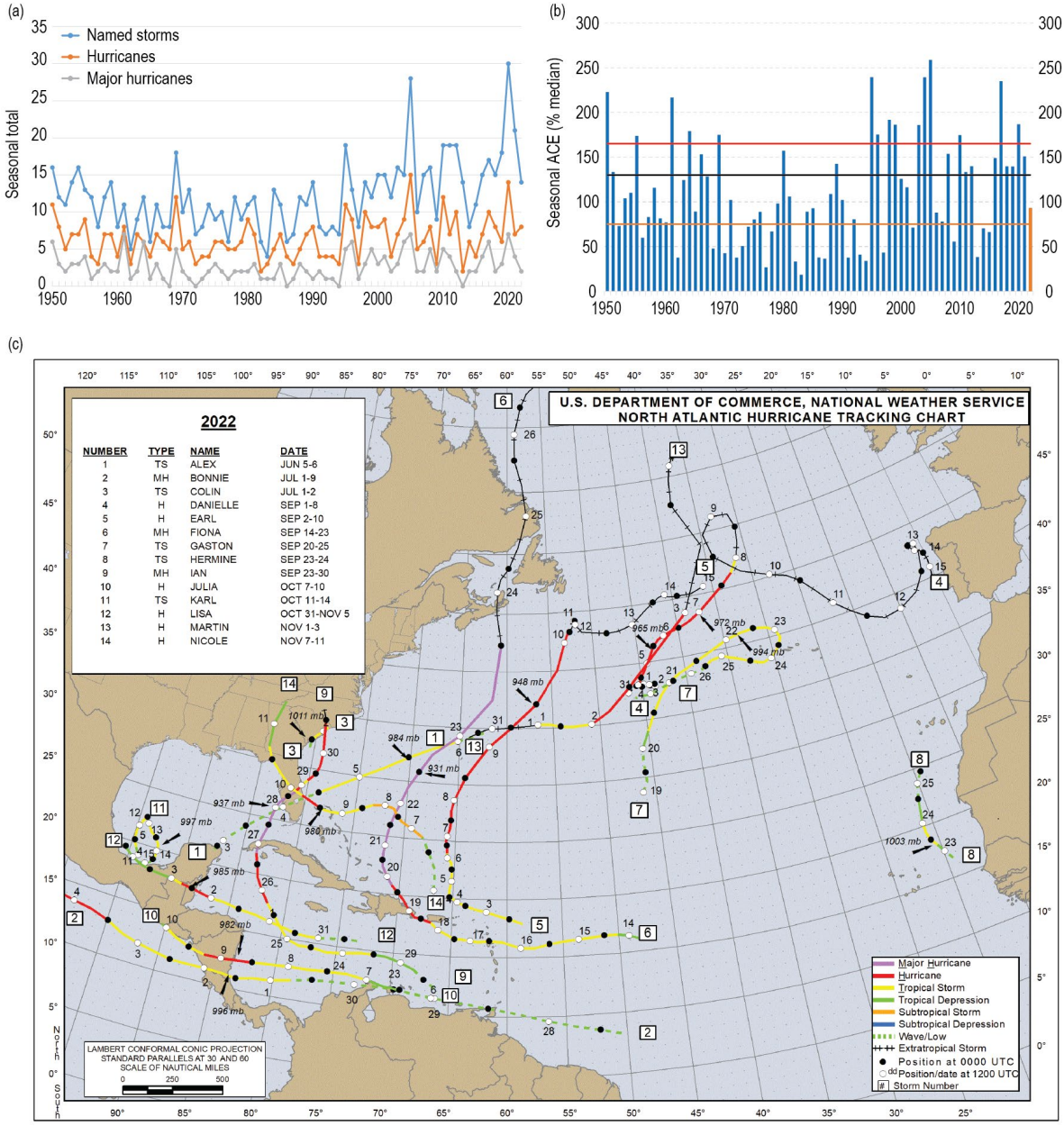

Fig. 4.22. (a) Seasonal Atlantic hurricane activity during 1950–2022 for named storms (blue), hurricanes (orange), and major hurricanes (gray). (b) The annual accumulated cyclone energy (ACE) index for 1950–2022 expressed as percent of the 1951–2020 median value. ACE is calculated by summing the squares of the six-hourly maximum sustained surface wind speed (kt) for all periods while the storm is at least tropical-storm strength. Black and orange lines correspond to NOAA's classifications for above-normal and below-normal seasons, respectively (https://www.cpc.ncep.noaa.gov/products/outlooks/Background.html). The thick red horizontal line at 165% denotes the threshold for an extremely active season. Note that there is a low-bias in activity during the 1950s through early 1970s due to the lack of satellite imagery and technique (Dvorak) to interpret tropical-cyclone intensity for systems over the open ocean. (c) 2022 Atlantic basin storm tracks. (Source: HURDAT2 [Landsea and Franklin 2013].)

Even during near-normal seasons, a single hurricane can bring devastation to an area. In 2022, Hurricane Fiona brought devastating flooding to Puerto Rico. It later set a new record for minimum sea-level pressure over land in Canada and contributed the most ACE, ~27% of the annual total, of any individual storm. Fiona was the third-costliest storm to impact Puerto Rico and the costliest weather disaster in the Canadian Maritime Provinces' history. Hurricane Ian was a major hurricane for only two days but brought extensive damage to Cuba, Florida, and portions of the southeastern United States. It caused over 100 deaths and more than $100 billion (U.S. dollars) in damage, making it the third-costliest U.S. hurricane on record. Please see Sidebar 4.1 for more discussion of Hurricanes Fiona and Ian.

Four of the 14 named storms during 2022 were short-lived (≤2 days). There has been a large increase (approximately five per year) in these "shorties" since 2000 (Landsea et al. 2010). These increased counts primarily reflect new observational capabilities such as scatterometers, Advanced Microwave Sounding Units, and the Advanced Dvorak Technique, and have no association with any known natural or anthropogenic climate variability (Villarini et al. 2011).

The 2022 seasonal ACE value was 97.8% of the 1951–2020 median (which is 96.7×10^4 kt^2; Fig. 4.22b). This value is close to the median, falling in the near-normal category (between 73 and 126×10^4 kt^2). Since the current Atlantic high-activity era began in 1995 (Goldenberg et al. 2001; Bell et al. 2019, 2020), there have been 19 above-normal seasons, with 10 of these being hyper-active. By comparison, the preceding 24-year low-activity era of 1971–94 had only two above-normal seasons, with none being extremely active.

(ii) Storm formation times, regions, and landfalls

Distinct active and inactive periods of TC activity occurred throughout the 2022 hurricane season. For the first time since 2014, no tropical storms formed before the official start of the hurricane season on 1 June. Activity in 2022 started with Tropical Storm Alex developing on 5 June. The first few days of July featured two tropical cyclones (Tropical Storms Bonnie and Colin). For the first time since 1997 and only the third time since 1950, there were no tropical storms during August. However, activity ramped up after that with six named storms developing during September, of which four became hurricanes. During the second half of September, two of the hurricanes (Fiona and Ian) attained major hurricane status and were the most destructive storms of the season. This was slightly above normal for September, which typically sees five named storms and three hurricanes. One depression, one tropical storm, and one hurricane formed during October, including the only named storm (Karl) to develop during the season in the Gulf of Mexico (The average year sees 2.2 named storms developing in the Gulf of Mexico). Three hurricanes developed in November, the last official month of the hurricane season. This ties with 2001 for the most observed on record. Historically, a hurricane only forms about every two years during November. Two of these November hurricanes made landfall, including Hurricane Nicole, which was the first November hurricane to make landfall in Florida since Kate in 1985. The majority of hurricane activity typically takes place during August–October, the climatological peak three months of the hurricane season, however, during 2022, the most active months were September–November.

Of the 14 named storms that developed in 2022, half of them formed in the Main Development Region (MDR; Fig. 4.23a, green box). The MDR spans the tropical Atlantic Ocean and Caribbean Sea between 9.5°N and 21.5°N (Goldenberg and Shapiro 1996; Goldenberg et al. 2001). That percentage of MDR formations (50%) is more typical of seasons with above-normal activity (average 52%) rather than near-normal seasons, which typically have about 38% of formations in the MDR. The MDR-related ACE value was 66% of its median and far exceeds the ACE associated with storms first named over the Gulf of Mexico (2% of the 2022 total) or in the extratropics (28%).

The storm tracks during 2022 (Fig. 4.22c) had two distinct clusters of tracks: one over the Caribbean and another over the western North Atlantic. Three storms formed at low latitudes,

with two crossing northern South America during their developing stages. Tropical Storm Bonnie moved across Central America intact, the first named storm to do so since Tropical Storm Otto in 2016, and intensified into a major hurricane over the eastern North Pacific. Hurricane Julia also crossed over from the Atlantic to the eastern North Pacific while maintaining at least tropical storm-force winds. No prior year on record has observed two systems that crossed over Central America while maintaining at least tropical-storm intensity.

(iii) Sea-surface temperatures

Sea-surface temperature (SST) anomalies ranged from just below 0°C to +0.5°C, and the area-averaged SST anomaly was +0.20°C (Figs. 4.23a,b). The area-averaged SST anomaly in the MDR was higher (by 0.28°C) than that of the global tropics (Fig. 4.23c). This signal typifies the warm phase of the Atlantic Multi-decadal Oscillation (AMO; Enfield and Mestas-Nuñez 1999; Bell and Chelliah 2006) and is a ubiquitous characteristic of Atlantic high-activity eras such as 1950–70 and 1995–present (Goldenberg et al. 2001; Vecchi and Soden 2007; Bell et al. 2018).

During August–October (ASO) 2022, above-average temperatures were also present across most of the North Atlantic Ocean. Outside of the MDR, the largest anomalies (exceeding +1.5°C) occupied portions of the central North Atlantic (Fig. 4.23a), areas where numerous tropical storms and hurricanes tracked. Extended Reconstructed Sea Surface Temperature version 5 (ERSST)-based anomalies over the entire North Atlantic for ASO were +0.47°C, consistent with a positive AMO. The continuing La Niña event typically reduces wind shear and increases mid-level moisture across the tropical Atlantic Ocean, both of which enhance tropical cyclone development.

(iv) Atmospheric conditions

Climatologically, the ASO peak in Atlantic hurricane activity largely reflects the June–September peak in the West African monsoon. The inter-related circulation features of an enhanced monsoon act to further increase hurricane activity, while those of an anomalously weak monsoon act to suppress it (Gray 1990; Hastenrath 1990; Landsea et al. 1992; Bell and Chelliah 2006; Bell et al. 2018, 2020). The association on multi-decadal time scales between the AMO and Atlantic hurricane activity largely exists because of their common relationship to the West African monsoon (Bell and Chelliah 2006) and reduced vertical shear due to weaker easterly trade winds in the MDR (Goldenberg et al. 2001). The West African

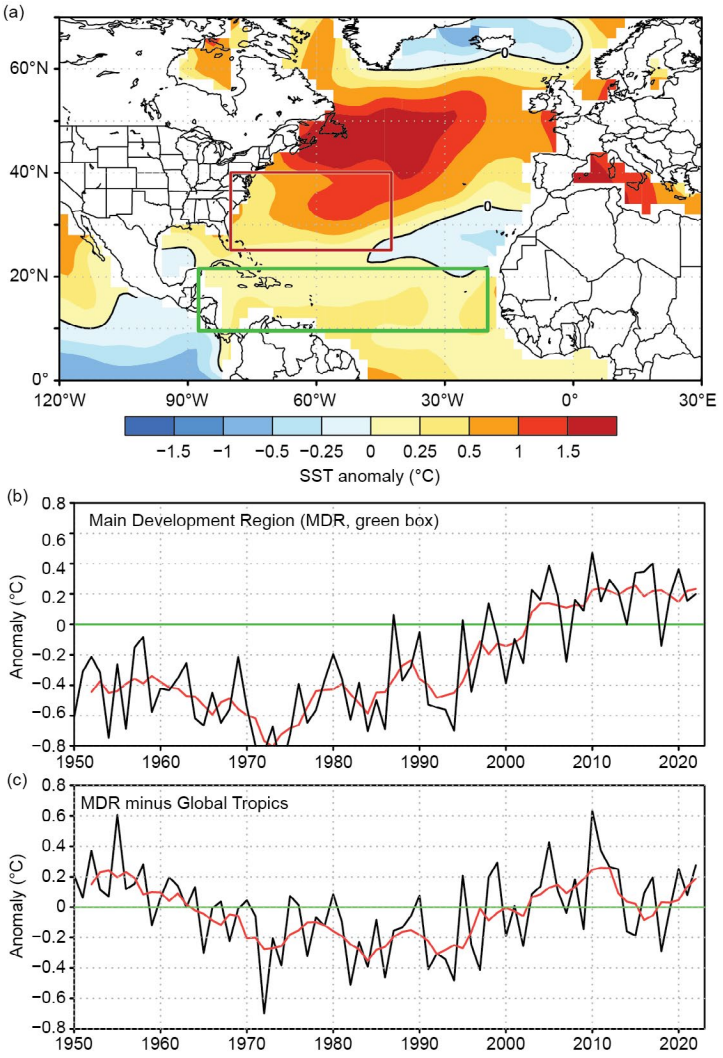

Fig. 4.23. (a) Aug–Oct 2022 sea-surface temperature (SST) anomalies (°C). (b),(c) Time series of Aug–Oct area-averaged SST anomalies (black) and 5-pt running mean of the time series (red): (b) In the Main Development Region (MDR, green box in (a) spanning 20°W–87.5°W and 9.5°N–21.5°N), and (c) difference between the MDR and the global tropics (20°S–20°N). Anomalies are departures from the 1991–2020 period means. The green horizontal line in (b) and (c) highlights the zero value, a critical reference value. (Source: ERSST-v5 [Huang et al. 2017].)

monsoon was enhanced during July–September (JAS) 2022, as indicated by negative outgoing longwave radiation (OLR) anomalies across the African Sahel (Fig. 4.24a, red box). Total OLR values in this region averaged 235 W m^{-2} (Fig. 4.24b), with values less than 240 W m^{-2} indicating deep tropical convection. The OLR time series shows that an enhanced monsoon has largely prevailed throughout the current Atlantic high-activity era and warm AMO of 1995–present (Fig. 4.24b). In contrast, a much weaker monsoon with OLR values well above 240 W m^{-2} in the Sahel region was typical of the low-activity era during the cool AMO period of the 1980s and early 1990s.

Consistent with a slightly above-normal monsoon, the large-scale divergent circulation at 200 hPa featured an extensive area of anomalous divergence over western Africa (Fig. 4.24c). The signal was not as robust as measured in 2021, with the core of negative velocity potential

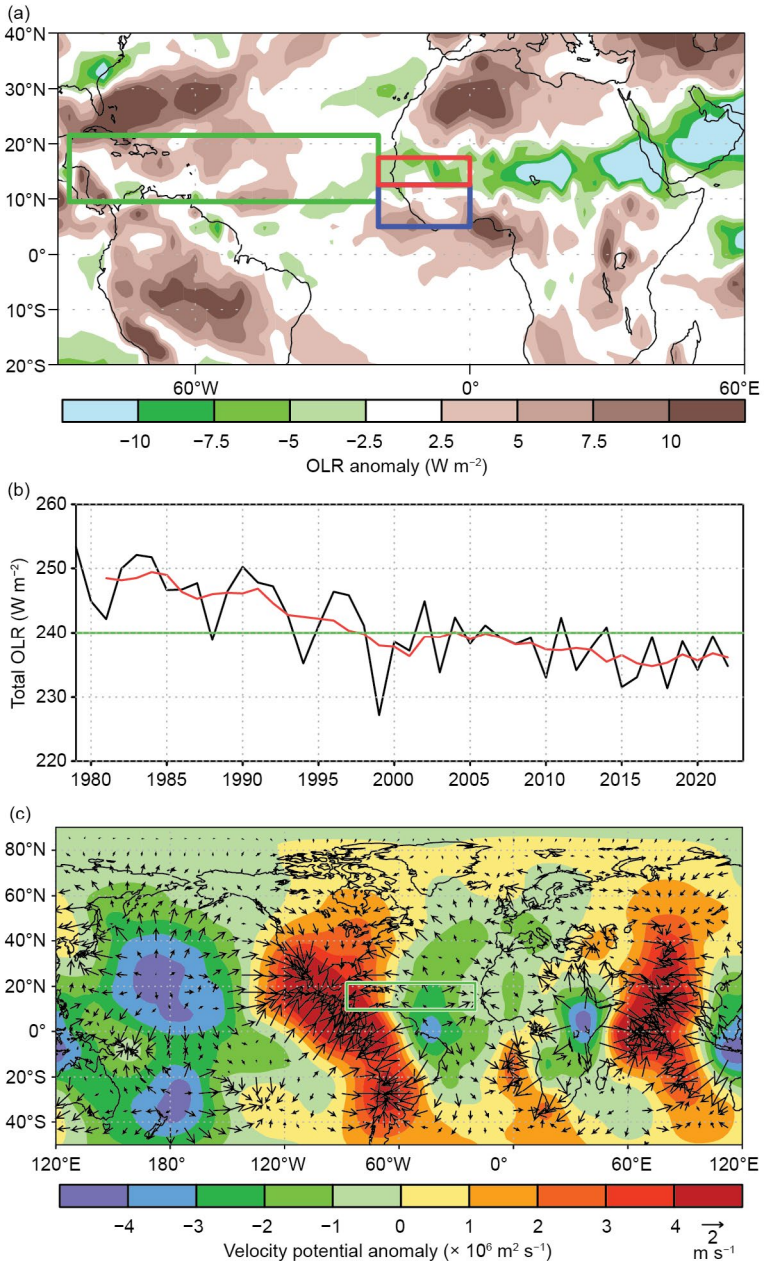

Fig. 4.24. (a) Jul–Sep 2022 anomalous outgoing longwave radiation (OLR; W m^{-2}), with negative (positive) values indicating enhanced (suppressed) convection. (b) Time series of Jul–Sep total OLR (black) and 5-yr running mean of the time series (red) averaged over the African Sahel region (red box in (a) spanning 20°W–0° and 12.5°N–17.5°N). (c) Jul–Sep 2022 anomalous 200-hPa velocity potential (× 10^6 m^2 s^{-1}) and divergent wind vectors (m s^{-1}). In (a), (c), the green box denotes the Atlantic Main Development Region. Anomalies are departures from the 1991–2020 means. The green horizontal line in (b) highlights the 240 value, a critical reference value for relating OLR to convection. (Sources: Liebmann and Smith [1996] for OLR; NCEP/NCAR Reanalysis [Kalnay et al. 1996].)

anomalies split by an area of near-zero anomalies and anomalous convergence. Analysis of streamfunction at 200 hPa (Fig. 4.25a) shows anomalous anticyclones over the Caribbean and over the eastern Atlantic, with cyclonic anomalies over portions of the MDR and western Africa. Farther north, a large anticyclonic anomaly is evident over central Canada with a cyclonic anomaly over the western Atlantic. This ASO 2022 streamfunction pattern over the eastern MDR does not resemble those associated with La Niña and the positive phase of the multi-decadal mode that is associated with higher activity (Bell and Chelliah 2006). Over the eastern MDR, ASO 2022 featured a large cyclonic anomaly. The ASO 2022 200-hPa streamfunction pattern more closely resembles the 200-hPa streamfunction anomaly pattern that Bell and Chelliah (2006)

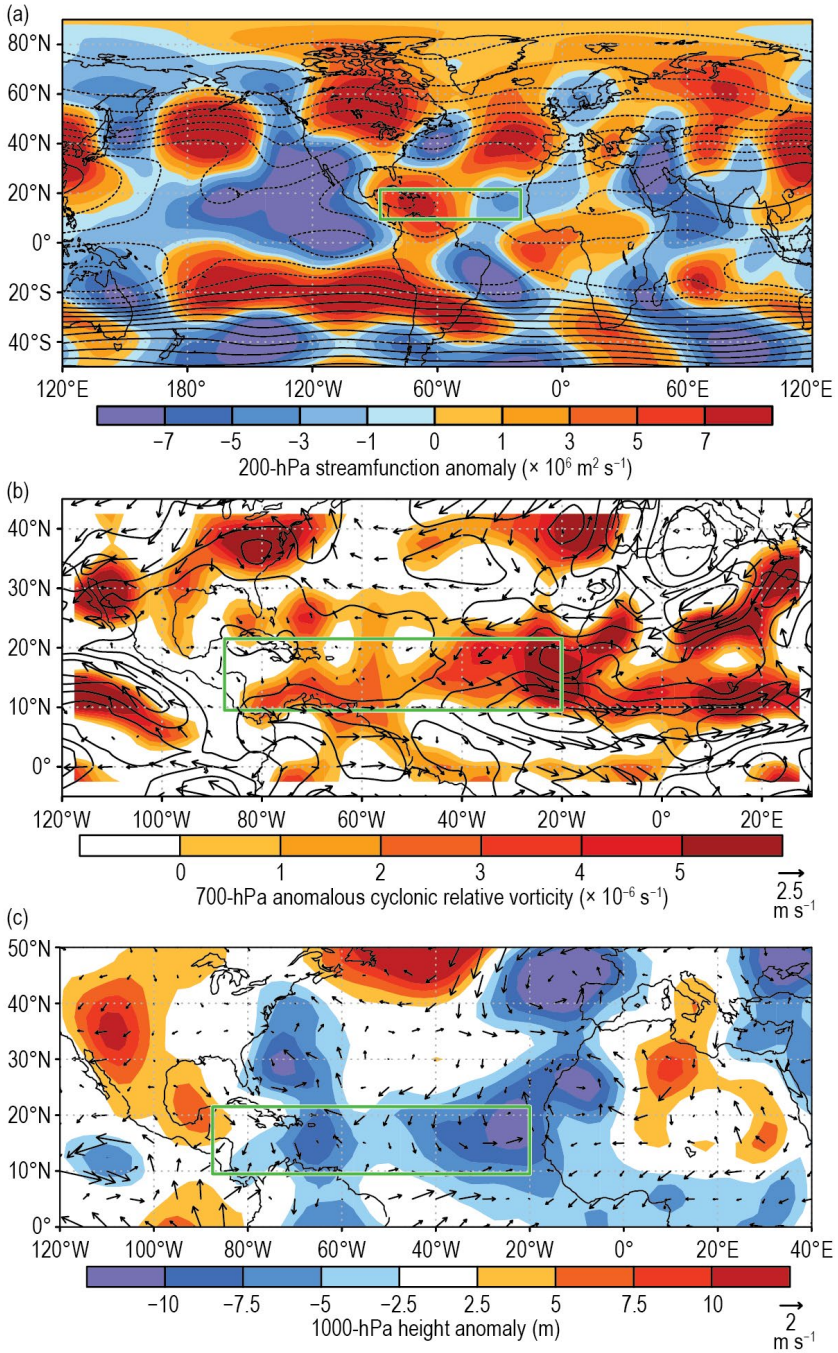

Fig. 4.25. Aug–Oct 2022: (a) 200-hPa streamfunction (contours, interval is 5 × 10^6 m^2 s^{-1}) and anomalies (shaded); (b) anomalous 700-hPa cyclonic relative vorticity (shaded, × 10^{-6} s^{-1}), wind speed (contours), and vector winds (m s^{-1}); (c) anomalous 1000-hPa heights (shaded, m) and vector winds. Vector scales differ for each panel and are below right of the color bar. Green box denotes the Main Development Region. Anomalies are departures from the 1991–2020 means. (Source: NCEP/NCAR reanalysis [Kalnay et al. 1996].)

found for La Niña episodes during 1975–1994 during a low-activity era rather than those during active eras. This discrepancy points to activity being mitigated by factors other than La Niña.

The 700-hPa anomalous wind and vorticity fields (Fig. 4.25b) indicate enhanced vorticity across the MDR. The 1000-hPa anomalous height and wind field (Fig. 4.25c) shows that the near-surface winds were largely aligned with the 700-hPa wind fields, with below-average heights and cyclonic turning of the winds across much of the MDR.

The ASO 2022 200-hPa–850-hPa wind shear was slightly above average for much of the MDR, with the highest positive anomalies located in the western MDR/Caribbean (Fig. 4.26a). The area-averaged magnitude of the vertical wind shear for the entire MDR was 9.1 m s^{-1} (Fig. 4.26b) and 11.2 m s^{-1} for the Gulf of Mexico (Fig. 4.26c). Shear values less than 10 m s^{-1} are generally considered conducive to hurricane formation (Gray 1968; DeMaria et al. 2005; Tippett et al. 2011). The lack of tropical storm activity over the Gulf of Mexico is likely related to the high shear, the highest value for that region since 2011.

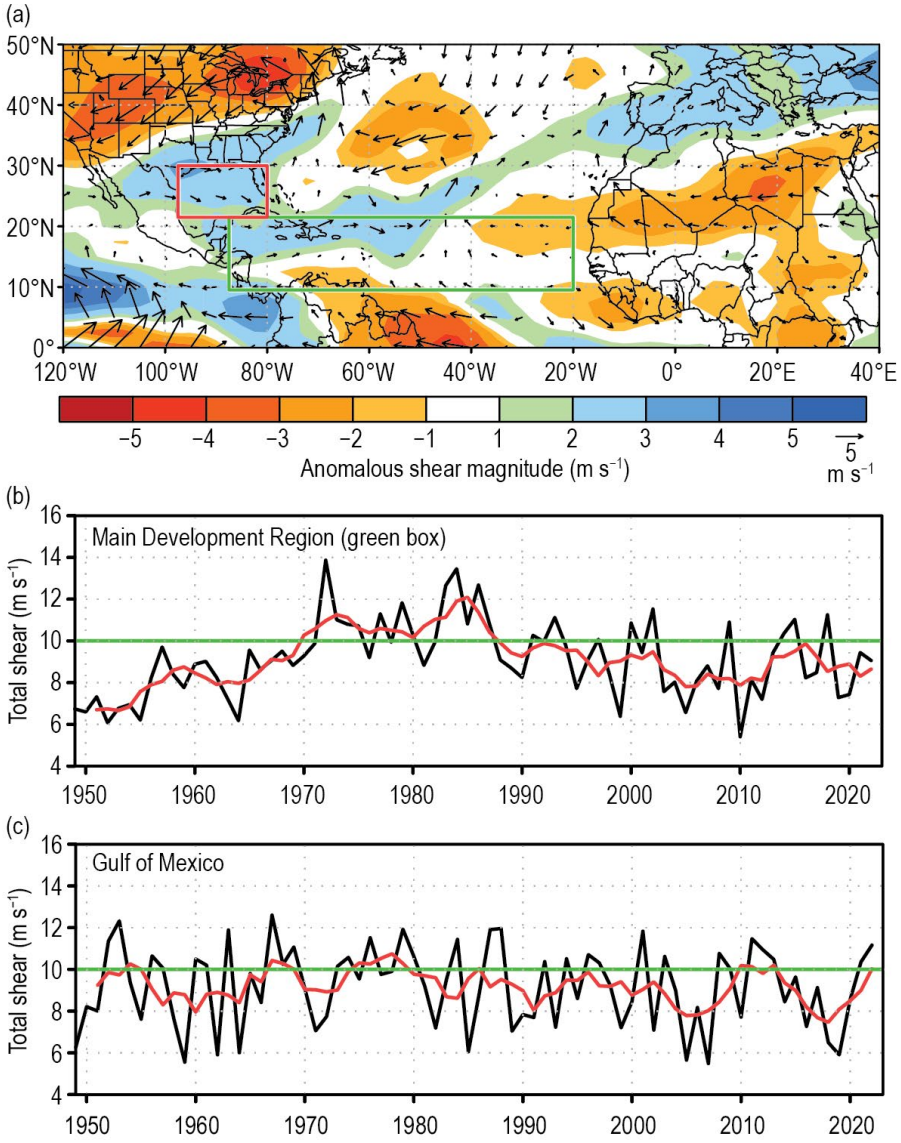

Fig. 4.26. Aug–Oct magnitude of the 200-hPa–850-hPa vertical wind shear (m s^{-1}): (a) 2022 anomalous magnitude and vector. (b), (c) Time series of Aug–Oct vertical shear magnitude (black) and 5-yr running mean of the time series (red) averaged over (b) the Main Development Region (green box in (a), spanning 87.5W°–20°W and 9.5°N–21.5°N) and (c) the Gulf of Mexico (21.5°N–30°N and 97.5°W–80°W). The green horizontal lines in (b) and (c) highlight the value 10, a critical reference value where shear is thought to inhibit tropical cyclone development on monthly and seasonal time scales. Anomalies are departures from the 1991–2020 means. (Source: NCEP/NCAR reanalysis [Kalnay et al. 1996].)

Further analysis shows that the largest anomalous 200-hPa–850-hPa wind-shear values were over the Caribbean, with anomaly values in excess of 5.0 m s^{-1} (Fig. 4.27a). The 200-hPa–850-hPa total wind shear over the MDR in August was 9.3 m s^{-1} (Fig. 4.27b), barely meeting the <10 m s^{-1} threshold conducive for tropical cyclogenesis. Additionally, specific humidity over the MDR (Fig. 4.27c) reflected anomalously dry conditions from about 30°W to 70°W. Furthermore, upper-level cyclonic flow was present over much of the MDR (Fig. 4.27d). Those factors likely

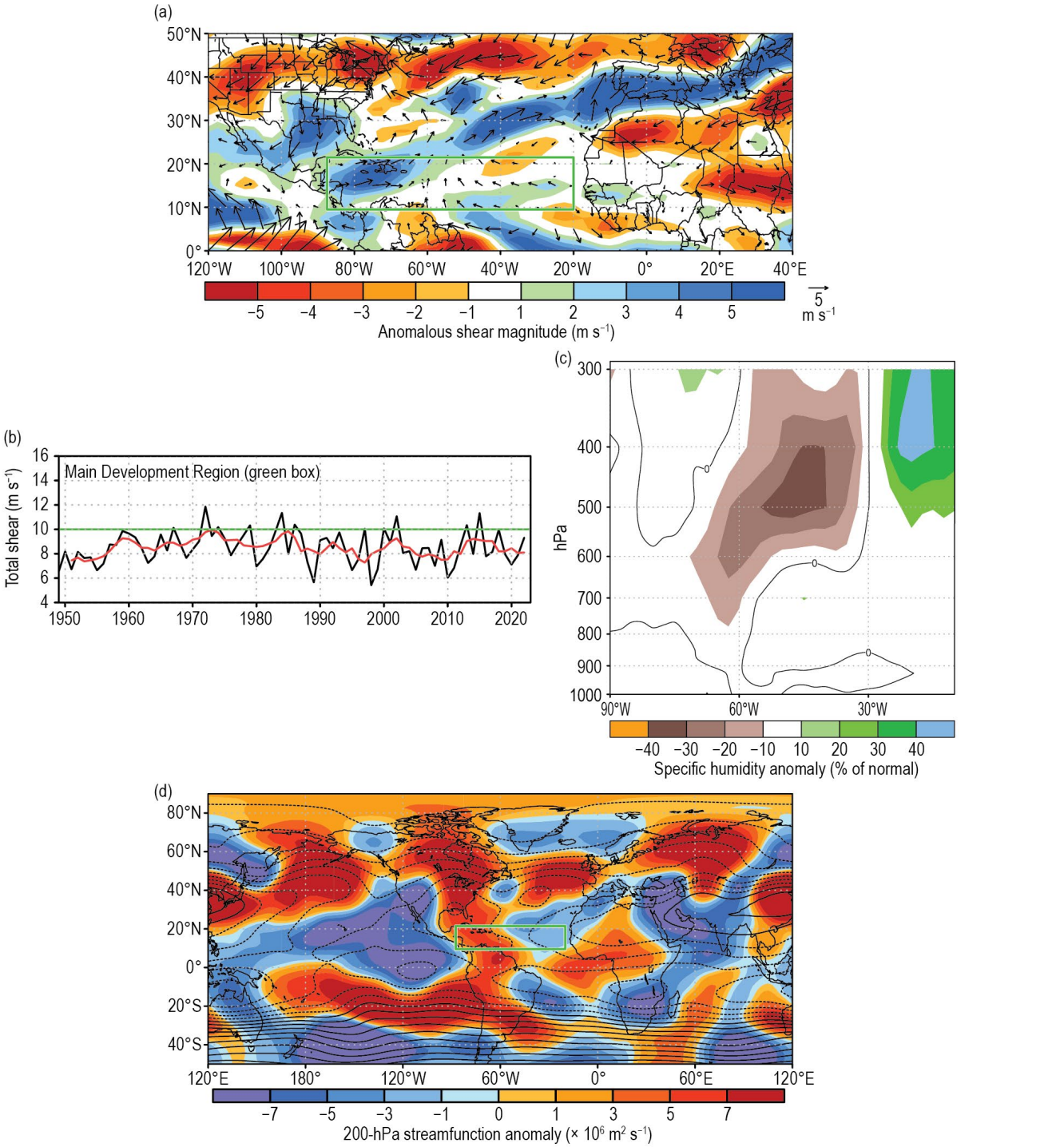

Fig. 4.27. (a) Aug 2022 magnitude of the 200-hPa–850-hPa vertical wind shear (m s^{-1}) showing anomalous magnitude and vector; (b) time series of vertical shear magnitude (black) and 5-yr running mean of the time series (red) averaged over the Main Development Region (MDR; green box in (a)), with the green horizontal line at 10, a critical reference value where shear is thought to inhibit tropical cyclone development on a monthly and seasonal time scales: (c) Aug 2022 MDR specific humidity deviations from normal (percent). Brown (green) shading represents below- (above-) normal values, with the thin black line representing no deviation; (d) Aug 2022 200-hPa streamfunction (contours, interval is 5 × 10^6 m^2 s^{-1}) and anomalies (shaded). (Source: NCEP/NCAR reanalysis [Kalnay et al. 1996].)

inhibited the development of tropical cyclones during August. In September, wind shear in the MDR dropped to 6.7 m s^{-1} (Fig. 4.28b), and specific humidity values returned closer to normal for much of the MDR (Fig. 4.28a).

The higher wind shear during August is not a typical response to La Niña conditions in the Pacific, and is also at odds with the Madden-Julian Oscillation (MJO) activity during late August. The anomalously low upper-level moisture and upper-level streamflow patterns being dissimilar from other low-activity years, where the low levels of activity were linked to tropical-based drivers, points to the likely driver of the high shear and low-upper level moisture being midlatitude influenced. An anomalously strong tropical upper tropospheric trough may correspond to relatively larger contributions from midlatitude influences on the tropical circulation (Klotzbach 2022). Therefore, additional research is required to determine if there was any predictable sub-seasonal forcing for this midlatitude influence.

As is typical during October, wind-shear values and specific humidity values increased significantly over the MDR. Near-normal shear was present near the Bay of Campeche, in the vicinity of where Tropical Storm Karl formed, and over portions of the Caribbean, near where Hurricanes Lisa and Julia developed. Hurricane Nicole developed in an area of extremely low 200-hPa–850-hPa wind shear, 4 m s^{-1} to 5 m s^{-1} below normal, a relatively moist environment, and anticyclonic flow to the north. Those factors likely aided in Nicole's development and westward turn toward the east coast of Florida. Other than the unusually quiet August, September, October, and November behaved more like a typical above-average season.

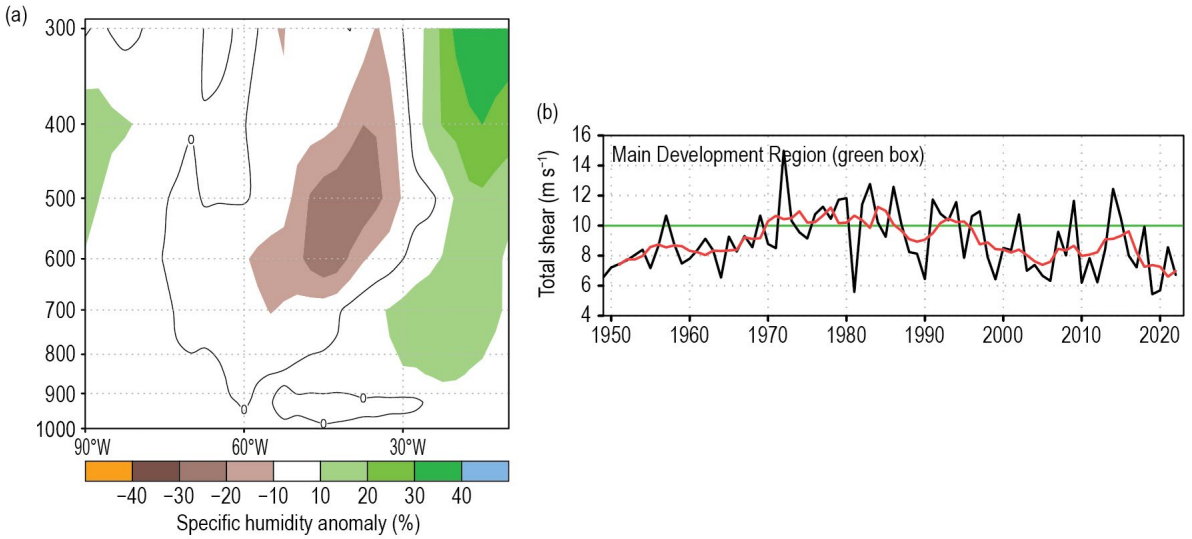

Fig 4.28. Sep 2022 conditions: (a) Main Development Region specific humidity deviations from normal (%). Brown (green) shading represents below- (above-) normal values, with the thin black line representing no deviation; (b) time series of vertical shear magnitude (black) and five-year running mean of the time series (red) averaged over the MDR (green box in Fig. 4.23a). The green horizontal line is at 10, a critical reference value where shear is thought to inhibit tropical cyclone development on a monthly and seasonal time scales.

3. EASTERN NORTH PACIFIC AND CENTRAL NORTH PACIFIC BASINS

—K. M. Wood and C. J. Schreck

(i) Seasonal activity

Numbers in this section are combined from the two agencies responsible for issuing advisories and warnings in the eastern North Pacific (ENP) basin: NOAA's National Hurricane Center in Miami, Florida (for the region from the Pacific coast of North America to 140°W), and NOAA's Central Pacific Hurricane Center in Honolulu, Hawaii (for the region between 140°W and the date line; the Central North Pacific [CNP]).

A total of 19 named storms formed within or crossed into the combined ENP/CNP basin in 2022, 10 of which became hurricanes and 4 became major hurricanes (Fig. 4.29a). This activity is above normal for named storms and hurricanes and near normal for major hurricanes compared

with the 1991–2020 averages of 16.9 named storms, 8.8 hurricanes, and 4.6 major hurricanes. All 2022 storms occurred between the official ENP hurricane season start date of 15 May and end date of 30 November. The first named storm of the season, Hurricane Agatha, developed on 28 May, and the final named storm, Hurricane Roslyn, dissipated on 24 October after making landfall in Mexico as a hurricane. Unusually, 2 of the 19 ENP named storms crossed Central America from the North Atlantic (Bonnie and Julia). No named storms formed within the CNP, but one dissipated about two and a half days after crossing 140°W (Darby), which is well below the 1991–2020 average of 3.4 named storms for the CNP.

Although TC counts were above normal, the 2022 seasonal ACE index was 116.9 × 10^4 kt^2, or 88% of the 1991–2020 mean of 132.8 × 10^4 kt^2 (Fig. 4.29b; Bell et al. 2000), continuing the streak of below-normal ACE activity that has persisted since 2019 (Fig. 4.29b; Wood and Schreck 2020, 2021, 2022). July TC activity was more than double the usual ACE for the month, contributing 45% of the season's ACE from five named storms, including two hurricanes (Estelle, Frank) and two major hurricanes (Bonnie, Darby). In contrast, August produced only 6% of the season's ACE, compared to the climatological average of 29% (Fig. 4.29c). October (16% of ACE) was slightly more active than September (15% of ACE). The four 2022 ENP TCs that reached major hurricane intensity (≥96 kt; 49 m s^{-1}) on the SSHWS contributed about 46% of the season's total ACE: Bonnie, Darby, Orlene, and Roslyn.

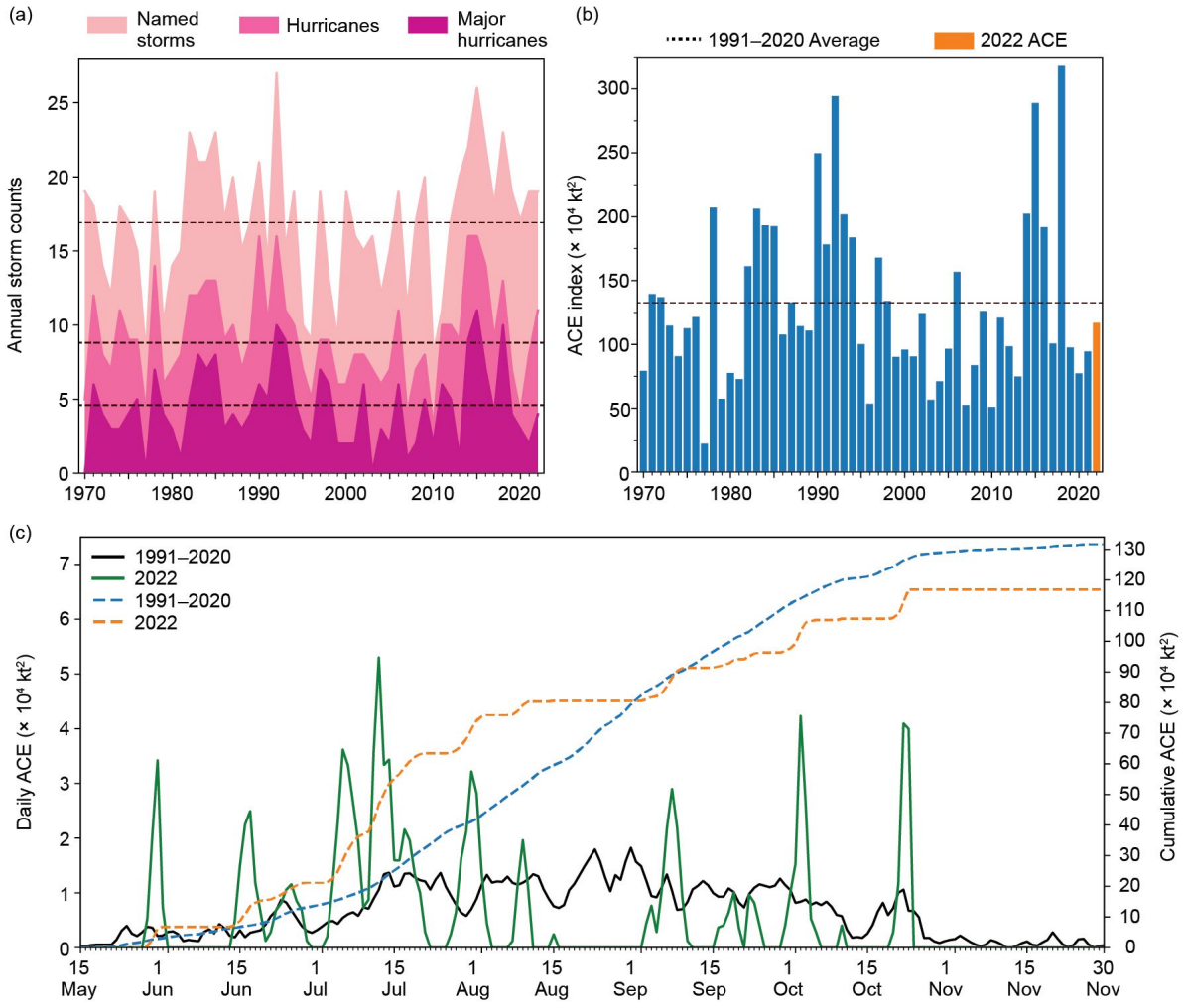

Fig. 4.29. Annual eastern North Pacific (a) storm counts by category during 1970–2022, with the 1991–2020 average by category denoted by each dashed line, and (b) accumulated cyclone energy (ACE) during 1970–2022, with 2022 highlighted in orange and the 1991–2020 average denoted by the dashed line. (c) Daily eastern North Pacific ACE for the 1991–2020 average (solid black) and during 2022 (solid green); accumulated daily ACE for the 1991–2020 average (dashed blue) and during 2022 (dashed orange).

(ii) Environmental influences on the 2022 season

Negative SST anomalies reminiscent of a typical La Niña pattern characterized the equatorial eastern Pacific during the 2022 ENP hurricane season, with co-located easterly 850-hPa wind anomalies between 180°W and 140°W (Figs. 4.30a,d). Storm formations were largely co-located with regions of seasonally near-normal OLR, near-to-above normal SSTs, and below-average vertical wind shear. Despite a broad region of below-average wind shear, TC activity was generally confined to the eastern half of the combined ENP/CNP basin, with only Darby crossing 140°W (Fig. 4.30c). As in 2021, enhanced 850-hPa westerly flow occurred near Central America, potentially supporting the observed clustering of TC activity via enhanced low-level cyclonic vorticity (Fig. 4.30d).

The development and intensity evolution of ENP TCs can be affected by the MJO as well as convectively-coupled Kelvin waves (e.g., Maloney and Hartmann 2001; Aiyyer and Molinari 2008; Schreck and Molinari 2011; Ventrice et al. 2012a,b; Schreck 2015, 2016). A relatively robust MJO signal coincident with a passing Kelvin wave may have contributed favorable conditions for Agatha's development in late May. In addition, the MJO may have supported Lester in

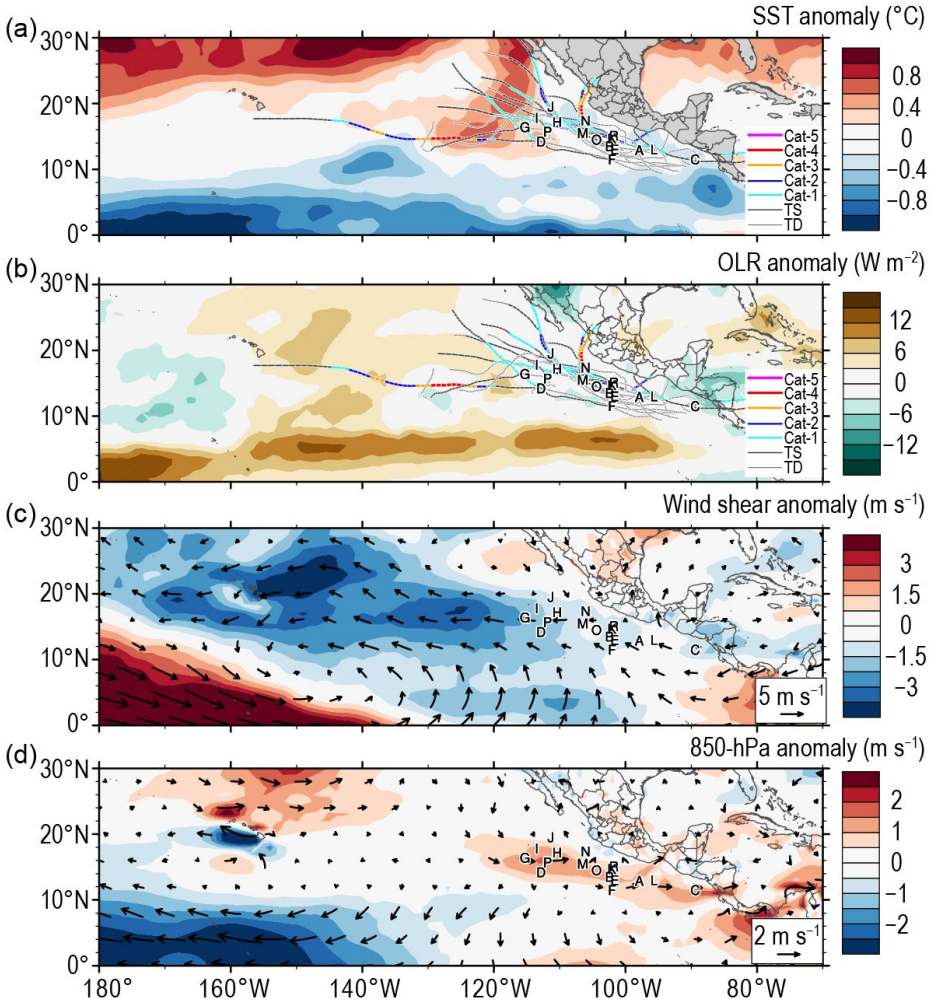

Fig. 4.30. 15 May–30 Nov 2022 anomaly maps of (a) sea-surface temperature (SST; °C; Banzon and Reynolds 2013), (b) outgoing longwave radiation (OLR; W m^{-2}; Schreck et al. 2018), (c) 200-hPa–850-hPa vertical wind shear (m s^{-1}) vector (arrows) and scalar (shading) anomalies, and (d) 850-hPa wind (m s^{-1}, arrows) and zonal wind (shading) anomalies. Anomalies are relative to the annual cycle from 1991 to 2020. Letters denote where each tropical cyclone attained tropical-storm intensity. Wind data are obtained from CFSR (Saha et al. 2014).

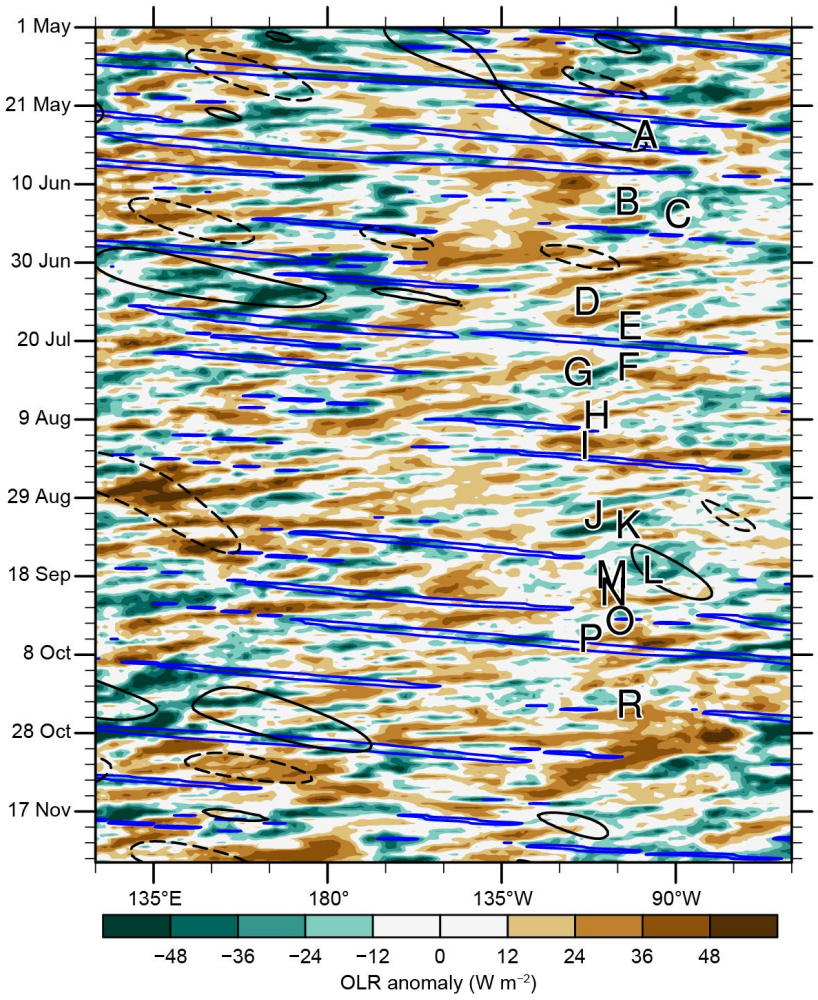

September, but otherwise MJO influences appeared relatively weak throughout the season (Fig. 4.31). Kelvin waves traversed the basin on a fairly regular basis, and cyclogenesis is generally favored within three days after a Kelvin wave passage. However, this pattern was not commonly observed in 2022. The formations of Agatha, Frank, and Paine were the most likely to have been influenced by Kelvin waves. Finally, easterly wave activity—which can be inferred from Fig. 4.31 as westward-moving negative (green) OLR anomalies—likely supported many ENP genesis events.

Fig. 4.31. Longitude–time Hovmöller diagram of 5°N–15°N average outgoing longwave radiation (OLR; W m^{-2}; Schreck et al. 2018). Unfiltered anomalies from a daily climatology are shaded. Negative anomalies (green) indicate enhanced convection. Anomalies filtered for Kelvin waves are contoured in blue at –10 W m^{-2} and Madden-Julian Oscillation (MJO)-filtered anomalies in black at ±10 W m^{-2} (dashed for positive, solid for negative). Letters are centered on the longitude and time when each tropical cyclone attained tropical-storm intensity.

(iii) Notable ENP TCs and impacts in 2022

Hurricane Bonnie, which was first named in the North Atlantic, fell short of the canonical rapid intensification threshold of ≥30 kt (15.4 m s^{-1}) in 24 hours as it approached its peak intensity of 100 kt but later rapidly weakened while over open ocean (≤–30 kt or –15.4 m s^{-1} in 24 hours; Wood and Ritchie 2015). Hurricane Darby rapidly intensified with a peak 24-hour intensity increase of 60 kt (31 m s^{-1}) prior to reaching its maximum intensity of 120 kt (62 m s^{-1}) and then underwent two periods of over-ocean rapid weakening. Hurricane Orlene reached a peak 24-hour intensity increase of 55 kt (28 m s^{-1}) before becoming a 115-kt major hurricane; the TC began weakening prior to landfall in southwestern Mexico with an estimated 75-kt intensity. Hurricane Roslyn followed a similar track to Orlene and also reached a peak 24-hour intensity increase of 55 kt (28 m s^{-1}) before becoming a 115-kt major hurricane. Compared to Orlene, however, Roslyn maintained more of its strength prior to its estimated 105-kt landfall in the same part of west-central Mexico as Orlene three weeks earlier. Bonnie, Darby, and Roslyn maintained peak intensity for only 12 hours and Orlene just 6 hours. In addition, Orlene and Roslyn were relatively short-lived TCs, factors that contributed to the four strongest TCs contributing less than half of the season's ACE, in contrast to recent seasons (e.g., 2021; Wood and Schreck 2022).

Four ENP TCs in 2022 made landfall along Mexico's west coast: Kay as a tropical storm, Agatha and Orlene as hurricanes, and Roslyn as a major hurricane. A fifth TC, Lester, impacted Mexico but as a tropical depression (Reinhart 2022). In addition, Julia hit Nicaragua from the North Atlantic as a hurricane, crossed Central America, and then made another landfall in El Salvador from the ENP as a tropical storm. Bonnie made landfall near the Nicaragua–Costa Rica border from the North Atlantic as a tropical storm, crossed Central America, and then grew to major hurricane status in the ENP but did not make any additional landfalls. Landfalling ENP TC

activity was higher than normal for Mexico, possibly as a consequence of many TCs forming near land in 2022. On average, 1.8 TCs make landfall per year (Raga et al. 2013).

Hurricane Agatha caused nine deaths attributed to mudslides and freshwater flooding in Mexico, plus six missing people and at least $50 million (U.S. dollars) in economic losses (Beven 2022; Aon 2023). Hurricane Kay followed an unusual track (see Fig. SB4.3a), maintaining a warm core at relatively high latitudes for the ENP while moving parallel to and eventually making landfall in Baja California, where it delivered heavy rain and strong winds to portions of northwest Mexico and the southwestern United States. The rain and wind associated with Kay resulted in power outages in California as well as relief to fire danger conditions. Tropical Storm Lester caused one death due to large waves, as rainfall from the storm flooded over 400 homes, caused multiple injuries, and required water rescues (Reinhart 2022). Hurricane Orlene rapidly weakened from its peak intensity of 115 kt prior to a 75-kt landfall in western Mexico, causing power outages and some wind damage. Hurricane Roslyn was the strongest landfalling ENP TC since Patricia in 2015 when it made landfall as a Category 3 (105-kt) hurricane. Roslyn resulted in an estimated four deaths and widespread power outages. Hurricane Julia crossed Central America from the Atlantic and then made a second landfall from the Pacific in El Salvador. Overall, Julia caused 89 deaths and hundreds of millions of U.S. dollars in economic damage (Aon 2023; Cangialosi 2023).

4. WESTERN NORTH PACIFIC BASIN

—S. J. Camargo

(i) Overview

The 2022 tropical cyclone (TC) season in the western North Pacific was below normal by most measures of TC activity. The data used here are primarily from JTWC best-track data for 1945–2021, with preliminary operational data for 2022. All statistics are based on the 1991–2020 climatological period unless otherwise noted.

According to the JTWC, a total of 22 TCs (bottom quartile: 23) reached tropical-storm intensity in 2022. Of these, 12 reached typhoon intensity (bottom quartile: 13), with 3 reaching super typhoon status (≥130 kt; bottom quartile: 3). There were also 7 tropical depressions (upper quartile: 7). A total of 48% of the tropical storms intensified into typhoons (bottom quartile: 56%), while only 25% of the typhoons reached super typhoon intensity (median: 29%). Figure 4.32a shows the number of storms in each category for the period 1945–2022.

The Japan Meteorological Agency (JMA) total for 2022 was 25 named storms (median: 25.5). As is typically the case, there were differences between the JTWC and JMA counts[3]. Songda and Trases were considered tropical depressions by JTWC and tropical storms (TSs) by JMA. Kulap and Nalgae were considered typhoons by JTWC but only reached the severe tropical storm category per JMA. JMA included Mulan (8–11 October) as a TS, but this storm was not included by JTWC. The number of all TCs (1951–76) and TSs, severe tropical storms, and typhoons (1977–2022) according to the JMA are shown in Fig. 4.32b. The Philippine Atmospheric, Geophysical and Astronomical Services Administration (PAGASA) named 18 TCs that entered its area of responsibility, including Storms 13W and 25W, which were named Gardo and Obet locally by PAGASA, but were not named by JMA, and Tropical Depression Maymay (8–11 August), which was not numbered or named by either the JMA or JTWC.

(ii) Seasonal activity

The 2022 season started with Tropical Depression 01W at the end of March, followed by Typhoon Malakas and Tropical Storm Megi in April (top quartile: 1). No storms occurred in May. Typhoon Chaba and Tropical Storm Aere formed at the end of June (median: 1). The early season

[3] It is well known that there are systematic differences between the JMA and the JTWC and the datasets, which have been extensively documented in the literature (e.g., Knapp et al. 2013; Schreck et al. 2014).

(January to June) had a total of four named storms (median: 4). The cumulative monthly number of named storms and typhoons for 2022 are shown in Figs. 4.32c,e, respectively, with the number of typhoons and super typhoons (>130 kt) per month displayed in Figs. 4.32d,f. In Figs. 4.32c–f, the 2022 values are compared with the climatological values, as well as the historical maxima and minima.

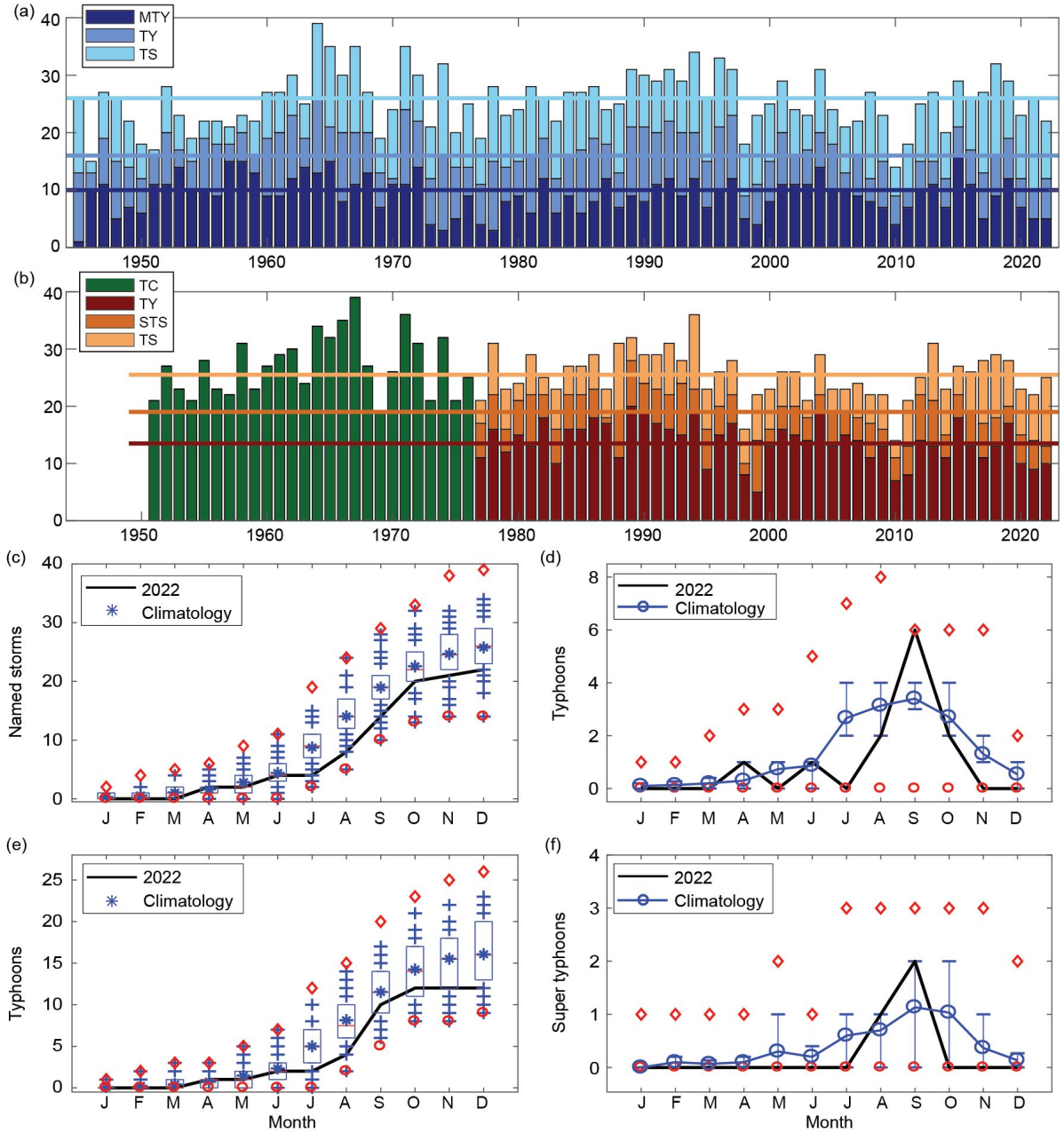

Fig. 4.32. (a) Number of tropical storms (TS), typhoons (TY), and major typhoons (MTY ≥96 kt) per year in the western North Pacific (WNP) for the period 1945–2022 based on JTWC. (b) Number of tropical cyclones (TCs; all storms which reach TS intensity or higher) from 1951 to 1976; number of TS, severe tropical storms (STS) and TY from 1977 to 2022 based on JMA. (c) Cumulative number of tropical cyclones with TS intensity or higher (named storms) per month in the WNP in 2022 (black line), and climatology (1991–2020) as box plots (interquartile range: box, median: red line, mean: blue asterisk, values in the top or bottom quartile: blue crosses, high [low] records in the 1945–2021 period: red diamonds [circles]). (e) As in (c) but for the number of typhoons. (d),(f) Number of typhoons and super typhoons (≥130 kt) per month in 2022 (black line) and the climatological mean (blue line). The red diamonds and circles denote the maximum and minimum monthly historical records, and the blue error bars show the climatological interquartile range for each month (in the case of no error bars, the upper and/or lower percentiles coincide with the median). (Sources: 1945–2021 JTWC best-track dataset; 2022 JTWC preliminary operational track data for panels (a) and (c)–(f); 1951–2022 Regional Specialized Meteorological Center-Tokyo, Japan Meteorological Agency [JMA] best-track dataset for (b).)

Chaba and Aere, both of which formed in June, were the only active storms in July. TC activity increased in August and was notable for having only four named storms (bottom quartile: 5): Tropical Storms Meari and Ma-On, Typhoon Tokage, and Super Typhoon Hinnamnor. September was the most active month of the season and the only month in 2022 with an above-average level of TC activity, with the occurrence of six typhoons (upper quartile: 4): Muifa, Merbok, Kulap, and Roke, with Nanmadol and Noru reaching super-typhoon intensity (upper quartile: 2). Seven storms formed in October, including four tropical storms, 21W, Sonca, Haitang, and Banyan, and two typhoons, Nesat and Nalgae (named storms, upper quartile: 5; typhoons, bottom quartile: 2).

Similar to the early part of the season, the late season (November and December) was quiet with only two tropical storms, Yamaneko and Pakhar (bottom quartile: 2), neither of which reached typhoon status. Despite the high level of activity in September, the rest of the season had a low number of storms. Overall, the 2022 season was characterized by below-normal levels of activity in the western North Pacific.

The total seasonal ACE in 2022 (Fig. 4.33a) was in the bottom quartile—the seventh lowest in the historical record. The ACE value was in the bottom quartile in the months of January–March, May, July, August, October, and November with zero ACE values in the months of January, February, March, and May, while July, October, and November ACE values were each the seventh or eighth lowest in the historical record. April and September ACE values were in the top quartiles for those months. ACE values in the peak and late season were in the bottom quartile and below the median in the early season. Climatologically, the months of July, August, September, and October contribute 11%, 19%, 23%, and 21% of the total ACE; in 2022, the highest ACE percentage occurred in September (56%), with July, August, and October contributions being low (3%, 18%, and 11%). Low seasonal ACE values are typical during La Niña events in the western North Pacific (Camargo and Sobel 2005), which was the case in 2022. Weaker and short-lived typhoons are characteristic of La Niña, which leads to low ACE values.

Four storms in 2022 had ACE values in the upper range for the climatological distribution of individual storms: Typhoon Noru and Super Typhoons Nanmadol, Muifa, and Hinnamnor. The ACE for Super Typhoon Hinnamnor was in the 99th percentile and contributed 24% of the total seasonal ACE for the basin, with the other three storms jointly contributing 35% of the total.

As is typical of La Niña events, the typhoon activity was shifted to the northwest part of the western North Pacific basin (Chia and Ropelewski 2002; Camargo and Sobel 2005; Camargo et al. 2007a), as seen in the storms' track and

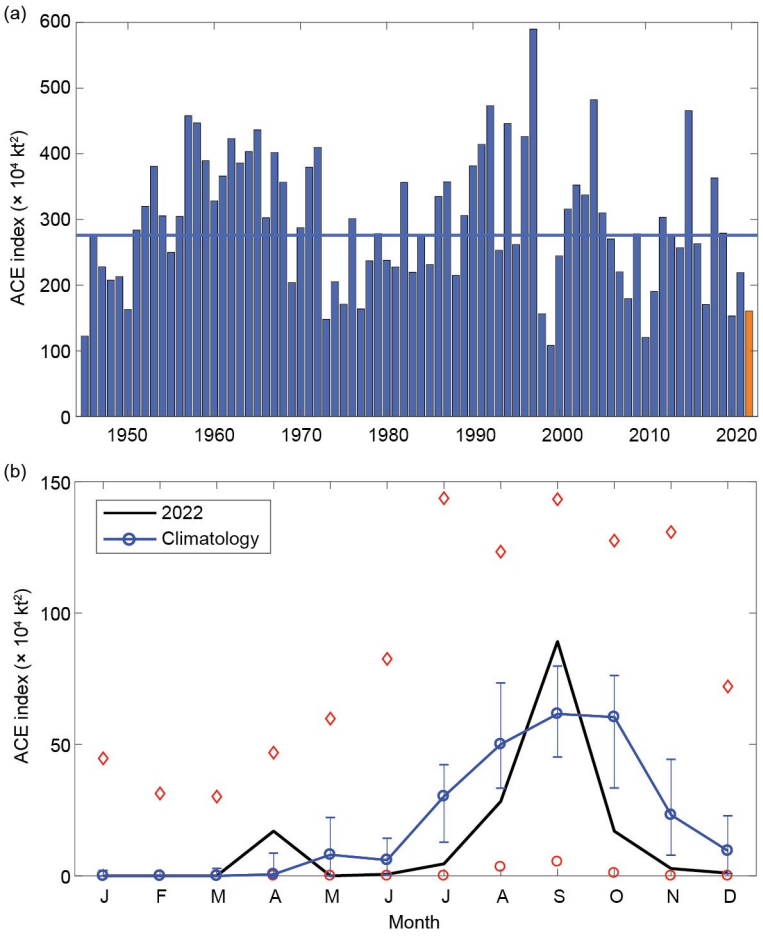

Fig. 4.33. (a) Accumulated cyclone energy (ACE) per year in the western North Pacific for 1945–2022. The solid blue line indicates the median for the 1991–2020 climatology. (b) ACE per month in 2022 (black line) and the median during 1991–2020 (blue line), where the blue error bars indicate the climatological interquartile range. In cases of no error bars, the upper and/or lower percentiles coincide with the median. The red diamonds and circles denote the maximum and minimum values, respectively, per month during the 1945–2021 period. (Source: 1945–2021 JTWC best-track dataset, 2022 JTWC preliminary operational track data.)

genesis locations (Figs. 4.34a,d) and in association with short tracks, weak storms, and low ACE values. The mean genesis position in 2022 was 19.5°N and 135.2°E, northwest of the climatological mean of 13.3°N and 140.5°E. These values are closer to the La Niña mean genesis positions 15.6°N and 136.3°E. Similarly, the mean track position in 2022 (21.5°N, 134.2°E) was northwest of the mean climatological track position (17.8°N, 135.9°E, with standard deviations of 1.6° and 5.2°, respectively).

In 2022, there were only 66.25 days with active named storms (bottom quartile: 86 days), the fifth-lowest number of active days in the historical record. From these active days, 33.25 had typhoons (bottom quartile: 42.7) and 12 days had major (including super) typhoons (SSHWS Categories 3–5; bottom quartile: 15.75). The percentage of active days with typhoons and major typhoons was 38% (median: 37%) and 14% (median: 15%), respectively. The median lifetime for TCs reaching tropical-storm intensity was 3.5 days (bottom quartile: 7 days) and for those reaching typhoon intensity was 6.25 days (bottom quartile: 7.75 days).

The longest-lived storm in 2022 was Typhoon Muifa (9.5 days), followed by Super Typhoon Hinnamnor (9.25 days), Tropical Storm Aere (8.5 days), and Typhoons Malakas (8.25 days) and Nalgae (7.75 days). None of the 2022 storms reached the top quartile of lifetime (10 days), and only the five named storms listed above had a duration above the median (7.25 days). During 13–14 September, three storms were active simultaneously in the basin: Typhoons Muifa, Merbok, and Nanmandol. This was the maximum number of simultaneous western North Pacific named storms in 2022. The record was set on 14–15 August 1996, with a total of six simultaneous named storms.

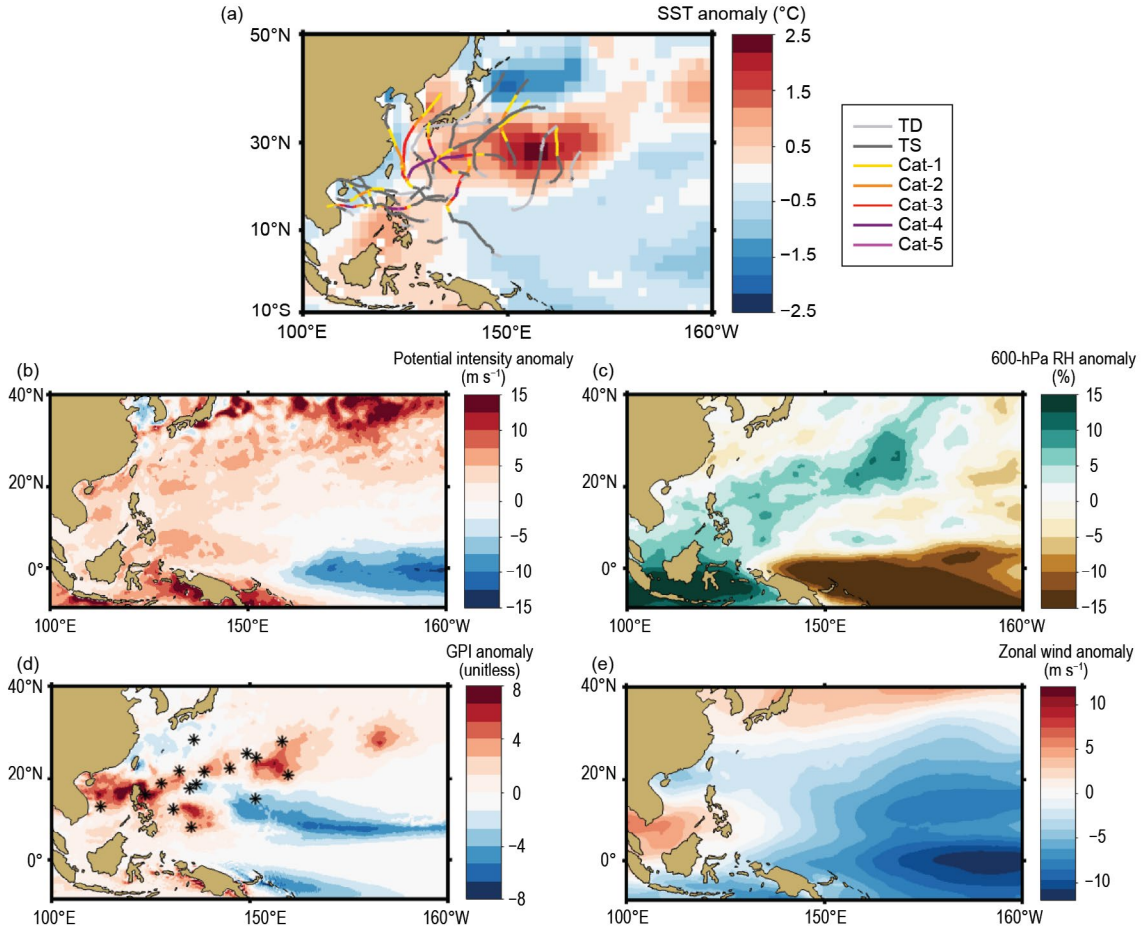

Fig. 4.34. Jul–Oct (JASO) 2022: (a) sea-surface temperature (SST) anomalies (°C) and the tracks of all 2022 storms with colors denoting their intensity; (b) potential intensity anomalies (m s^{-1}); (c) relative humidity 600-hPa anomalies (%); (d) genesis potential index anomalies and first position of JASO 2022 storms marked with an asterisk; and (e) zonal winds at 850 hPa (m s^{-1}). (Data sources: SST: ERSSTv5 [Huang et al. 2017]; other environmental fields: ECMWF ERA5 reanalysis [Hersbach et al. 2020], tracks and first position: JTWC preliminary operational track data.)

(iii) Environmental conditions

Figure 4.34 shows the tracks and environmental conditions associated with the 2022 typhoon season. The persistent La Niña strongly influenced the characteristics of the typhoon season. The SST anomalies (Fig. 4.34a) during the peak typhoon season of July–October (JASO) show a typical La Niña pattern, with below-normal SSTs in the eastern Pacific surrounded by above-normal SSTs. The typhoon tracks occurred in regions with warm SSTs (Fig. 4.34a). The potential intensity anomalies (Emanuel 1988; Fig. 4.34b) had similar characteristics, but with strong negative anomalies more concentrated in the equatorial region, surrounded by weak anomalies. Potential intensity anomalies were positive in the regions of warm SST anomalies.

In the equatorial region, there was a zonal dipole of mid-level relative humidity anomalies (Fig. 4.34c), with drier regions to the east and wetter to the west over the Maritime Continent. This equatorial band of wet anomalies extended poleward from southwest to the northeast, over the regions of positive SST anomalies. The genesis potential index (GPI; Fig. 4.34d; Emanuel and Nolan 2004; Camargo et al. 2007b) expresses the enhanced or reduced probability of TC formation through a nonlinear empirical combination of environmental factors known to affect TC genesis. In 2022, the JASO GPI showed positive anomalies in a southwest-to-northeast-oriented band starting in the South China Sea. These positive GPI anomalies were broadly co-located with areas of positive SST and moist relative humidity anomalies.

The genesis position of most typhoons in JASO 2022 occurred over or near this positive anomaly band. During La Niña events, the monsoon trough (defined by 850-hPa zonal wind anomalies) tends to be restricted to the western part of the basin. In 2022, this was clearly the case, with positive zonal winds anomalies (Fig. 4.34e) restricted to the region from the South China Sea to the Philippines. Many TCs tend to form along the edge of the monsoon trough, as was the case again in 2022. These environmental conditions help explain the low levels of activity in 2022, as only a small area in the western North Pacific had environmental conditions conducive to genesis formation, i.e., high SST, high potential intensity, and anomalously moist mid-level relative humidity during the peak typhoon season.

(iv) Tropical cyclone impacts

Including tropical depressions, 14 storms made landfall in 2022 (median: 17.5, 1961–2020 climatology). Landfall here is defined as when the storm track is over land and its previous location was over the ocean. In order to include landfall over small islands, tracks were interpolated from 6-hour to 15-minute intervals, and a high-resolution land mask was used. In the case of multiple landfalls, we considered the landfall with the highest intensity for each storm. Five storms made landfall as tropical depressions (top quartile: 5) and five as tropical storms (bottom quartile: 8). Four made landfall as typhoons (median: 4): Hinnamnor, Muifa, Nanmadol, and Noru. Noru made landfall as a major typhoon (bottom quartile: 1).

The largest economic impacts in terms of damage in 2022 were caused by Typhoons Hinnamnor ($1.5 billion U.S. dollars) and Nanmandol ($3.5 billion U.S. dollars; Gallagher Re 2023). Typhoon Hinnamnor hit Japan, Korea, and the Philippines. It was one of the strongest storms on record for South Korea. Nanmandol primarily affected Japan and Korea, with high rainfall rates that led to flooding. The most fatalities were caused by Tropical Storm Megi (or Agaton, 214 fatalities) and Typhoon Nalgae (or Paeng, 164 fatalities) in the Philippines, according to reports from the National Disaster Risk Reduction and Management Council and ReliefWeb.

5. NORTH INDIAN OCEAN

—C. J. Schreck

(i) Seasonal activity

The North Indian Ocean (NIO) TC season typically occurs between April and December, with two peaks of activity: May–June and October–December, due to the presence of the monsoon trough over tropical waters of the NIO during these periods. Tropical cyclone genesis typically occurs in the Arabian Sea and the Bay of Bengal between 8°N and 15°N. The Bay of Bengal, on average, experiences four times more TCs than the Arabian Sea (Dube et al. 1997).

The 2022 NIO TC season had seven named storms according to JTWC, which was above the IBTrACS–JTWC 1991–2020 climatology of 5.5. Two storms were in the Arabian Sea with the rest in the Bay of Bengal. Only one, Sitrang, became a cyclone, and none became major cyclones. These values were below the climatological averages of 2.2 cyclones and 1.1 major cyclones (Fig. 4.35). The 2022 seasonal ACE index (January–December) of 10.6 × 10^4 kt^2 was less than half of the 1991–2020 mean of 24.7 × 10^4 kt^2.

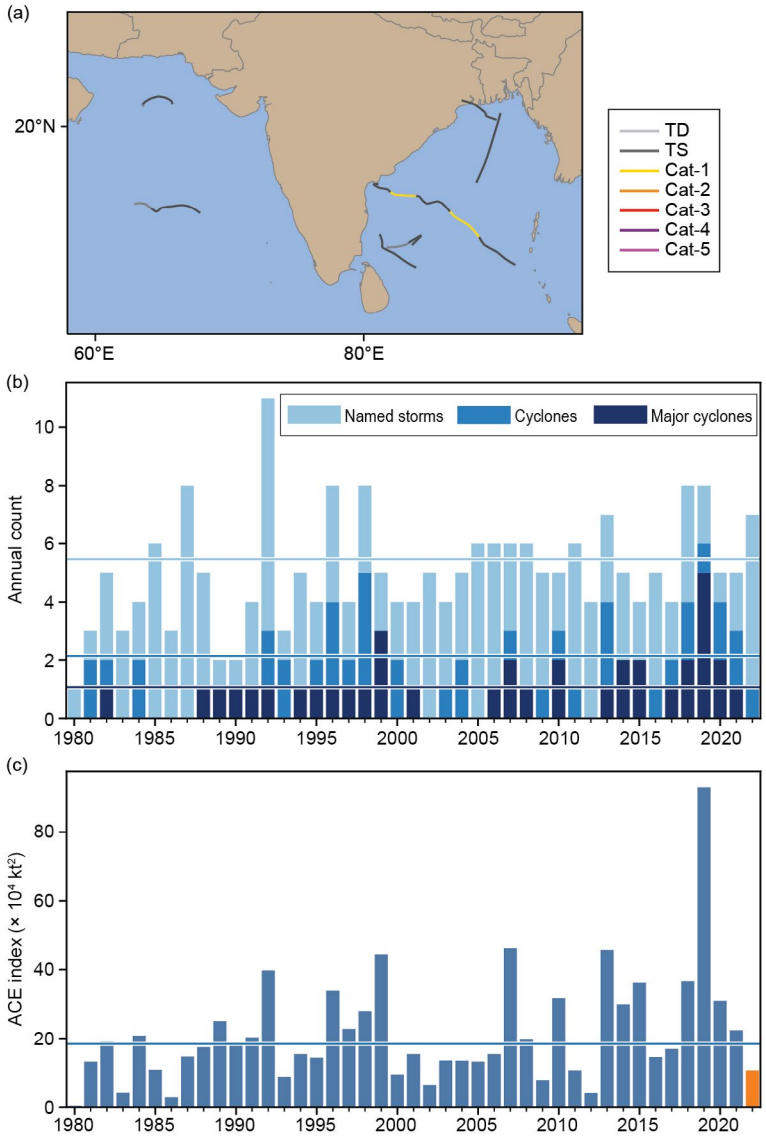

Fig. 4.35. Annual tropical cyclone statistics for the North Indian Ocean basin for 1990–2022: (a) storm tracks for 2022; (b) number of named storms, cyclones, and major cyclones; and (c) accumulated cyclone energy (ACE; × 10^4 kt^2). Horizontal lines, representing the 1991–2020 climatology, are included in both (b) and (c).

Indian Ocean dipole conditions, as measured by the Dipole Mode Index, were generally negative during 2022 (section 4f). During the post-monsoon period when three of the named storms occurred, SSTs were cooler in the western Arabian Sea and warmer in the Bay of Bengal (Fig. 4.36a). Convection was enhanced in the Bay of Bengal, where two tropical storms formed (Fig. 4.36b). Vertical wind shear was also below normal northward of 10°N (Fig. 4.36c), and low-level equatorial westerlies enhanced cyclonic vorticity in the basin (Fig. 4.36d). Overall, it was surprising that no storms reached tropical-cyclone strength amid these favorable environmental conditions.

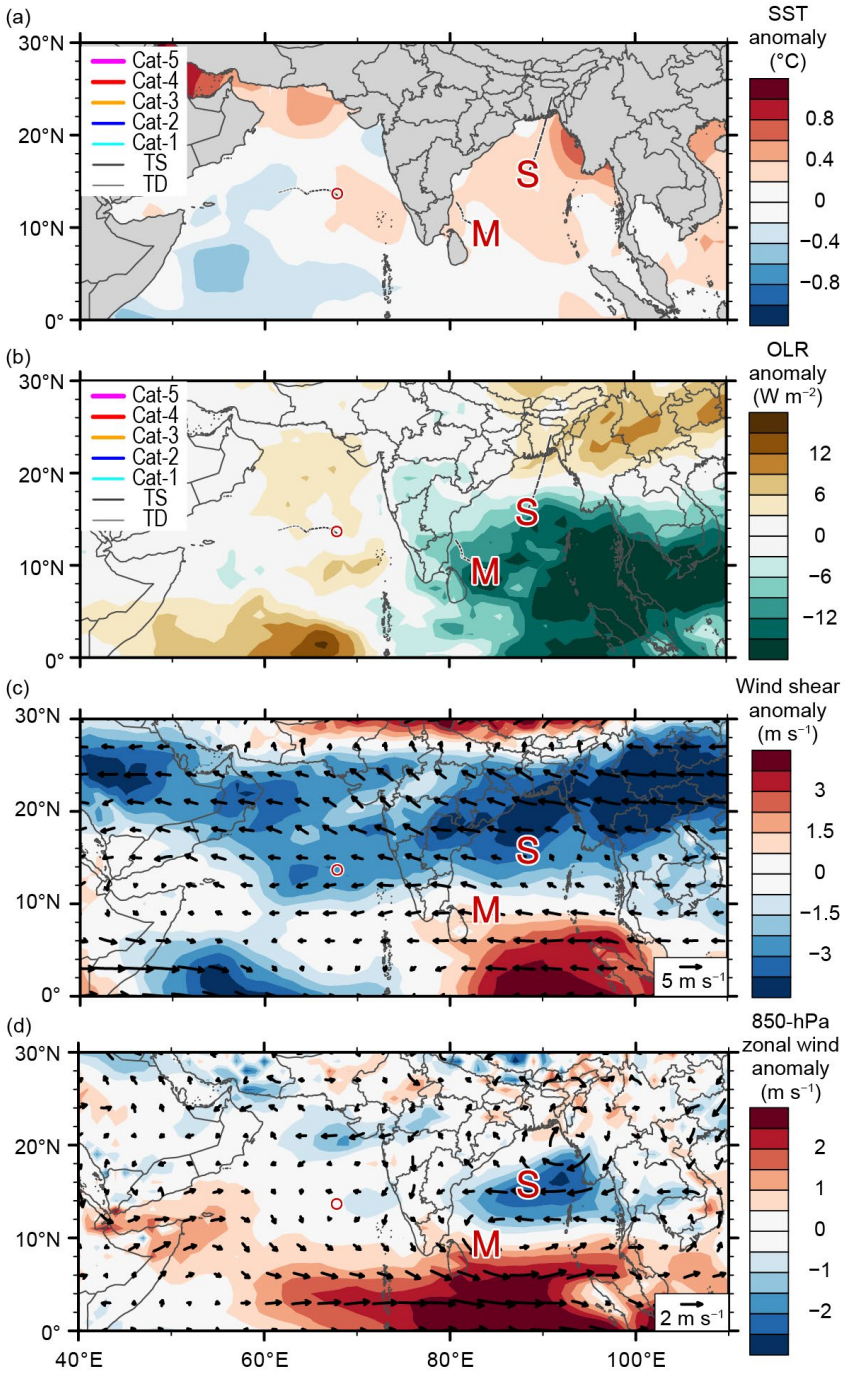

Fig. 4.36. Oct–Dec 2022 North Indian Ocean (NIO) anomaly maps of (a) SST (°C; Banzon and Reynolds 2013), (b) outgoing longwave radiation (OLR; W m^{-2}; Schreck et al. 2018); (c) 200-hPa–850-hPa vertical wind shear (m s^{-1}) vector (arrows) and scalar anomalies (shading), and (d) 850-hPa winds (m s^{-1}, arrows) and zonal wind anomalies (shading). Anomalies are relative to the annual cycle from 1991 to 2020. Letter symbols denote where each NIO tropical cyclone attained its initial tropical-storm intensity, and the red circle represents an unnamed tropical storm. (Source: wind data from CFSR [Saha et al. 2014].)

(ii) Individual tropical cyclones and impacts

The North Indian Ocean cyclone season had an early start with an unnamed tropical storm on 4 March. The strongest storm of the season was Severe Cyclone Asani in May. Asani's winds briefly reached Category 1 strength on the SSHWS on two occasions over the Bay of Bengal. However, Asani weakened to a tropical depression before making landfall in eastern India, which limited its impacts.

Tropical cyclones are uncommon during the Indian summer monsoon season, but two tropical storms formed in August: one in the Bay of Bengal and one in the Arabian Sea. Each only lasted for about 24 hours. Only two other years (1979 and 1982) have observed a North Indian Ocean storm during August. This was the first time on record there were multiple storms in August. In the India Meteorological Department best track data, the Bay of Bengal storm persisted as a depression for three days after landfall as it traversed northern India. Its remnants also contributed to severe flooding in Pakistan that inundated nearly 600,000 homes (Aon 2023).

Tropical Storm Sitrang formed in the Bay of Bengal in October. After initially moving westward, the storm made a sharp northward turn that led to landfall in Bangladesh. Its heavy rainfall and flooding damaged or destroyed about 10,000 homes and caused economic damage totaling in the tens of millions of U.S. dollars (Aon 2023).

6. SOUTH INDIAN OCEAN

—A. D. Magee and C. J. Schreck

(i) Seasonal activity

The South Indian Ocean (SIO) TC basin extends south of the equator and from the east African coastline to 90°E. While tropical cyclone activity can occur year-round, the peak season is typically between November and April when the Intertropical Convergence Zone is situated in the Southern Hemisphere. The 2021/22 season includes TCs that occurred from July 2021 to June 2022. Landfalling TCs typically impact Madagascar, Mozambique, and the Mascarene Islands, including Mauritius and La Réunion; however, impacts can be felt in other locations within the region. Below-average storm activity was observed in the SIO basin, with nine named storms according to JTWC, compared to the IBTrACS-JTWC 1991–2020 mean of 10.5 (Fig. 4.37). The five cyclones in 2021/22 were near average (6.1). All five also became major cyclones, which is above the average of 3.5. The 2021/22 season had an unusually late start, with Tropical Storm Ana forming on 23 January: the latest-starting SIO TC since 1998. A record number of named storms (six) made landfall in Madagascar during the season.

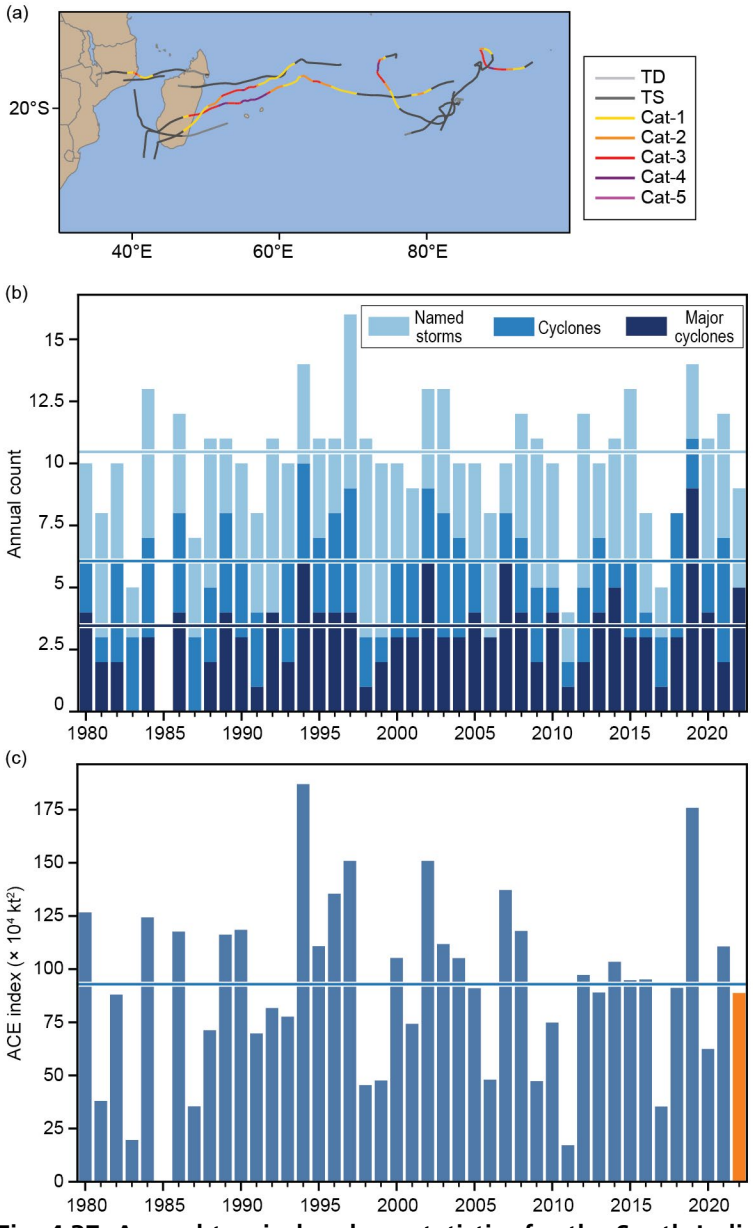

Fig. 4.37. Annual tropical cyclone statistics for the South Indian Ocean basin for 1980–2022: (a) storm tracks for the basin, (b) number of named storms, cyclones, and major cyclones, and (c) accumulated cyclone energy (ACE; × 10^4 kt^2). Horizontal lines represent the 1991–2020 climatology.

The 2021/22 seasonal ACE index was 88.8 × 10^4 kt^2, which is near the 1991–2020 climatology of 94.3 × 10^4 kt^2. Cyclone-favorable conditions, including anomalously high SSTs towards the east of the basin (Fig. 4.38a) and anomalously weak wind shear across the entire SIO (south of 15°S; Fig. 4.38c), were present.

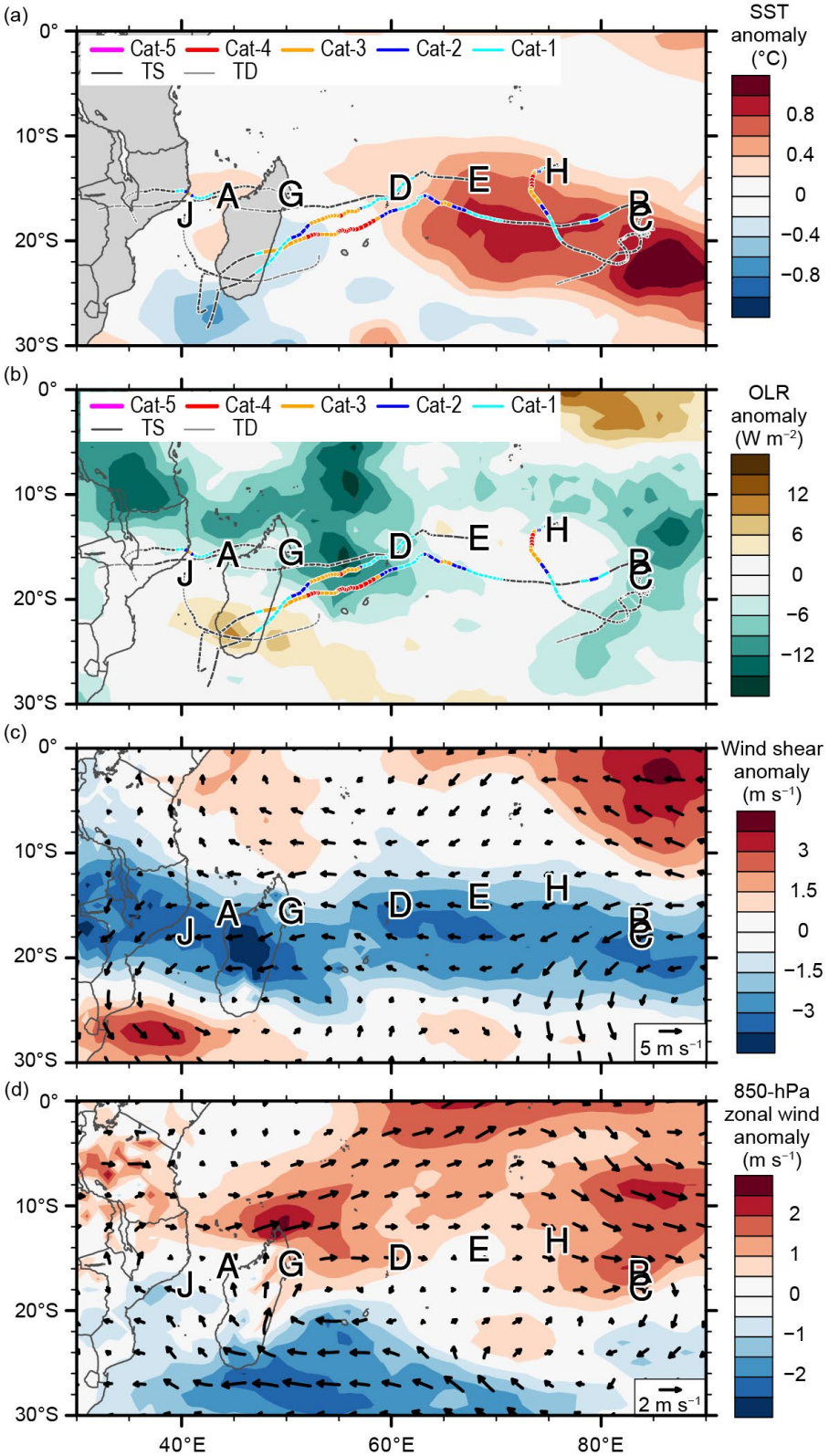

Fig. 4.38. Jan–Apr 2022 South Indian Ocean (SIO) anomaly maps of (a) sea-surface temperature (SST; °C; Banzon and Reynolds 2013), (b) outgoing longwave radiation (OLR; W m^{-2}; Schreck et al. 2018); (c) 200-hPa–850-hPa vertical wind shear (m s^{-1}) vector (arrows) and scalar anomalies (shading), and (d) 850-hPa winds (m s^{-1}, arrows) and zonal wind anomalies (shading). Anomalies are relative to the annual cycle from 1991 to 2020. Letter symbols denote where each SIO tropical cyclone attained its initial tropical-storm intensity (Source: wind data from CFSR [Saha et al. 2014].)

(ii) Noteworthy TCs and impacts

Tropical Storm Ana formed from an area of convection ~1200 km northeast of Madagascar. The system generally tracked to the southwest and made landfall between Toamasina and Île Sainte-Marie in Madagascar as a tropical depression. Upon entering the Mozambique Channel (24 January), favorable environmental conditions resulted in a peak intensity with maximum sustained winds of 50 kt (26 m s^{-1}) and a minimum central pressure of 993 hPa, which registered as a tropical storm event on the SSHWS. Shortly after, Ana made landfall in Mozambique. Ana reportedly resulted in over 140 fatalities, particularly impacting Madagascar, Mozambique, and Malawi. In Malawi, over 100,000 people were reportedly displaced, and most of the nation lost electricity. In Mozambique, approximately 10,000 houses were destroyed due to impacts associated with Ana.

Severe Tropical Cyclone Batsirai, the second and most intense tropical cyclone of the season, originated from a tropical disturbance in the central Indian Ocean. The compact system underwent periods of intensification and weakening, ultimately intensifying to an intense Category 4 cyclone on 2 February with maximum sustained winds of 125 kt (64 m s^{-1}) and a minimum central pressure of 932 hPa. The system continued to track westward toward Madagascar and made landfall as a Category 3 storm on 5 February near Nosy Varika, becoming the strongest cyclone to make landfall in Madagascar since Severe Tropical Cyclone Enawo in 2017. Batsirai particularly impacted La Reunion, where extreme wind and rainfall resulted in around $53 million (U.S. dollars) of agricultural losses and widespread power outages across the island. The majority of the impacts were observed in Madagascar, particularly in Nosy Varika. In total, 121 deaths were reported, over 100,000 people were displaced, and 120,000 homes were affected, with damage estimated at $190 million (U.S. dollars).

Tropical Storm Dumako (13–15 February) and Severe Tropical Cyclone Emnati (16–24 February) also made landfall in Madagascar within 18 days of Batsirai, marking the first time since January 1988 that three storms made landfall in Madagascar in a single month. Emnati initially formed from a tropical disturbance, favorable oceanic (SSTs ~28°C) and environmental conditions (low vertical wind shear), which promoted intensification while initially tracking westward and then southwestward towards southern Madagascar. Cyclone Emnati achieved peak intensity as a Category 4 system on the SSHWS, with maximum sustained winds of 115 kt (59 m s^{-1}) and a minimum central pressure of 941 hPa on 20 February. A total of 15 fatalities were reported, and extreme wind, rainfall, and associated flooding caused considerable damage to houses and road infrastructure.

Severe Tropical Cyclone Gombe originated from an area of disturbed weather approximately 500 km from Mauritius and tracked toward the west, where it made landfall across Nampula Province in northern Madagascar as a tropical storm. Upon entering the Mozambique Channel, Gombe intensified to reach a peak intensity of 100 kt (51 m s^{-1}) and a minimum central pressure of 959 hPa, a Category 3 system, on 11 March. Impacts from Gombe resulted in 72 deaths and substantial damage to tens of thousands of homes across Madagascar, Mozambique, and Malawi. Across Mozambique, approximately 500,000 people were impacted and nearly 50,000 homes were destroyed. Thousands of hectares of crops were affected, and widespread power outages were reported across the Nampula province.

Tropical Storm Jasmine (24–27 April) formed from a tropical depression near Comoros and initially tracked towards the southwest, making landfall near Nampula, Mozambique. The system then tracked along the coastline and re-entered the Mozambique Channel, where it intensified, reaching a peak intensity of 55 kt (28 m s^{-1}) and a minimum central pressure of 984 hPa. Jasmine tracked on towards the southeast, making a second landfall across Toliara in Madagascar on 26 April, resulting in three deaths. The storm dissipated on 27 April after re-entering the southern Indian Ocean.

7. AUSTRALIAN BASIN

—B. C. Trewin

(i) Seasonal activity

The 2021/22 TC season was near normal in the broader Australian basin (areas south of the equator and between 90°E and 160°E[4], which includes Australian, Papua New Guinean, and Indonesian areas of responsibility). The season produced 12 TCs in a season with weak to moderate La Niña conditions. The 1991–2020 IBTrACS-JTWC seasonal averages for the basin are 10.2 named storms, 5.0 TCs, and 2.5 major TCs, which compares with the 2021/22 IBTrACS-based counts of 12, 4, and 1, respectively (Fig. 4.39; Table 4.2), and is consistent with La Niña conditions. There were seven TCs in the western sector[5] of the broader Australian region during 2021/22, two in the northern sector, and three in the eastern sector. Two TCs (Tiffany and Seth) made landfalls in Australia as tropical cyclones.

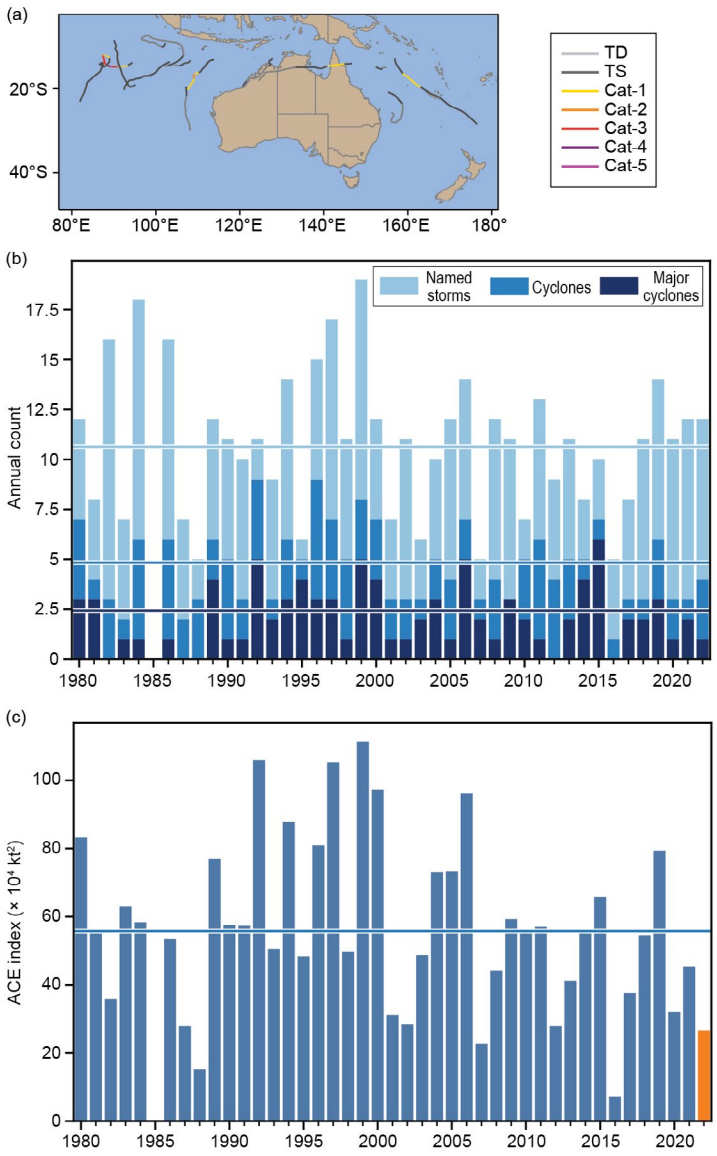

Fig. 4.39. Annual tropical cyclone statistics for the Australian basin for the period 1980–2022: (a) storm tracks for the basin, (b) number of named storms, cyclones, and major cyclones, and (c) accumulated cyclone energy (ACE; × 10^4 kt^2). Horizontal lines represent the 1991–2020 climatology.

(ii) Landfalling and other significant TCs

The major impacts of tropical cyclones in Australia in the 2021/22 season resulted from flooding, most of which occurred from remnant lows well after the systems dropped below tropical-cyclone intensity. Tropical Cyclone Tiffany formed east of Cape York Peninsula and reached tropical-cyclone intensity on 9 January. Maximum sustained 10-minute winds reached 55 kt (28.3 m s^{-1}) early on 10 January, shortly before landfall on the east coast near Cape Melville. The system weakened below cyclone intensity as it crossed Cape York Peninsula but re-intensified after reaching the Gulf of Carpentaria. It made a second landfall on 12 January with 10-minute winds of 50 kt (25.7 m s^{-1}) near Port Roper, on the Gulf's southwest coast. Both landfalls brought limited wind damage, mostly to vegetation. The remnant low initially tracked west across the Northern Territory into the Kimberley region of Western Australia, before turning south on 15 January and moving southeast before dissipating in the far northwest of South Australia on 17 January. Flooding occurred along much of Tiffany's track but was especially significant in the normally arid inland areas of South Australia, with weekly rainfall totals for the 17–23 January period widely exceeding 50 mm and locally exceeding 200 mm. Cortlinye (33.0°S, 136.3°E), near Kimba, had a daily rainfall total of 206.0 mm, a January

[4] The Australian Bureau of Meteorology's warning area overlaps both the southern Indian Ocean and southwest Pacific.

[5] The western sector covers areas between 90°E and 125°E. The eastern sector covers areas east of the eastern Australian coast to 160°E, as well as the eastern half of the Gulf of Carpentaria. The northern sector covers areas from 125°E east to the western half of the Gulf of Carpentaria. The western sector incorporates the Indonesian area of responsibility, while the Papua New Guinea area of responsibility is incorporated in the eastern sector. Some cyclones crossed two or more sectors.

record for South Australia. There was severe flooding in places, and the main road and rail links between South Australia and the Northern Territory along with the railway to Western Australia were closed for extended periods.

Tropical Cyclone Seth was a long-lived system, although it only reached tropical-cyclone intensity briefly in the Coral Sea. The precursor low formed north of Darwin on 24 December and tracked east across northern Australia, emerging over the Coral Sea near Cairns on 30 December and reaching tropical-cyclone intensity near 19°S, 15°E on 31 December. After peaking later that day with maximum sustained 10-minute winds of 55 kt (28.3 m s^{-1}), with a maximum gust of 82 kt (42.2 m s^{-1}) at Frederick Reef (20.9°S, 154.4°E), Seth weakened quickly and fell below cyclone intensity by the evening of 1 January. The remnant low turned and moved slowly towards the east coast, reaching the coast near Hervey Bay on 7 January. Extreme rainfall totals occurred to the south of the landfall point, with a number of sites receiving more than 400 mm in 24 hours, the highest total being 674 mm at Marodian (25.9°S, 152.3°E). Major flooding occurred in the Mary and Burnett Rivers, with 30 homes and 50 businesses damaged by floodwaters in Maryborough and two confirmed deaths in the region.

The season's other landfalling system was Anika, which formed in the Timor Sea on 24 February. It reached tropical-cyclone intensity on 25 February and moved south towards the far north of Western Australia, reaching maximum sustained 10-minute winds of 50 kt (25.7 m s^{-1}) before making landfall near Kalumburu late on 26 February. Anika weakened quickly below cyclone intensity over land and tracked generally southwest parallel to the West Kimberley coast, re-emerging over water north of Broome on 1 March and intensifying to regain cyclone intensity on 2 March. It made a second landfall late that day at Wallal Downs, east of Port Hedland, having regained its earlier peak intensity of 10-minute sustained winds of 50 kt. Peak 24-hour rainfall totals included 333 mm at Truscott and 250 mm at Kalumburu on 27 February. Only minor damage was reported along Anika's path, along with some localized flooding.

The two most intense systems of the season were Vernon in late February and Charlotte in late March. Both cyclones were well to the west of Western Australia and did not affect any land areas. Vernon reached 10-minute sustained winds of 100 kt (51.4 m s^{-1}) near 15°S, 91°E on 26 February just before leaving the Australian region, while Charlotte had 10-minute sustained winds of 90 kt (46.3 m s^{-1}) near 17°S, 109°E on 22 March. Neither cyclone had any significant impacts.

Historically, La Niña years have had more TCs in the Australian region (and El Niño years fewer), both in the Pacific and Indian Ocean sectors (Nicholls 1979). However, recent La Niña events have failed to produce high numbers of TCs (although recent El Niños have produced low numbers). Even the strong 2010/11 La Niña was associated with only a near-average number of TCs, although there were also a large number of tropical lows that failed to reach TC intensity. It is unclear whether this is the same El Niño–Southern Oscillation variability superimposed on an overall downward trend or whether other factors are contributing to the La Niña-TC relationship. ACE values for this basin are summarized in Table 4.2.

8. SOUTHWEST PACIFIC BASIN

—A.D. Magee, A. M. Lorrey, and H. J. Diamond

(i) Seasonal activity

The 2021/22 Southwest Pacific tropical cyclone season officially began in November 2021 and ended in April 2022. Data for the season were gathered from the Fiji Meteorological Service, Australian Bureau of Meteorology, and New Zealand MetService, Ltd. The Southwest Pacific basin, defined by Diamond et al. (2012) as 135°E–120°W, experienced a total of seven tropical cyclones, including two severe storms. In addition, there was one out-of-season tropical cyclone that occurred in May.

Figure 4.40 (and Table 4.2) illustrates and documents the tropical cyclone activity in the basin, which spans the area 160°E–120°W to avoid overlap with the Australian basin and double counting of storms. It is important to note that the climatological definition of the Southwest Pacific basin (Diamond et al. 2012) is used for this seasonal description and does not align with WMO-designated boundaries for RSMC or Tropical Cyclone Warning Centre areas of responsibility.

In comparison to the 1991–2020 seasonal average of 9.8 named tropical cyclones, including 4.3 severe storms, as reported by the Southwest Pacific Enhanced Archive for Tropical Cyclones (SPEArTC), the 2021/22 Southwest Pacific tropical cyclone season was considered to be below normal. All winds reported are 10-minute averaged winds as noted in Diamond et al (2012).

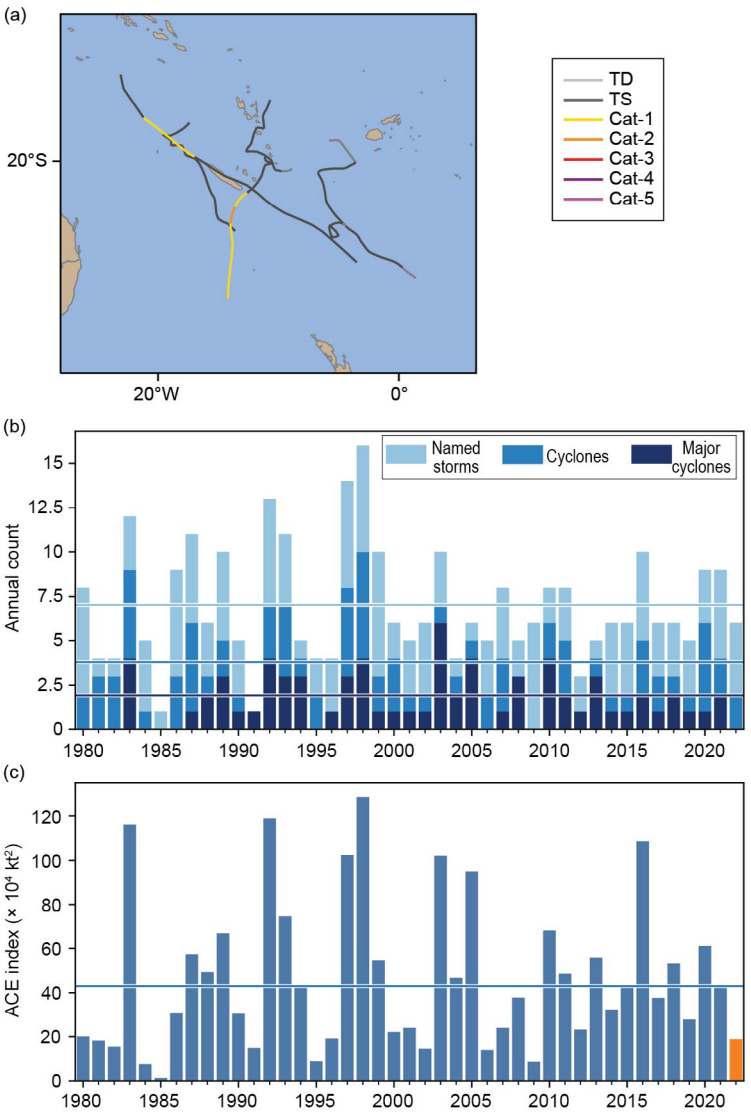

Fig. 4.40. Annual tropical cyclone statistics for the Southwest Pacific basin for the period 1990–2022: (a) storm tracks, (b) number of named storms, cyclones, and major cyclones, and (c) accumulated cyclone energy (ACE; × 10^4 kt^2). Horizontal lines represent the 1991–2020 climatology.

(ii) Storm tracks, landfalls, and impacts

Tropical Cyclone Ruby, the first TC of the 2021/22 Southwest Pacific tropical cyclone season, initially formed as a tropical low in the Solomon Sea on 9 December. The low tracked towards the southeast and continued to intensify, eventually achieving peak intensity on 13 December, with maximum winds of 60 kt (31 m s^{-1}) and a minimum central pressure of 975 hPa. Ruby made landfall in New Caledonia, impacting electricity and transportation services across northern Grande Terre. This storm brought 303 mm of rainfall to Riviere Blanche on the southeastern side of the island, with maximum wind gusts of nearly 100 kt (51 m s^{-1}) reported at Poingam.

Severe Tropical Cyclone Cody, the first severe TC for the season, initially formed as a tropical depression to the northwest of Fiji. Strong wind shear in the region briefly inhibited intensification; however, the system organized and achieved Category 1 intensity to the southwest of Viti Levu, Fiji. Cody reached peak intensity of 70 kt (36 m s^{-1}) and a minimum central pressure of 980 hPa on 1 December. Cody resulted in one fatality, while flooding and other storm impacts

displaced approximately 5000 people, who took shelter at numerous evacuation centers across Fiji's Western, Central, and Northern Divisions. Damage in Fiji from Cody was estimated at $25 million (U.S. dollars).

The season's second severe tropical cyclone, Dovi, originated as a tropical low in the eastern Coral Sea. The system initially tracked eastward towards Vanuatu, slowed, and began to intensify near Southern Vanuatu. On 9 February, the tropical low was named Tropical Cyclone Dovi and tracked to the south as a Category 1 system. As Dovi continued to intensify, it passed off the east coast of New Caledonia as a Category 3 system on 10 February. Dovi reached its peak intensity as an Australian Category 4 storm with sustained winds of 95 kt (49 m s^{-1}) and a minimum central pressure of 940 hPa on 11 February. Dovi then passed west of Norfolk Island and continued to track south, transitioning to a subtropical system as it approached New Zealand. The severe tropical cyclone caused significant flooding and power outages in Vanuatu and New Caledonia. The North Island of New Zealand was severely impacted by Dovi after it became an ex-tropical cyclone, particularly in the Bay of Plenty and Hawke's Bay regions where a significant number of homes were damaged. The strong winds from this decaying system caused power and communication lines to be disrupted, leaving many residents without electricity or phone services. High winds also closed the Auckland Harbour Bridge, which is a main thoroughfare. In addition, the water supply was compromised in the town of Featherston during this storm, and uprooted trees and broken tree limbs resulted in damage to water and road infrastructure. Approximately $35 million (U.S. dollars) in damage was attributed to Dovi in New Zealand alone.

One out-of-season TC occurred in May: Tropical Cyclone Gina. Forming approximately 400 km northeast of Port Vila, Vanuatu, in an area of favorable oceanic (SSTs around 30°C) and environmental (low-to-moderate vertical wind shear) conditions, the tropical depression continued to intensify as it tracked westward towards Vanuatu. On 18 May, Gina reached maximum intensity of 35 kt (18 m s^{-1}) and a minimum central pressure of 998 hPa and maintained Category 1 intensity for approximately 48 hours, continuing to track towards the southeast. Prolonged and intense rainfall from Gina caused flooding in parts of Vanuatu and resulted in the temporary closure of Port Vila's Bauerfield Airport.

h. Tropical cyclone heat potential

—F. Bringas, G. J. Goni, I-I Lin, and J. A. Knaff

Tropical cyclone heat potential (TCHP; e.g., Goni et al. 2009, 2017) is an indicator of the available heat stored in the upper ocean that can potentially induce tropical cyclone (TC) intensification and regulate ocean–atmosphere enthalpy fluxes and TC-induced sea-surface temperature (SST) cooling (e.g., Lin et al. 2013). TCHP is calculated as the integrated heat content between the sea surface and the 26°C isotherm (D26), which is generally taken to be the minimum temperature required for TC genesis and intensification (Leipper and Volgenau 1972; Dare and McBride 2011).

Provided that atmospheric conditions are favorable, TC intensification, including rapid intensification, has been associated with areas in the ocean that have TCHP values above 50 kJ cm^{-2} (e.g., Shay et al. 2000; Mainelli et al. 2008; Lin et al. 2014, 2021; Knaff et al. 2018, 2020). High SSTs prior to TC formation usually lead to less SST cooling during the lifetime of the TC, and hence higher enthalpy fluxes from the ocean into the storm, which favors intensification (e.g., Lin et al. 2013). Similarly, upper-ocean salinity is another condition of relevance for TC intensification because fresh water-induced barrier layers may also modulate the upper-ocean mixing and cooling during a TC and thus the air–sea fluxes (e.g., Balaguru 2012; Domingues et al. 2015). Upper-ocean thermal conditions observed during 2022 are presented here in terms of two parameters: 1) TCHP anomaly values with respect to their long-term mean (1993–2020) and 2) TCHP anomaly values compared to conditions observed in 2021. TCHP anomalies during 2022 (Fig. 4.41) are computed for June–November in the Northern Hemisphere and November 2021–April 2022 in the Southern Hemisphere. In Fig. 4.41, the seven regions where TCs are known to form, travel, and intensify are highlighted. In all of these regions, TCHP values exhibit large

temporal and spatial variability due to mesoscale features, trends, and short- to long-term modes of variability, such as the North Atlantic Oscillation, El Niño–Southern Oscillation (ENSO), and the Pacific Decadal Oscillation. The differences in TCHP anomalies between 2021 and 2022 are also computed for the primary months of TC activity in each hemisphere (Fig. 4.42).

During 2022, TCHP anomaly conditions were above average for most TC regions and basins, with the exception of the eastern North Pacific, the southern portion of the South Indian, and near the center of the North Atlantic Gyre (Fig. 4.41). In particular, some areas in the North Indian Ocean, western North Pacific Ocean, east and west of Australia, and portions of the North Atlantic Ocean exhibited TCHP anomaly values above 30 kJ cm^{-2}, which are indicative of favorable oceanic conditions for the development and intensification of TCs.

Compared to 2021, TCHP anomalies during 2022 were larger in some regions of the western North Pacific and North Atlantic, most of the Gulf of Mexico, and much of the Southern Hemisphere. They were notably smaller in the central and eastern Pacific. These lower TCHP anomalies during 2022 were associated with the ongoing and stronger negative phase of ENSO (La Niña), prevalent in this region since mid-2021 (Fig. 4.42). In the Southern Hemisphere, TCHP anomalies during 2022 were average or above average, with values above 30 kJ cm^{-2} in small areas in the South Indian Ocean and more extended areas in the southwestern Pacific (Fig. 4.41). TCHP anomalies in 2022 were on average similar to those observed in 2021 in most of the Southern Hemisphere, with most areas showing differences between ±10 kJ cm^{-2}, except for the southwestern Pacific (Fig. 4.42).

In the South Indian Ocean basin, the most intense storm of the season was Batsirai, which after being named on 28 January, underwent several periods of intensification and weakening until experiencing rapid intensification from Category 2 to Category 4 on 2 February, when it reached its peak intensity of 125 kt (64 m s^{-1}) and a minimum central barometric pressure of 932 hPa, while traveling over a region with SST >27°C and TCHP >50 kJ cm^{-2}. Similar to Batsirai, Cyclone Gombe underwent rapid intensification on 9 March over a period of 18 hours while traveling over the Mozambique Channel with SST >30°C and TCHP >80 kJ cm^{-2}, reaching peak intensity of 110 kt (57 m s^{-1}) and a minimum central barometric pressure of 959 hPa.

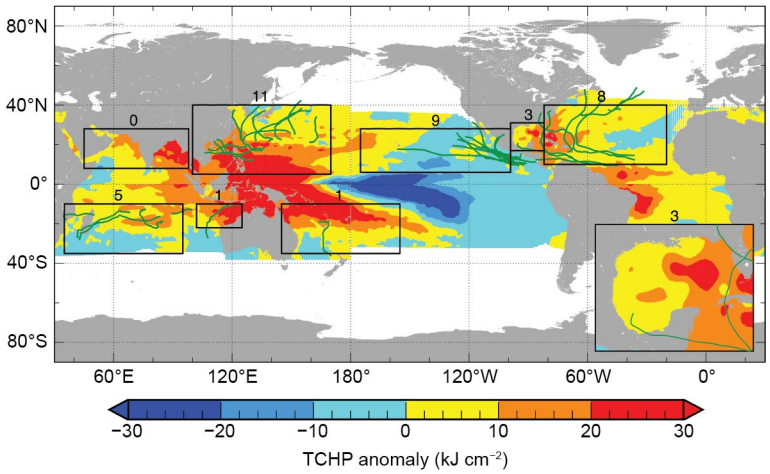

Fig. 4.41. Global anomalies of tropical cyclone heat potential (TCHP; kJ cm^{-2}) during 2022. The boxes indicate the seven regions where TCs occur: from left to right, southwest Indian, North Indian, west North Pacific, southeast Indian, South Pacific, east Pacific, and North Atlantic (shown as Gulf of Mexico and tropical Atlantic separately). The green lines indicate the trajectories of all tropical cyclones reaching at least Category 1 intensity (one-minute average wind ≥64 kt, 34 m s^{-1}) and above during Nov 2021–Apr 2022 in the Southern Hemisphere and Jun–Nov 2022 in the Northern Hemisphere. The numbers above each box correspond to the number of Category 1 and above cyclones that traveled within that box. The Gulf of Mexico conditions are shown in the inset in the lower right corner.

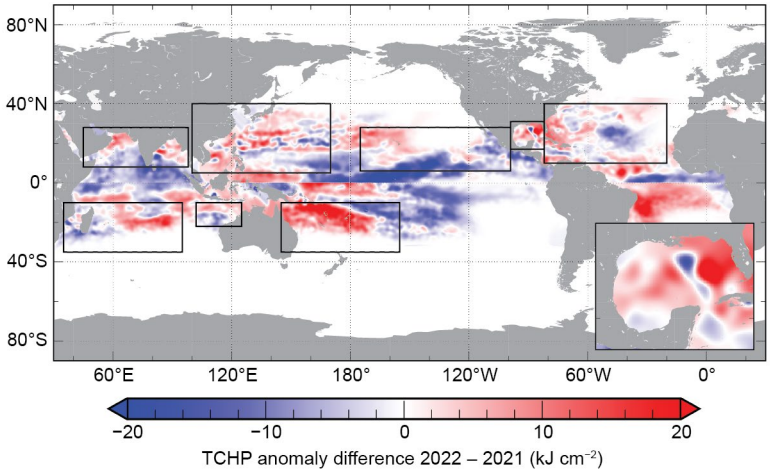

Fig. 4.42. Tropical cyclone heat potential (TCHP) anomaly difference between the 2022 and 2021 tropical cyclone seasons (kJ cm^{-2}; Jun–Nov in the Northern Hemisphere and Nov–Apr in the Southern Hemisphere). The Gulf of Mexico conditions are shown in the inset in the lower right corner.

Large positive areas of high TCHP anomaly values were observed in the regions east and west of Australia where TCs typically translate. However, in 2021/22, below-average TC activity was observed in these two regions with a total of 10 TCs, of which only 2 reached Category 1 intensity or above.

Similar to the eastern and western Australia regions, the North Indian Ocean experienced above-average TCHP anomalies in excess of 30 kJ cm^{-2} during 2022 in the Bay of Bengal and northern Arabian Sea. No Category 1 or above storms were recorded during June–November (Fig. 4.41), which made for a below-average season in terms of TC intensity. One caveat associated with this result is that almost all TCs forming in this region do so during the pre- and post-monsoon seasons (May–June and October–December).

In the western North Pacific basin, the upper-ocean thermal conditions are largely modulated by the state of ENSO (e.g., Lin et al. 2014, 2020; Zheng et al. 2015). During all of 2022, La Niña was observed in this region with TCHP anomalies that were positive in the western North Pacific, with values well above 30 kJ cm^{-2} closer to the equator and a regional average of approximately 20 kJ cm^{-2} when compared to the long-term mean (Fig. 4.41), as is typical in a La Niña year (Lin et al. 2014; 2020). TCHP anomalies in the western North Pacific were fairly similar in 2021 and 2022, likely due to the predominance of La Nina conditions in both years (Fig. 4.42). Due to the influence of La Niña, TC activity during 2022 was below average for the western North Pacific. Nevertheless, there were two notable super typhoons: Hinnamnor and Nanmadol. Hinnamnor originated and intensified to Category 5 (140 kt; 72 m s^{-1}) over a region of high TCHP (>60 kJ cm^{-2}), though at relatively high latitudes (~22°N–26°N). The storm reached its lifetime maximum intensity (LMI) of 140 kt (72 m s^{-1}) on 30 August. After a short period of intensity fluctuation to ~125 kt (64 m s^{-1}), Hinnamnor intensified back to 140 kt on 1 September. The most noteworthy feature in Hinnamnor was its sharp 90° turn in its track that was accompanied by dramatic reduction of its forward motion to near-stationary (i.e., ~1 m s^{-1} to 2 m s^{-1}) on 1–2 September. As a result of this slowing, a large cold pool was induced and contributed to Hinnamnor's weakening to ~75 kt (39 m s^{-1}). Super Typhoon Nanmadol also originated and intensified over areas with TCHP >50 kJ cm^{-2}, and similarly at a relatively high latitude of ~21°N–26°N. It reached its LMI of 135 kt (69 m s^{-1}) on 16 September. After LMI, Nanmadol maintained a northwest track while steadily weakening before it made landfall in Japan and affected both Japan and South Korea.

In the North Atlantic basin, upper-ocean thermal conditions during the 2022 hurricane season were characterized by TCHP anomalies larger than the long-term average except in areas of the eastern portion of this region, west of Africa, with values on the western part of the basin of around 20 kJ cm^{-2} on average for most of the region and up to 30 kJ cm^{-2} in smaller areas around Cuba (Fig. 4.41). TCHP anomalies were also positive during 2022 in areas associated with the location of the Loop Current's northern extension in the Gulf of Mexico, where these anomalies were greater than 25 kJ cm^{-2} during 2022 compared to the long-term mean. Differences of ±20 kJ cm^{-2} between 2022 and 2021 were observed, likely as a result of the variability of ocean currents in the region.

Hurricane Fiona formed during 12–14 September, despite environmental conditions considered to be only marginally favorable. The system became a named storm on 15 September while moving towards the Caribbean Sea region. After becoming a Category 3 hurricane, Fiona traveled over Puerto Rico and the Dominican Republic, where it weakened slightly, but emerged in the tropical North Atlantic and intensified into a Category 4 TC on 21 September. Fiona reached peak intensity of one-minute sustained wind speeds of 115 kt (58 m s^{-1}) and a minimum central barometric pressure of 932 hPa while traveling over a region with SST >30°C and TCHP >80 kJ cm^{-2}, which is well above the 50-kJ cm^{-2} threshold required to support Atlantic hurricane intensification (Mainelli et al. 2008).

Major Hurricane Ian, the most intense Atlantic storm in 2022, reached Category 1 intensity on 26 September, and intensified to a Category 3 system while approaching the southwestern tip of Cuba. Ian continued traveling north into the Gulf of Mexico, where on 28 September it

strengthened into a Category 5 hurricane with peak intensity of one-minute sustained wind speeds of 140 kt (72 m s^{-1}) and minimum central barometric pressure of 936 hPa, while traveling over a region with SST >31°C and TCHP > 115 kJ cm^{-2}. Ian then made landfall as a Category 4 hurricane in Florida.

In summary, favorable upper-ocean thermal conditions were observed in all TCHP basins during the 2022 season, except in the eastern North Pacific, where conditions were slightly below average compared to the long-term mean. Additionally, TCHP anomaly values during 2022 exhibited generally similar values in most regions compared to the previous year in most basins, with higher values reported in the western North Atlantic and the eastern Australia regions. This translated into above-average hurricane activity in the South Indian region, average activity in the North Atlantic and eastern North Pacific, and below-average activity in the northwest Pacific and North Indian Oceans. Several significant storms, including Intense Cyclones Batsirai and Gombe in the southwestern Indian Ocean, Super Typhoons Hinnamnor and Nanmadol in the western North Pacific, and Major Hurricanes Fiona and Ian in the North Atlantic, Caribbean Sea, and Gulf of Mexico, underwent rapid intensification while traveling over areas with favorable ocean conditions including high TCHP values.

Sidebar 4.1: Hurricanes Fiona and Ian: A pair of impactful North Atlantic major hurricanes

—C. FOGARTY, R. TRUCHELUT, AND P. KLOTZBACH

Both major hurricanes that formed during the 2022 Atlantic hurricane season (Fiona and Ian) caused tremendous damage and loss of life. This sidebar details the meteorology and briefly summarizes the impacts that these storms caused. Here we highlight the damage that Fiona caused in the Atlantic Provinces of Canada and that Ian caused in Florida. We also note that Fiona also caused massive flooding damage in Puerto Rico, and Ian caused significant wind and storm surge damage in Cuba. Observed statistics are taken from the National Hurricane Center (NHC)'s Tropical Cyclone Reports on Fiona (Pasch et al. 2023) and Ian (Bucci et al. 2023).

Hurricane Fiona developed from a tropical wave off the coast of Africa, reaching tropical depression status ~8000 km east of Guadeloupe on 14 September. Later that day, the NHC designated the system Tropical Storm Fiona, and on 18 September an eye formed, with Fiona reaching hurricane status as it approached southwestern Puerto Rico, where it caused heavy flooding and severe power outages. The storm reached major hurricane status on 20 September while traversing the eastern Bahamas. Fiona reached its peak intensity as a Category 4 storm (120 kt; 62 m s^{-1}) with a minimum pressure as a tropical system of 931 hPa 42 hours later as it tracked just northwest of Bermuda. The pressure rose to 940 hPa after Fiona passed Bermuda, and then the system underwent a volatile extratropical transition process late on 23 September and early on 24 September while still maintaining winds of Category 3 intensity (100 kt; 51 m s^{-1}). During the early hours of 24 September, Fiona made landfall in eastern Nova Scotia as a Category 2-force severe post-tropical cyclone with a minimum sea-level pressure of 931 hPa—the lowest ever recorded sea-level pressure of any cyclone over land in Canada. The storm rapidly accelerated as it approached Nova Scotia, then slowed significantly near Cape Breton. Fiona weakened as it moved slowly northward through the Gulf of St. Lawrence on 25 September and into the Labrador Sea. Fiona dissipated by 28 September.

Fiona was the most intense and most destructive tropical or post-tropical cyclone in Atlantic Canada's history. The extratropical transition (ET) was truly remarkable since an approaching upper-level potential vorticity anomaly interacted with the storm while it was still a major hurricane. The cloud and wind field expanded exceptionally quickly, with most of the ET process occurring over a 12-hour period from 1200 UTC on 23 September to 0000 UTC on 24 September. The damage swath of the storm was immense and occurred not just over the eastern (right-of-track) sector, but also over a large region west of the track where, in fact, the highest winds were observed (Fig. SB4.1). These winds were actually from the baroclinic energetics portion of the storm and were more persistent and produced greater storm surge than on the east side. The slow forward motion of Fiona worsened the impacts overall. Trapped-fetch wave growth (Bowyer and MacAfee 2005) east of the track over parts of northern Cape Breton and southwestern Newfoundland caused extensive damage and was responsible for the complete destruction of numerous homes

in the town of Port Aux Basques where an all-time record water level was recorded.

Many have described Fiona as Canada's version of Superstorm Sandy, which devastated the northeastern United States in 2012. The event was like no other in the modern era for Atlantic Canada. The closest analog is the 1873 Great Nova Scotia Cyclone, which had a similar track and similar impacts anecdotally. The financial toll was only second to post-tropical storm Hazel in 1954, which brought severe flooding over the populated Toronto region. Total estimated insured costs

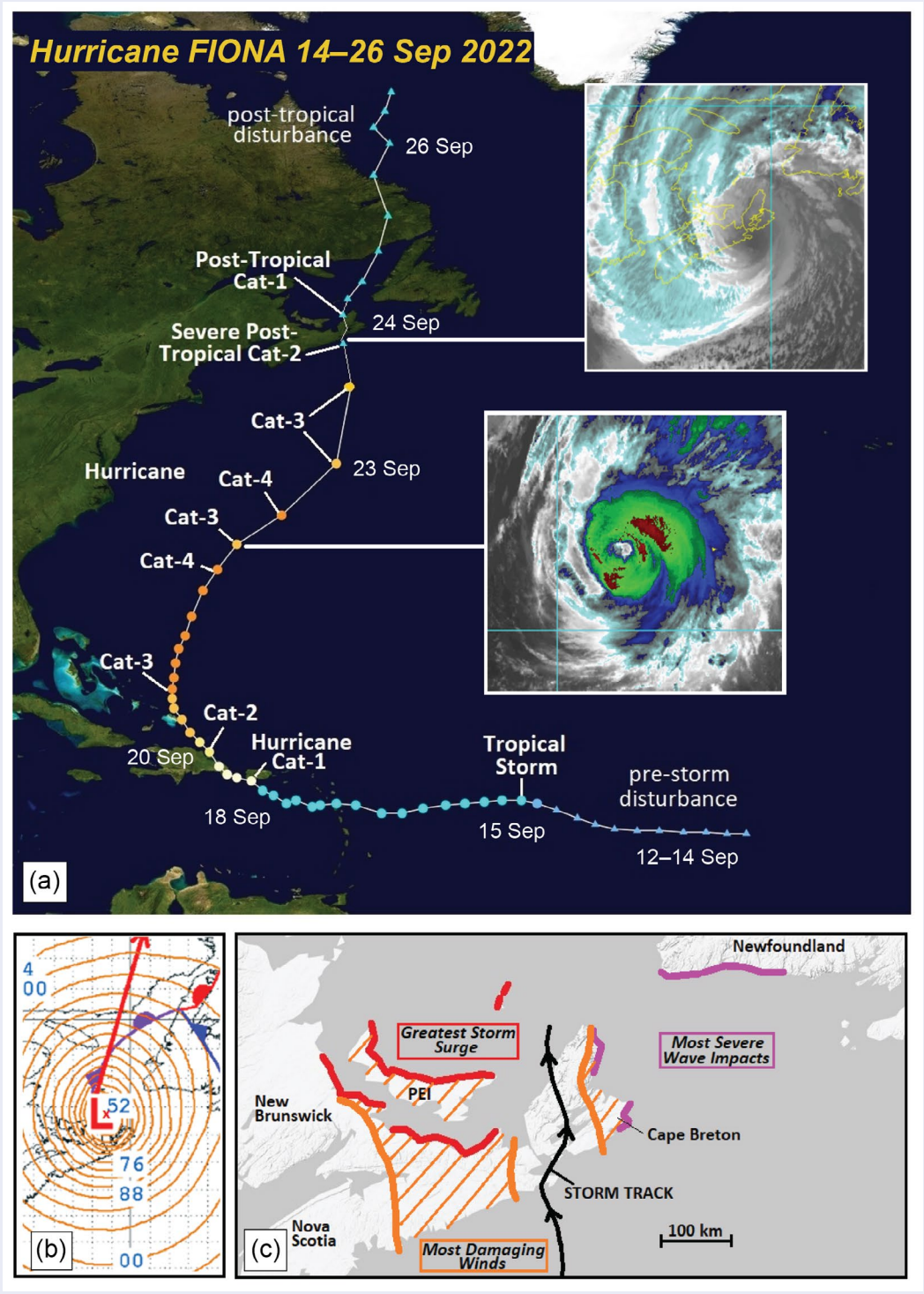

Fig. SB4.1. (a) Track of Hurricane Fiona at 6-hr intervals with select milestones labeled along the track. Triangles denote pre- and post-tropical phases. Two enhanced infrared GOES-16 satellite insets 24 hours apart show the rapid transformation of Fiona from tropical to post-tropical. (b) Sea-level pressure analysis (every 4 hPa, select contour labels marked, e.g., 52 = 952 hPa) from NOAA's Ocean Prediction Center five hours after landfall. Minimum central pressure was ~940 hPa. Direction of travel shown by red arrow. (c) Highlighted regions in Atlantic Canada where the most significant storm impacts were observed.

from Fiona were $800 million (Canadian dollars) as of early 2023, while Hazel's insured losses were estimated to be near $1.4 billion (Canadian dollars, adjusted to 2022).

While Fiona was moving northward towards Nova Scotia early on 23 September, Ian became a tropical depression in the eastern Caribbean Sea and grew to a minimal tropical storm by 0000 UTC on 24 September. Ian moved west-northwestward with little change in strength for the next two days. Upon entering a favorable thermodynamic and outflow environment in the western Caribbean late on 25 August, Ian's maximum sustained winds rapidly intensified from 40 kt (21 m s^{-1}) to 110 kt (57 m s^{-1}) in the ~40 hours prior to initial landfall in western Cuba at 0830 UTC on 27 September. An eyewall replacement cycle occurred during that afternoon and evening as Ian turned north across the southeastern Gulf of Mexico, with a second period of rapid intensification from 105 kt (54 m s^{-1}) to Ian's peak intensity as a Category 5 hurricane with 140 kt (72 m s^{-1}) sustained winds occurring between 0000 and 1200 UTC on the 28th. Maximum winds weakened slightly due to increasing vertical wind shear prior to landfall as a 130 kt (67 m s^{-1}) Category 4 hurricane at 1900 UTC near Cayo Costa in southwest Florida. Ian weakened to a tropical storm over central Florida early on 29 September, then moved offshore and re-strengthened to a Category 1 hurricane later that day as it turned north. The hurricane made a second U.S. landfall near Georgetown, South Carolina, with 75-kt (39-m s^{-1}) sustained winds around 1800 UTC on 30 September. Shortly thereafter, Ian underwent extratropical transition.

Ian stands in the upper echelon of Florida's worst historical hurricanes. Its maximum sustained winds at initial landfall were Florida's fourth strongest on record and equaled those of Hurricane Charley, which struck nearly the same location in 2004. However, Ian exceeded Charley in scope of sensible impacts, as surge, winds, and rain each caused widespread destruction across southwest and central Florida. Peak storm surge of 4 m to 5 m occurred in coastal Lee County (Fig. SB4.2, left panel), leveling portions of Fort Myers Beach and causing significant coastal flooding across parts of Charlotte, Collier, and Monroe Counties. Catastrophic wind gusts exceeding 120 kt (62 m s^{-1}) were observed in Lee and Charlotte Counties as the inner eyewall moved inland, with damaging gusts of 55 kt–70 kt (28 m s^{-1} to 36 m s^{-1}) affecting central Florida and coastal northeast Florida.

Ian's forward speed of 7 kt (4 m s^{-1}) as it crossed the Florida peninsula led to extensive flash and river flooding. As shown in Fig. SB4.2 (right panel), storm-total precipitation along and east of the Interstate 4 corridor totaled 300 mm–500 mm, breaking numerous all-time one- and three-day rainfall records in southwest and central Florida and inundating the low-lying St. Johns and Peace River basins for several months. The severity of coastal and inland flooding resulted in 156 confirmed U.S. fatalities, making Ian Florida's deadliest hurricane since 1935. Total economic losses from Ian are estimated by NOAA's National Centers for Environmental Information to be $114 billion (U.S. dollars), making it the third-costliest Consumer Price Index-adjusted U.S. hurricane on record and the most expensive in Florida's history.

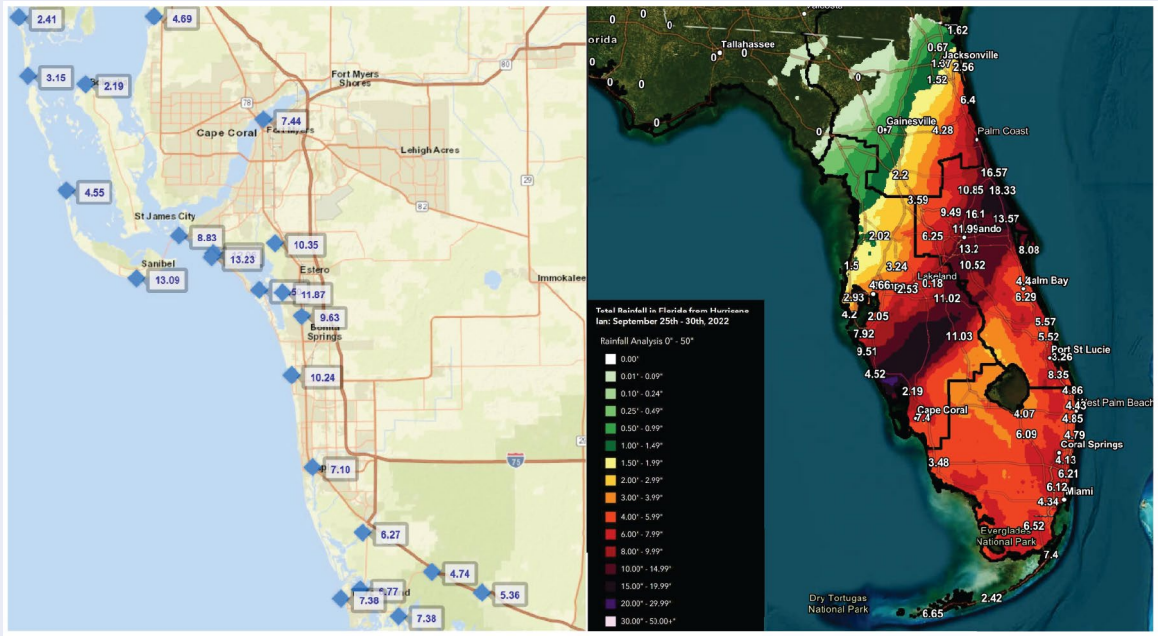

Fig. SB4.2. Hurricane Ian (left) peak inundation levels relative to North American VerticalDatum of 1988 from the United States Geological Survey Flood Event Viewer (Bowyer and MacAfee 2005) for southwest Florida and (right) storm total rainfall estimates (inches). Right panel courtesy of NWS Melbourne, Florida.

Sidebar 4.2: **Tropical cyclone contributions during the 2022 North American monsoon**
—K. M. WOOD

Overall, the 2022 North American monsoon (NAM) season, which is defined as the period 15 June–30 September, produced less rainfall than the near-record setting 2021 season (https://www.weather.gov/psr/2021MonsoonReview). However, many locations received rainfall above the 75th percentile from 1991 to 2020 according to the Parameter-elevation Relationships on Independent Slopes Model (PRISM; Daly et al. 2008) precipitation data. Eastern locations saw rainfall earlier than western locations, and an active period of rain occurred in Arizona during late July into August (Fig. SB4.3b). Tropical cyclone (TC) activity near northern Mexico and the southwestern United States may have influenced some of this rainfall, such as Hurricane Kay which brought rain and wind to California in a rather unusual event for the state (Fig. SB4.3a).

To examine TC activity that may have impacted rainfall during the NAM, we focus on the region north of 20°N and between 120°W and the western North American coastline. Compared with the 1991–2020 average, 2022 had nearly 112% of the typical accumulated cyclone energy (ACE) for this region during 15 June–30 September and about 129% of the typical named storm days in a season that overall produced 88% of the average ACE (see section 4g3). It was the highest ACE for this region since 2016. Of the five TCs that spent at least 24 hours within this region, Kay showed the strongest apparent influence on subsequent rainfall across much of the southwestern United States following a dry period (Fig. SB4.3), corroborated by geostationary satellite imagery (not shown). Though Tropical Storm Madeline remained relatively far south, its passage near the southern end of Baja California was accompanied by a northward surge of moisture that may have supported subsequent rainfall. In summary, the TC season likely had a strong influence on the NAM season.

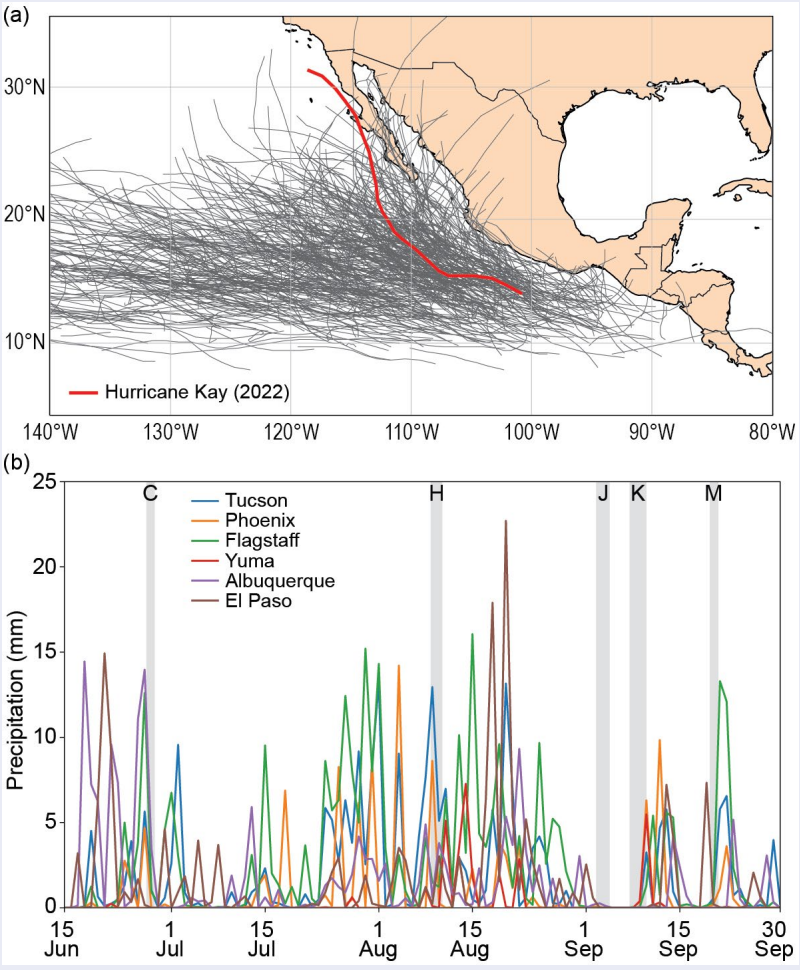

Fig. SB4.3. (a) Track of all eastern North Pacific tropical cyclones from 1991 to 2020 with Hurricane Kay's track highlighted in red. (b) Daily PRISM precipitation averaged within 25 km of Tucson (blue), Phoenix (orange), Flagstaff (green), Yuma (red), Albuquerque (violet), and El Paso (brown). Gray shading indicates times during which a tropical cyclone existed for at least 24 hours within the region north of 20°N and between 120°W and the North American coastline labeled by the first letter of each storm: Celia, Howard, Javier, Kay, and Madeline.

Appendix 1: Chapter 4 – Acronyms

ACE	accumulated cyclone energy
AMO	Atlantic Multi-decadal Oscillation
ASO	August–October
CNP	central North Pacific
CPC	Climate Prediction Center
D26	26°C isotherm
DJF	December–February
ENP	eastern North Pacific
ENSO	El Niño–Southern Oscillation
ERSST	Extended Reconstructed Sea Surface Temperature version 5
ET	extratropical transition
GPI	genesis potential index
HTC	hurricane/typhoon/cyclone
HTHH	Hunga Tonga-Hunga Ha'apai
HURDAT2	Hurricane Database
IBTrACS	International Best Track Archive for Climate Stewardship
IO	Indian Ocean
IOB	Indian Ocean basin
IOD	Indian Ocean dipole
IODE	eastern Indian Ocean dipole
IODW	western Indian Ocean dipole
ITCZ	Intertropical Convergence Zone
JAS	July–September
JASO	July–October
JJA	June–August
JJAS	June–September
JMA	Japan Meteorological Agency
JTWC	Joint Typhoon Warning Center
LMI	lifetime maximum intensity
LMR	land monsoon rainfall
MAM	March–May
MDR	Main Development Region
MJO	Madden-Julian Oscillation
MSLP	mean sea-level pressure
MSWEP	Multi-Source Weighted-Ensemble Precipitation
MTY	major typhoon
NAM	North American monsoon
NH	Northern Hemisphere
NHC	National Hurricane Center
NIO	North Indian Ocean
NOAA GlobalTemp	NOAA Global Surface Temperature Analysis
OISST	Optimum Interpolation Sea Surface Temperature
OLR	outgoing longwave radiation
ONI	Oceanic Niño Index
PAGASA	Philippine Atmospheric, Geophysical and Astronomical Services Administration
PRISM	Parameter-elevation Relationships on Independent Slopes Model
RMM	Real-time Multivariate Madden-Julian Oscillation
RSMC	Regional Specialized Meteorological Center
SAM	Southern Annular Mode

SH	Southern Hemisphere
SIO	South Indian Ocean
SON	September–November
SPCZ	South Pacific Convergence Zone
SPEARrTC	Southwest Pacific Enhanced Archive for Tropical Cyclones
SSHWS	Saffir-Simpson Hurricane Wind Scale
SST	sea-surface temperature
STS	Severe Tropical Storm
TC	tropical cyclone
TCHP	tropical cyclone heat potential
TS	tropical storm
TY	typhoon
WMO	World Meteorological Organization
WNP	western North Pacific

Appendix 2: Chapter 4 – Supplemental Materials

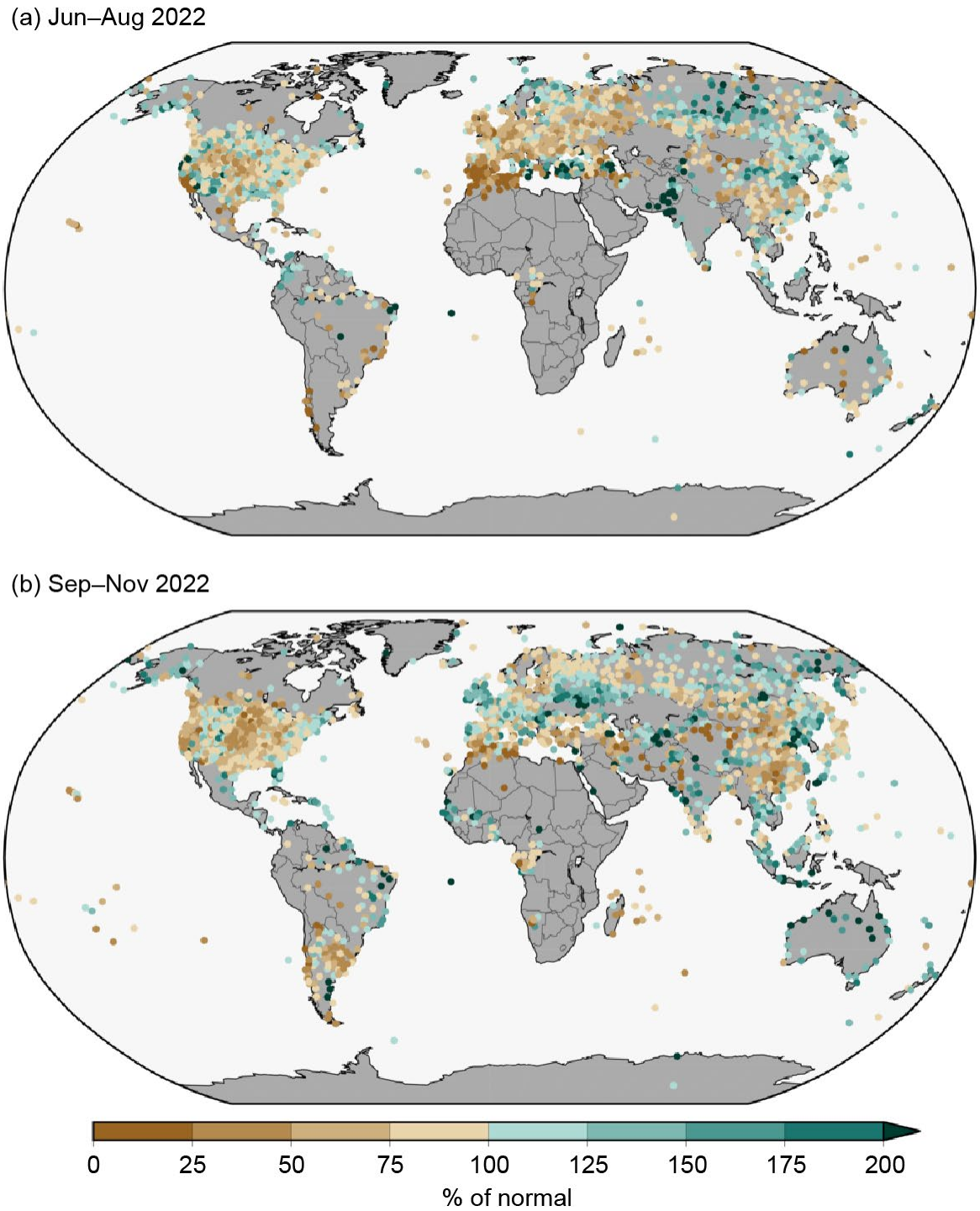

Fig. A4.1. Land-only percent of normal precipitation during (a) JJA 2022 and (b) SON 2022 (relative to a 1961–1990 base period). The figure is provided by NOAA NCEI and the data are from GHCN-M version 4beta (Menne et al. 2018).

References

Aiyyer, A., and J. Molinari, 2008: MJO and tropical cyclogenesis in the Gulf of Mexico and eastern Pacific: Case study and idealized numerical modeling. *J. Atmos. Sci.*, **65**, 2691–2704, https://doi.org/10.1175/2007JAS2348.1.

Aon, 2023: 2023 weather, climate, and catastrophe insight. Accessed 9 March 2023, 115 pp., www.aon.com/getmedia/f34ec133-3175-406c-9e0b-25cea768c5cf/20230125-weather-climate-catastrophe-insight.pdf.

Balaguru, K., P. Chang, R. Saravanan, L. R. Leung, Z. Xu, M. Li, and J. S. Hsieh, 2012: Ocean barrier layers' effect on tropical cyclone intensification. *Proc. Natl. Acad. Sci. USA*, **109**, 14343–14347, https://doi.org/10.1073/pnas.1201364109.

Banzon, V. F., and R. W. Reynolds, 2013: Use of WindSat to extend a microwave-based daily optimum interpolation sea surface temperature time series. *J. Climate*, **26**, 2557–2562, https://doi.org/10.1175/JCLI-D-12-00628.1.

Beck, H. E., E. F. Wood, M. Pan, C. K. Fisher, D. G. Miralles, A. I. J. M. van Dijk, T. R. McVicar, and R. F. Adler, 2019: MSWEP V2 global 3-hourly 0.1° precipitation: Methodology and quantitative assessment. *Bull. Amer. Meteor. Soc.*, **100**, 473–500, https://doi.org/10.1175/BAMS-D-17-0138.1.

Behringer, D. W., M. Ji, and A. Leetmaa, 1998: An improved coupled model for ENSO prediction and implications for ocean initialization. Part I: The ocean data assimilation system. *Mon. Wea. Rev.*, **126**, 1013–1021, https://doi.org/10.1175/1520-0493(1998)1262.0.CO;2.

Bell, G. D., and Coauthors, 2000: The 1999 North Atlantic Hurricane season [in "Climate Assessment for 1999"]. *Bull. Amer. Meteor. Soc.*, **81** (6), S19–S22, https://doi.org/10.1175/1520-0477(2000)81[s1:CAF]2.0.CO;2.

——, ——, ——, S. B. Goldenberg, and R. J. Pasch, 2018: Atlantic basin [in "State of the Climate in 2017"]. *Bull. Amer. Meteor. Soc.*, **99** (8), S114–S118, https://doi.org/10.1175/2018BAMSStateoftheClimate.1.

——, ——, ——, H. Wang, S. B. Goldenberg, and R. J. Pasch, 2019: Atlantic basin [in "State of the Climate in 2018"]. *Bull. Amer. Meteor. Soc.*, **100** (9), S113–S119, https://doi.org/10.1175/2019BAMSStateoftheClimate.1.

——, E. S. Blake, C. W. Landsea, M. Rosencrans, H. Wang, S. B. Goldenberg, and R. J. Pasch, 2020: Atlantic basin [in "State of the Climate in 2019"]. *Bull. Amer. Meteor. Soc.*, **101** (7), S204–S212, https://doi.org/10.1175/BAMS-D-20-0077.1.

Besl, J., 2023: Tonga eruption may temporarily push Earth closer to 1.5°C of warming. *Eos*, **104**, https://doi.org/10.1029/2023EO230104.

Beven, J. L., 2022: National Hurricane Center tropical cyclone report: Hurricane Agatha (EP012022), 28–31 May 2022. NHC Tech. Rep., 22 pp., https://www.nhc.noaa.gov/data/tcr/EP012022_Agatha.pdf.

Bjerknes, J., 1969: Atmospheric teleconnections from the equatorial Pacific. *Mon. Wea. Rev.*, **97**, 163–172, https://doi.org/10.1175/1520-0493(1969)0972.3.CO;2.

Bowyer, P. J., and A. W. MacAfee, 2005: The theory of trapped-fetch waves within tropical cyclones—An operational perspective. *Wea. Forecasting*, **20**, 229–244, https://doi.org/10.1175/WAF849.1.

Bucci, L., L. Alaka, A. Hagen, S. Delgado, and J. Beven, 2023: National Hurricane Center tropical cyclone report: Hurricane Ian (AL092022), 23–30 September 2022. NHC Tech. Rep., 72 pp., https://www.nhc.noaa.gov/data/tcr/AL092022_Ian.pdf.

Camargo, S. J., and A. H. Sobel, 2005: Western North Pacific tropical cyclone intensity and ENSO. *J. Climate*, **18**, 2996–3006, https://doi.org/10.1175/JCLI3457.1.

——, A. W. Robertson, S. J. Gaffney, P. Smyth, and M. Ghil, 2007a: Cluster analysis of typhoon tracks: Part II: Large-scale circulation and ENSO. *J. Climate*, **20**, 3654–3676, https://doi.org/10.1175/JCLI4203.1.

——, K. A. Emanuel, and A. H. Sobel, 2007b: Use of a genesis potential index to diagnose ENSO effects on tropical cyclone genesis. *J. Climate*, **20**, 4819–4834, https://doi.org/10.1175/JCLI4282.1.

——, M. C. Wheeler, and A. H. Sobel, 2009: Diagnosis of the MJO modulation of tropical cyclogenesis using an empirical index. *J. Atmos. Sci.*, **66**, 3061–3074, https://doi.org/10.1175/2009JAS3101.1.

Cangialosi, J. P., 2023: National Hurricane Center tropical cyclone report: Hurricane Julia (AL132022, EP182022), 7–10 October 2022. NHC Tech. Rep., 23 pp., https://www.nhc.noaa.gov/data/tcr/AL132022_EP182022_Julia.pdf.

Chen, L., and J.-J. Luo, 2021: Indian Ocean dipole and unique Indian Ocean basin warming in 2020 [in "State of the climate in 2020"]. *Bull. Amer. Meteor. Soc.*, **102** (8), S220–S222, https://doi.org/10.1175/BAMS-D-21-0080.1.

——, and ——, 2022: Indian Ocean dipole [in "State of the Climate in 2021"]. *Bull. Amer. Meteor. Soc.*, **103** (8), S213–S217, https://doi.org/10.1175/BAMS-D-22-0069.1.

Chia, H. H., and C. F. Ropelewski, 2002: The interannual variability in the genesis location of tropical cyclones in the northwest Pacific. *J. Climate*, **15**, 2934–2944, https://doi.org/10.1175/1520-0442(2002)0152.0.CO;2.

Daly, C., M. Halbleib, J. I. Smith, W. P. Gibson, M. K. Doggett, G. H. Taylor, J. Curtis, and P. A. Pasteris, 2008: Physiographically-sensitive mapping of temperature and precipitation across the conterminous United States. *Int. J. Climatol.*, **28**, 2031–2064, https://doi.org/10.1002/joc.1688.

Dare, R. A., and J. L. McBride, 2011: Sea surface temperature response to tropical cyclones. *Mon. Wea. Rev.*, **139**, 3798–3808, https://doi.org/10.1175/MWR-D-10-05019.1.

DeMaria, M., M. Mainelli, L. K. Shay, J. A. Knaff, and J. Kaplan, 2005: Further improvements to the Statistical Hurricane Intensity Prediction Scheme (SHIPS). *Wea. Forecasting*, **20**, 531–543, https://doi.org/10.1175/WAF862.1.

Diamond, H. J., and J. A. Renwick, 2015: The climatological relationship between tropical cyclones in the southwest Pacific and the Madden–Julian Oscillation. *Int. J. Climatol.*, **35**, 676–686, https://doi.org/10.1002/joc.4012.

——, and C. J. Schreck, 2022: The tropics [in "State of the Climate in 2021"]. *Bull. Amer. Meteor. Soc.*, **103** (8), S1–S59, https://doi.org/10.1175/BAMS-D-22-0069.1.

——, A. M. Lorrey, K. R. Knapp, and D. H. Levinson, 2012: Development of an enhanced tropical cyclone tracks database for the southwest Pacific from 1840 to 2011. *Int. J. Climatol.*, **32**, 2240–2250, https://doi.org/10.1002/joc.2412.

Ding, Q., E. J. Steig, D. S. Battisti, and J. M. Wallace, 2012: Influence of the tropics on the Southern Annular Mode. *J. Climate*, **25**, 6330–6348, https://doi.org/10.1175/JCLI-D-11-00523.1.

Domingues, R., and Coauthors, 2015: Upper ocean response to Hurricane Gonzalo (2014): Salinity effects revealed by targeted and sustained underwater glider observations. *Geophys. Res. Lett.*, **42**, 7131–7138, https://doi.org/10.1002/2015GL065378.

Dube, S. K., D. Rao, P. C. Sinha, T. S. Murty, and N. Bahuluyan, 1997: Storm surge in the Bay of Bengal and Arabian Sea: The problem and its prediction. *Mausam*, **48**, 288–304, https://doi.org/10.54302/mausam.v48i2.4012.

Ebita, A., and Coauthors, 2011: The Japanese 55-year Reanalysis "JRA-55": An interim report. *SOLA*, **7**, 149–152, https://doi.org/10.2151/sola.2011-038.

Emanuel, K. A., 1988: The maximum intensity of hurricanes. *J. Atmos. Sci.*, **45**, 1143–1155, https://doi.org/10.1175/1520-0469(1988)0452.0.CO;2.

—— , and D. S. Nolan, 2004: Tropical cyclone activity and the global climate system. *26th Conf. on Hurricanes and Tropical Meteorology*, Miami, FL, Amer. Meteor. Soc., 10A.2, https://ams.confex.com/ams/26HURR/techprogram/paper_75463.htm.

Enfield, D. B., and A. M. Mestas-Nuñez, 1999: Multiscale variabilities in global sea surface temperatures and their relationships with tropospheric climate patterns. *J. Climate*, **12**, 2719–2733, https://doi.org/10.1175/1520-0442(1999)0122.0.CO;2.

Fang, X., and Coauthors, 2023: Will the history-record southeasterly wind in March 2022 trigger a third-year La Niña event? *Adv. Atmos. Sci.*, **40**, 6–13, https://doi.org/10.1007/s00376-022-2147-6.

Frank, W. M., and P. E. Roundy, 2006: The role of tropical waves in tropical cyclogenesis. *Mon. Wea. Rev.*, **134**, 2397–2417, https://doi.org/10.1175/MWR3204.1.

Gallagher Re, 2023: Gallagher Re natural catastrophe report: 2022, 60 pp., https://www.ajg.com/gallagherre/news-and-insights/2023/january/nat-cat-report-2022/.

Goldenberg, S. B., and L. J. Shapiro, 1996: Physical mechanisms for the association of El Niño and West African rainfall with Atlantic major hurricane activity. *J. Climate*, **9**, 1169–1187, https://doi.org/10.1175/1520-0442(1996)0092.0.CO;2.

—— , C. W. Landsea, A. M. Mestas-Nuñez, and W. M. Gray, 2001: The recent increase in Atlantic hurricane activity: Causes and implications. *Science*, **293**, 474–479, https://doi.org/10.1126/science.1060040.

Goni, G. J., and Coauthors, 2009: Applications of satellite-derived ocean measurements to tropical cyclone intensity forecasting. *Oceanography*, **22**, 176–183, https://doi.org/10.5670/oceanog.2009.78.

—— , and Coauthors, 2017: Autonomous and Lagrangian ocean observations for Atlantic tropical cyclone studies and forecasts. *Oceanography*, **30**, 92–103, https://doi.org/10.5670/oceanog.2017.227.

Gray, W. M., 1968: Global view of the origin of tropical disturbances and storms. *Mon. Wea. Rev.*, **96**, 669–700, https://doi.org/10.1175/1520-0493(1968)0962.0.CO;2.

—— , 1990: Strong association between West African rainfall and U.S. landfall of intense hurricanes. *Science*, **249**, 1251–1256, https://doi.org/10.1126/science.249.4974.1251.

Guo, Y., X. Jiang, and D. E. Waliser, 2014: Modulation of the convectively coupled Kelvin waves over South America and the tropical Atlantic Ocean in association with the Madden–Julian oscillation. *J. Atmos. Sci.*, **71**, 1371–1388, https://doi.org/10.1175/JAS-D-13-0215.1.

Hastenrath, S., 1990: Decadal-scale changes of the circulation in the tropical Atlantic sector associated with Sahel drought. *Int. J. Climatol.*, **10**, 459–472, https://doi.org/10.1002/joc.3370100504.

Hendon, H., C. Zhang, and J. Glick, 1999: Interannual variation of the Madden–Julian oscillation during austral summer. *J. Climate*, **12**, 2538–2550, https://doi.org/10.1175/1520-0442(1999)0122.0.CO;2.

Hersbach, H., and Coauthors, 2020: The ERA5 global reanalysis. *Quart. J. Roy. Meteor. Soc.*, **146**, 1999–2049, https://doi.org/10.1002/qj.3803.

Hong, C.-C., T. Li, and J.-J. Luo, 2008: Asymmetry of the Indian Ocean dipole. Part II: Model diagnosis. *J. Climate*, **21**, 4849–4858, https://doi.org/10.1175/2008JCLI2223.1.

Huang, B., and Coauthors, 2017: Extended Reconstructed Sea Surface Temperature, version 5 (ERSSTv5): Upgrades, validations, and intercomparisons. *J. Climate*, **30**, 8179–8205, https://doi.org/10.1175/JCLI-D-16-0836.1.

—— , C. Liu, V. Banzon, E. Freeman, G. Graham, B. Hankins, T. Smith, and H.-M. Zhang, 2020: Improvements of the Daily Optimum Interpolation Sea Surface Temperature (DOISST) version 2.1. *J. Climate*, **34**, 2923–2939, https://doi.org/10.1175/JCLI-D-20-0166.1.

Huffman, G. J., R. F. Adler, D. T. Bolvin, and G. Gu, 2009: Improving the global precipitation record: GPCP version 2.1. *Geophys. Res. Lett.*, **36**, L17808, https://doi.org/10.1029/2009GL040000.

—— , D. T. Bolvin, D. Braithwaite, K. Hsu, R. Joyce, and P. Xie, 2014: NASA Global Precipitation Measurement Integrated Multi-satellitE Retrievals for GPM (IMERG). Algorithm Theoretical Basis Doc., version 4.4, 26 pp., https://pps.gsfc.nasa.gov/Documents/IMERG_ATBD_V4.pdf.

Izumo, T., and Coauthors, 2010: Influence of the state of the Indian Ocean dipole on the following year's El Niño. *Nat. Geosci.*, **3**, 168–172, https://doi.org/10.1038/ngeo760.

Kalnay, E., and Coauthors, 1996: The NCEP/NCAR 40-Year Reanalysis Project. *Bull. Amer. Meteor. Soc.*, **77**, 437–471, https://doi.org/10.1175/1520-0477(1996)0772.0.CO;2.

Kiladis, G. N., and K. M. Weickmann, 1992: Circulation anomalies associated with tropical convection during northern winter. *Mon. Wea. Rev.*, **120**, 1900–1923, https://doi.org/10.1175/1520-0493(1992)1202.0.CO;2.

—— , M. C. Wheeler, P. T. Haertel, K. H. Straub, and P. E. Roundy, 2009: Convectively coupled equatorial waves. *Rev. Geophys.*, **47**, RG2003, https://doi.org/10.1029/2008RG000266.

Klotzbach, P. J., K. M. Wood, C. J. Schreck III, S. G. Bowen, C. M. Patricola, and M. M. Bell, 2022: Trends in Global Tropical Cyclone Activity: 1990–2021. *Geophys. Res. Lett.*, **49**, e2021GL095774.

Knaff, J. A., C. R. Sampson, and K. D. Musgrave, 2018: An operational rapid intensification prediction aid for the western North Pacific. *Wea. Forecasting*, **33**, 799–811, https://doi.org/10.1175/WAF-D-18-0012.1.

—— , —— , and B. R. Strahl, 2020: A tropical cyclone rapid intensification prediction aid for the Joint Typhoon Warning Center's areas of responsibility. *Wea. Forecasting*, **35**, 1173–1185, https://doi.org/10.1175/WAF-D-19-0228.1.

Knapp, K. R., M. C. Kruk, D. H. Levinson, H. J. Diamond, and C. J. Neumann, 2010: The International Best Track Archive for Climate Stewardship (IBTrACS): Unifying tropical cyclone data. *Bull. Amer. Meteor. Soc.*, **91**, 363–376, https://doi.org/10.1175/2009BAMS2755.1.

—— , J. A. Knaff, C. R. Sampson, G. M. Riggio, and A. D. Schnapp, 2013: A pressure-based analysis of the historical western North Pacific tropical cyclone intensity record. *Mon. Wea. Rev.*, **141**, 2611–2631, https://doi.org/10.1175/MWR-D-12-00323.1.

Krishnamurti, T. N., and D. Subrahmanyam, 1982: The 30–50 day mode at 850 mb during MONEX. *J. Atmos. Sci.*, **39**, 2088–2095, https://doi.org/10.1175/1520-0469(1982)0392.0.CO;2.

Kumar, A., and Z.-Z. Hu, 2014: Interannual and interdecadal variability of ocean temperature along the equatorial Pacific in conjunction with ENSO. *Climate Dyn.*, **42**, 1243–1258, https://doi.org/10.1007/s00382-013-1721-0.

Landsea, C. W., and J. L. Franklin, 2013: Atlantic Hurricane database uncertainty and presentation of a new database format. *Mon. Wea. Rev.*, **141**, 3576–3592, https://doi.org/10.1175/MWR-D-12-00254.1.

——, W. M. Gray, P. W. Mielke, and K. J. Berry, 1992: Long-term variations of western Sahelian monsoon rainfall and intense U.S. landfalling hurricanes. *J. Climate*, **5**, 1528–1534, https://doi.org/10.1175/1520-0442(1992)0052.0.CO;2.

——, G. A. Vecchi, L. Bengtsson, and T. R. Knutson, 2010: Impact of duration thresholds on Atlantic tropical cyclone counts. *J. Climate*, **23**, 2508–2519, https://doi.org/10.1175/2009JCLI3034.1.

Lau, W. K.-M., and D. E. Waliser, 2012: *Intraseasonal Variability in the Atmosphere-Ocean Climate System*. Springer, 642 pp.

Leipper, D. F., and D. Volgenau, 1972: Hurricane heat potential of the Gulf of Mexico. *J. Phys. Oceanogr.*, **2**, 218–224, https://doi.org/10.1175/1520-0485(1972)0022.0.CO;2.

Liebmann, B., and C. A. Smith, 1996: Description of a complete (interpolated) outgoing longwave radiation dataset. *Bull. Amer. Meteor. Soc.*, **77**, 1275–1277, https://doi.org/10.1175/1520-0477-77.6.1274.

Lin, I. I., and Coauthors, 2013: An ocean coupling potential intensity index for tropical cyclones. *Geophys. Res. Lett.*, **40**, 1878–1882, https://doi.org/10.1002/grl.50091.

——, I.-F. Pun, and C.-C. Lien, 2014: 'Category-6' Supertyphoon Haiyan in global warming hiatus: Contribution from subsurface ocean warming. *Geophys. Res. Lett.*, **41**, 8547–8553, https://doi.org/10.1002/2014GL061281.

——, and Coauthors, 2020: ENSO and tropical cyclones. *El Niño Southern Oscillation in a Changing Climate*, *Geophys. Monogr.*, Vol. 253, Amer. Geophys. Union, 377–408, https://doi.org/10.1002/9781119548164.ch17.

Liu, T., J. Li, C. Sun, T. Lian, and Y. Zhang, 2021: Impact of the April–May SAM on central Pacific Ocean sea temperature over the following three seasons. *Climate Dyn.*, **57**, 775–786, https://doi.org/10.1007/s00382-021-05738-4.

Luo, J.-J., S. Masson, S. Behera, and T. Yamagata, 2007: Experimental forecasts of the Indian Ocean dipole using a coupled OAGCM. *J. Climate*, **20**, 2178–2190, https://doi.org/10.1175/JCLI4132.1.

——, R. Zhang, S. K. Behera, Y. Masumoto, F.-F. Jin, R. Lukas, and T. Yamagata, 2010: Interaction between El Niño and extreme Indian Ocean dipole. *J. Climate*, **23**, 726–742, https://doi.org/10.1175/2009JCLI3104.1.

——, W. Sasaki, and Y. Masumoto, 2012: Indian Ocean warming modulates Pacific climate change. *Proc. Natl. Acad. Sci. USA*, **109**, 18701–18706, https://doi.org/10.1073/pnas.1210239109.

Madden, R., and P. Julian, 1971: Detection of a 40–50 day oscillation in the zonal wind in the tropical Pacific. *J. Atmos. Sci.*, **28**, 702–708, https://doi.org/10.1175/1520-0469(1971)0282.0.CO;2.

——, and ——, 1972: Description of global-scale circulation cells in the tropics with a 40–50 day period. *J. Atmos. Sci.*, **29**, 1109–1123, https://doi.org/10.1175/1520-0469(1972)0292.0.CO;2.

——, and ——, 1994: Observations of the 40–50-day tropical oscillation: A review. *Mon. Wea. Rev.*, **122**, 814–837, https://doi.org/10.1175/1520-0493(1994)1222.0.CO;2.

Mainelli, M., M. DeMaria, L. Shay, and G. Goni, 2008: Application of oceanic heat content estimation to operational forecasting of recent Atlantic category 5 hurricanes. *Wea. Forecasting*, **23**, 3–16, https://doi.org/10.1175/2007WAF2006111.1.

Maloney, E. D., and D. L. Hartmann, 2001: The Madden–Julian oscillation, barotropic dynamics, and North Pacific tropical cyclone formation. Part I: Observations. *J. Atmos. Sci.*, **58**, 2545–2558, https://doi.org/10.1175/1520-0469(2001)0582.0.CO;2.

Matthews, A. J., 2008: Primary and successive events in the Madden–Julian Oscillation. *Quart. J. Roy. Meteor. Soc.*, **134**, 439–453, https://doi.org/10.1002/qj.224.

Menne, M. J., B. E. Gleason, J. Lawrimore, J. Rennie, and C. N. Williams, 2018: Global Historical Climatology Network – Monthly temperature, version 4 (BETA). NOAA National Centers for Environmental Information, https://doi.org/10.7289/V5XW4GTH.

Millán, L., and Coauthors, 2022: The Hunga Tonga-Hunga Ha'apai Hydration of the stratosphere. *Geophys. Res. Lett.*, **49**, e2022GL099381, https://doi.org/10.1029/2022GL099381.

Mo, K. C., 2000: The association between intraseasonal oscillations and tropical storms in the Atlantic Basin. *Mon. Wea. Rev.*, **128**, 4097–4107, https://doi.org/10.1175/1520-0493(2000)1292.0.CO;2.

Moreno, P. I., and Coauthors, 2018: Onset and evolution of Southern Annular Mode-like changes at centennial timescale. *Sci. Rep.*, **8**, 3458, https://doi.org/10.1038/s41598-018-21836-6.

Münnich, M., and J. D. Neelin, 2005: Seasonal influence of ENSO on the Atlantic ITCZ and equatorial South America. *Geophys. Res. Lett.*, **32**, L21709, https://doi.org/10.1029/2005GL023900.

Nicholls, N., 1979: A possible method for predicting seasonal tropical cyclone activity in the Australian region. *Mon. Wea. Rev.*, **107**, 1221–1224, https://doi.org/10.1175/1520-0493(1979)1072.0.CO;2.

Nobre, P., and J. Shukla, 1996: Variations of sea surface temperature, wind stress and rainfall over the tropical Atlantic and South America. *J. Climate*, **9**, 2464–2479, https://doi.org/10.1175/1520-0442(1996)0092.0.CO;2.

Pasch, R. J., B. J. Reinhart, and L. Alaka, 2023: National Hurricane Center tropical cyclone report: Hurricane Ian (AL072022), 14–23 September 2022. NHC Tech. Rep., 60 pp., www.nhc.noaa.gov/data/tcr/AL072022_Fiona.pdf.

Raga, G. B., B. Bracamontes-Ceballos, L. Farfán, and R. Romero-Centeno, 2013: Landfalling tropical cyclones on the Pacific coast of Mexico: 1850–2010. *Atmósfera*, **26**, 209–220, https://doi.org/10.1016/S0187-6236(13)71072-5.

Ramage, C. S., 1971: *Monsoon Meteorology*. Academic Press, 296 pp.

Reinhart, B. J., 2022: Tropical Storm Lester. National Hurricane Center tropical cyclone report (EP132022), 15–17 September 2022. NHC Tech. Rep., 14 pp., www.nhc.noaa.gov/data/tcr/EP132022_Lester.pdf.

Reynolds, R. W., N. A. Rayner, T. M. Smith, D. C. Stokes, and W. Wang, 2002: An improved in situ and satellite SST analysis for climate. *J. Climate*, **15**, 1609–1625, https://doi.org/10.1175/1520-0442(2002)0152.0.CO;2.

Riddle, E., M. Stoner, N. Johnson, M. L'Heureux, D. Collins, and S. Feldstein, 2012: The impact of the MJO on clusters of wintertime circulation anomalies over the North American region. *Climate Dyn.*, **40**, 1749–1766, https://doi.org/10.1007/s00382-012-1493-y.

Ropelewski, C. F., and M. S. Halpert, 1989: Precipitation patterns associated with the high index phase of the Southern Oscillation. *J. Climate*, **2**, 268–284, https://doi.org/10.1175/1520-0442(1989)0022.0.CO;2.

Saha, S., and Coauthors, 2014: The NCEP Climate Forecast System version 2. *J. Climate*, **27**, 2185–2208, https://doi.org/10.1175/JCLI-D-12-00823.1.

Saji, N. H., B. N. Goswami, P. N. Vinayachandran, and T. Yamagata, 1999: A dipole mode in the tropical Indian Ocean. *Nature*, **401**, 360–363, https://doi.org/10.1038/43854.

Schneider, T., T. Bischoff, and G. H. Haug, 2014: Migrations and dynamics of the intertropical convergence zone. *Nature*, **513**, 45–53, https://doi.org/10.1038/nature13636.

Schreck, C. J., 2015: Kelvin waves and tropical cyclogenesis: A global survey. *Mon. Wea. Rev.*, **143**, 3996–4011, https://doi.org/10.1175/MWR-D-15-0111.1.

——, 2016: Convectively coupled Kelvin waves and tropical cyclogenesis in a semi-Lagrangian framework. *Mon. Wea. Rev.*, **144**, 4131–4139, https://doi.org/10.1175/MWR-D-16-0237.1.

——, and J. Molinari, 2011: Tropical cyclogenesis associated with Kelvin waves and the Madden–Julian oscillation. *Mon. Wea. Rev.*, **139**, 2723–2734, https://doi.org/10.1175/MWR-D-10-05060.1.

——, J. Molinari, and A. Aiyyer, 2012: A global view of equatorial waves and tropical cyclogenesis. *Mon. Wea. Rev.*, **140**, 774–788, https://doi.org/10.1175/MWR-D-11-00110.1.

——, K. R. Knapp, and J. P. Kossin, 2014: The impact of best track discrepancies on global tropical cyclone climatologies using IBTrACS. *Mon. Wea. Rev.*, **142**, 3881–3899, https://doi.org/10.1175/MWR-D-14-00021.1.

——, H.-T. Lee, and K. R. Knapp, 2018: HIRS outgoing longwave radiation—Daily climate data record: Application toward identifying tropical subseasonal variability. *Remote Sens.*, **10**, 1325, https://doi.org/10.3390/rs10091325.

Shay, L. K., G. J. Goni, and P. G. Black, 2000: Effects of a warm oceanic feature on Hurricane Opal. *Mon. Wea. Rev.*, **128**, 1366–1383, https://doi.org/10.1175/1520-0493(2000)1282.0.CO;2.

Tippett, M. K., S. J. Camargo, and A. H. Sobel, 2011: A Poisson regression index for tropical cyclone genesis and the role of large-scale vorticity in genesis. *J. Climate*, **24**, 2335–2357, https://doi.org/10.1175/2010JCLI3811.1.

Trenberth, K. E., 1984: Signal versus noise in the Southern Oscillation. *Mon. Wea. Rev.*, **112**, 326–332, https://doi.org/10.1175/1520-0493(1984)1122.0.CO;2

Vecchi, G. A., and B. J. Soden, 2007: Effect of remote sea surface temperature change on tropical cyclone potential intensity. *Science*, **450**, 1066–1071, https://doi.org/10.1038/nature06423.

Ventrice, M. J., C. D. Thorncroft, and M. A. Janiga, 2012a: Atlantic tropical cyclogenesis: A three-way interaction between an African easterly wave, diurnally varying convection, and a convectively coupled atmospheric Kelvin wave. *Mon. Wea. Rev.*, **140**, 1108–1124, https://doi.org/10.1175/MWR-D-11-00122.1.

——, ——, and C. J. Schreck, 2012b: Impacts of convectively coupled Kelvin waves on environmental conditions for Atlantic tropical cyclogenesis. *Mon. Wea. Rev.*, **140**, 2198–2214, https://doi.org/10.1175/MWR-D-11-00305.1.

Villarini, G., G. A. Vecchi, T. R. Knutson, and J. A. Smith, 2011: Is the recorded increase in short duration North Atlantic tropical storms spurious? *J. Geophys. Res.*, **116**, D10114, https://doi.org/10.1029/2010JD015493.

Vincent, D. G., 1994: The South Pacific Convergence Zone (SPCZ): A review. *Mon. Wea. Rev.*, **122**, 1949–1970, https://doi.org/10.1175/1520-0493(1994)1222.0.CO;2.

Vose, R. S., and Coauthors, 2021: Implementing full spatial coverage in NOAA's Global Temperature Analysis. *Geophys. Res. Lett.*, **48**, e2020GL090873, https://doi.org/10.1029/2020GL090873.

Waliser, D. E., and C. Gautier, 1993: A satellite-derived climatology of the ITCZ. *J. Climate*, **6**, 2162–2174, https://doi.org/10.1175/1520-0442(1993)0062.0.CO;2.

Wang, B., 1994: Climatic regimes of tropical convection and rainfall. *J. Climate*, **7**, 1109–1118, https://doi.org/10.1175/1520-0442(1994)0072.0.CO;2.

——, and Q. Ding, 2008: Global monsoon: Dominant mode of annual variation in the tropics. *Dyn. Atmos. Ocean*, **44**, 165–183, https://doi.org/10.1016/j.dynatmoce.2007.05.002.

——, J. Liu, H. J. Kim, P. J. Webster, and S. Y. Yim, 2012: Recent change of the global monsoon precipitation (1979–2008). *Climate Dyn.*, **39**, 1123–1135, https://doi.org/10.1007/s00382-011-1266-z.

Wheeler, M., and G. N. Kiladis, 1999: Convectively coupled equatorial waves: Analysis of clouds and temperature in the wavenumber–frequency domain. *J. Atmos. Sci.*, **56**, 374–399, https://doi.org/10.1175/1520-0469(1999)0562.0.CO;2.

——, and H. H. Hendon, 2004: An all-season real-time multivariate MJO index: Development of an index for monitoring and prediction. *Mon. Wea. Rev.*, **132**, 1917–1932, https://doi.org/10.1175/1520-0493(2004)1322.0.CO;2.

Wood, K. M., and E. A. Ritchie, 2015: A definition for rapid weakening in the North Atlantic and eastern North Pacific. *Geophys. Res. Lett.*, **42**, 10091–10097, https://doi.org/10.1002/2015GL066697.

——, and C. J. Schreck, 2020: Eastern North Pacific and central North Pacific basins [in "State of the Climate in 2019"]. *Bull. Amer. Meteor. Soc.*, **101** (8), S212–S214, https://doi.org/10.1175/BAMS-D-20-0077.1.

——, and ——, 2021: Eastern North Pacific and central North Pacific basins [in "State of the Climate in 2020"]. *Bull. Amer. Meteor. Soc.*, **102** (8), S233–S235, https://doi.org/10.1175/BAMS-D-21-0080.1.

——, and ——, 2022: Eastern North Pacific and central North Pacific basins [in "State of the Climate in 2021"]. *Bull. Amer. Meteor. Soc.*, **103** (8), S229–S231, https://doi.org/10.1175/BAMS-D-22-0069.1.

Yim, S. Y., B. Wang, J. Liu, and Z. W. Wu, 2014: A comparison of regional monsoon variability using monsoon indices. *Climate Dyn.*, **43**, 1423–1437, https://doi.org/10.1007/s00382-013-1956-9.

Yin, J. F., H. Gu, X. Liang, M. Yu, J. Sun, Y. Xie, F. Li, and C. Wu, 2022: A possible dynamic mechanism for rapid production of the extreme hourly rainfall in Zhengzhou City on 20 July 2021. *J. Meteor. Res.*, **36**, 6–25, https://doi.org/10.1007/s13351-022-1166-7.

Zhang, C., 2005: Madden–Julian oscillation. *Rev. Geophys.*, **43**, RG2003, https://doi.org/10.1029/2004RG000158.

——, and J. Gottschalck, 2002: SST anomalies of ENSO and the Madden–Julian oscillation in the equatorial Pacific. *J. Climate*, **15**, 2429–2445, https://doi.org/10.1175/1520-0442(2002)0152.0.CO;2.

Zheng, Z.-W., I.-I. Lin, B. Wang, H.-C. Huang, and C.-H. Chen, 2015: A long neglected damper in the El Nino–typhoon relationship: A 'Gaia-like' process. *Sci. Rep.*, **5**, 11103, https://doi.org/10.1038/srep11103.

Zuo, M., T. Zhou, W. Man, X. Chen, J. Liu, F. Liu, and C. Gao, 2022: Volcanoes and climate: Sizing up the impact of the recent Hunga Tonga-Hunga Ha'apai volcanic eruption from a historical perspective. *Adv. Atmos. Sci.*, **39**, 1986–1993, https://doi.org/10.1007/s00376-022-2034-1.